Mathematical Framework and Numerical Methods for the Modeling of Mechanochemistry in Multi-phase Materials

by

Gregory H. Teichert

A dissertation submitted in partial fulfillment
of the requirements for the degree of
Doctor of Philosophy
(Mechanical Engineering)
in The University of Michigan
2017

Doctoral Committee:

Professor Krishnakumar R. Garikipati, Chair
Associate Professor Vikram Gavini
Associate Professor Emmanuelle Marquis
Professor Anton Van der Ven

Gregory H. Teichert

greght@umich.edu

ORCID iD: 0000-0003-2387-4942

ACKNOWLEDGEMENTS

I would like to thank my advisor, Professor Krishna Garikipati, for his continued guidance and support throughout my graduate education. I also gratefully acknowledge the help and insight from Professors Vikram Gavini, Emmanuelle Marquis, and Anton Van der Ven.

Thanks also to my lab fellows: Shiva Rudraraju, Koki Sagiyama, Sarah Verner, and Zhenlin Wang, as well as Anirudh Natarajan, Hasrsha Gunda, and Ellen Solomon for their help and encouragement.

I particularly want to thank my family for their love, support, and encouragement: my parents and siblings; my sons, Hyrum and Soren; and especially my wife, Michelle.

TABLE OF CONTENTS

LIST OF FIGURES

FIGURE

LIST OF TABLES

TABLE

LIST OF APPENDICES

APPENDIX

ABSTRACT

This dissertation presents a suite of mathematical formulations and numerical methods for modeling the interactions between solid mechanics and chemistry in multi-phase materials. In all cases, the treatments rely on the free energy of the system, which potentially includes the strain energy, the chemical free energy, and the interfacial energy. Variational methods are applied to the free energy functionals to derive equilibrium conditions for mechanics and to identify constraints on kinetic laws for chemistry. The applications of this class of variational methods include evolving material configurations associated with phase changes, both diffusive (e.g. oxidation) and non-diffusive (e.g. martensitic transformations). Motivated by the need to represent multi-well, oscillatory, free energy densities, a study is presented comparing spline and polynomial forms for these functions. An alternative approach to phase-field dynamics for finding a minimum energy state is demonstrated, with Mg alloy precipitates as an example. It involves learning the free energy surface as a function of key geometric features with machine learning techniques, which are then used to predict a minimum energy state. This collection of mathematical formulations and numerical methods is aimed at explorations of the physics underlying observed phenomena in multi-phase materials, with potential use in materials' design.

CHAPTER I

Introduction

The modeling of materials physics plays a key role, together with physical experimentation and observation, in understanding the driving mechanisms behind material phenomena. As these driving forces are more clearly understood, mathematical and numerical models can turn from replicating what is currently seen to predicting what might be possible given an alternative set of inputs. The construction of these models generally depends on the nature of the underlying mechanisms and the scales on which they occur. This dissertation considers the interplay between the solid mechanics and chemical composition of materials on the continuum scale. While the formulations and methods are applicable to a wide range of materials, to fix ideas they are in most cases presented in the context of a specific material or material phenomena.

1.1 Material phenomena

Three types of material phenomena are considered in the dissertation: martensitic transformations, titanium oxidation, and formation of precipitates in Mg-Rare Earth alloys.

Martensitic transformations are diffusionless, lattice-distorting phase transitions [7, 8, 9, 10, 11, 12]. The transformation from austenite to martensite in steel is, perhaps, the most well-known example and has been utilized for millenia [7]. In the

comparatively recent past, reversible martensitic transformations have been found to be responsible for the shape-memory effect in certain alloys [7, 8, 9, 10, 11]. The applications of shape-memory alloys are varied, including use in actuators and medical and dental devices and implants. Diffusion-driven martensitic phase transformations occur in lithium-ion manganese oxide batteries [12]. In many of these examples, the underlying change in crystal lattice is from cubic to tetragonal, although several other transition types occur (e.g. cubic to orthorhombic, cubic to monoclinic) [7, 9, 10].

While titanium and titanium alloys are widely used materials, titanium oxides have also been proposed as useful materials in multiple applications, including medical implants [13, 14] and batteries [15]. The diffusion of oxygen in titanium alloys has also been explored for its hardening effects [16]. Titanium oxidizes to form a variety of oxides, including rutile [17, 18, 19], anatase TiO_2, and rock salt TiO [20, 21, 22, 23]. At low partial pressures of oxygen, ordered $TiO_{1/6}$, $TiO_{1/3}$, and $TiO_{1/2}$ suboxides can also form [1]. In addition to these oxides, a region of solid solution HCP TiO_x can exist below the oxide layer with compositions as high as $x = 1/2$ [24, 25]. As with other metals, oxidation can introduce voids that could negatively effect the material properties. There are multiple possible mechanisms driving the voiding process, including vacancy condensation and the effect of oxide stresses [26, 27].

Magnesium is an attractive structural material due to its low density (two thirds the density of aluminum and one quarter the density steel) and abundance in the Earth's crust [28, 29, 30, 31]. Poor mechanical properties such as yield strength, formability, creep resistance, and corrosion resistance, even in many alloys, limit its current use. Precipitation and age hardening in magnesium alloys play key roles in the improvement of material properties. Many studies and computational models have focused on understanding the properties of these precipitates, including those of promising Mg-Rare Earth alloys [32, 33, 34, 5, 35, 31, 3, 36, 37, 2].

1.2 Methodology

The difference in crystal structure between adjacent phases, whether it be between martensitic variants, oxide and metal, or precipitate and solid-solution phases, is a key element in the interactions between solid mechanics and chemistry. The effects of the mismatch in crystal structure are treated in a continuum setting in the formulations and methods presented in this dissertation. These continuum methods rely on material parameters describing the structure and free energy of each phase. This information can be predicted using atomistic methods such as first-principles statistical mechanics and density functional theory (DFT) [31, 38, 39, 40, 41, 42, 43, 44, 45, 46, 47, 48]. The numerical examples presented in the following chapters repeatedly rely on reported parameters determined through such methods.

Within the continuum setting, the solid mechanics are defined using a standard displacement field. Even when dynamics are introduced to model chemical diffusion, the solid mechanics are considered quasi-static. Where the chemical composition is variable, a (scalar) composition field is introduced. A variable crystal lattice can be represented using various methods. If completely dependent on the composition, no additional fields are needed. Otherwise, it is possible to introduce order parameters, such as those used in Allen-Cahn formulations, to identify regions of distinct crystal lattices [49]. It is also possible, as introduced in Chapters 2 and 3, to represent the crystal structure with a second kinematic (vector) field.

Each of the material examples in the previous section involve multiple phases with either coherent or incoherent interfaces. There are several possible ways to model the phase interfaces depending on the coherency of the interface and whether dynamics are included. An incoherent interface modeled in a dynamic setting can be represented using the level set method, where the zero level set of a field represents the sharp interface [50, 51]. The interface motion is governed by a specified interface velocity and partial differential equation. This method is used in Chapter 2. Evolving coherent

interfaces are represented in phase field methods using the Allen-Cahn and/or Cahn-Hilliard by a rapid but continuous change in a composition or order parameter field [52, 49]. The location and thickness of these diffuse interfaces are controlled by nonconvexities and gradient terms in the free energy function. Chapters 3, 4, and 5 demonstrate these phase field methods. When the location of a coherent interface is fixed and known, a signed distance function can be approximated near the interface and used to smoothly transition from the material parameters of one phase to those of another. This method is used in Chapter 5.

1.3 The free energy

A proper expression for the free energy of a substance is considered a fundamental equation from which all thermodynamic properties of the substance can be derived. Material properties such as heat capacity and compressiblity, as well as information about phase stability, are related to second derivatives. The first derivatives of the free energy are used to define equilibrium conditions [53].

When a system is at a stable equilibrium, the free energy is at a minimum. Extremization of a function is accomplished by setting the first derivative equal to zero. The free energy is, in general, a functional rather than a function; that is, its value "depends upon the entire course or path of one or more functions rather than on a number of discrete variable," as is the case with all integrals and derivatives [54]. The method for minimizing a functional is provided by variational calculus. This is done by setting what is termed the *first variation* equal to zero, giving the weak form of the equilibrium conditions. From the first variation, the related *variational derivative* and the partial differential equation in strong form can be derived [55]. This method of defining a free energy functional and setting the first variation to be zero is used throughout this dissertation for deriving the equilibrium conditions of solid mechanics.

The variational derivative also plays a role in modeling the dynamics when at nonequilibrium with respect to concentration of a species within a body. The variational derivative of the Gibbs free energy with respect to concentration is the chemical potential. A commonly used phenomenological law defines the flux in chemical diffusion to be proportional to the gradient of the chemical potential [53]. Chemical diffusion can be modeled by combining this definition of the flux, $\boldsymbol{J}$, with the conservation equation $\partial c/\partial t = -\nabla \cdot \boldsymbol{J}$. When the free energy and, hence, the chemical potential include gradient terms representing interfacial energy, this becomes the Cahn-Hilliard equation. The Cahn-Hilliard and the related Allen-Cahn equations are phase field models, which are able to model the time evolution of materials with multiple, concurrent phases [52, 49]. They are defined such that the free energy of the system decreases over time, eventually reaching equilibrium when appropriate boundary conditions are applied. Phase-field models are used in Chapters 3 through 5.

The problem of finding the energy minimizing state can also be considered as an optimization problem. For cases where a variable field or function can be represented by a set of discrete variables, traditional optimization techniques can be used. For situations where it is possible to evaluate the total free energy but impractical to calculate gradients, derivative-free optimization methods can be used [56]. These include, for example, genetic algorithms, simulated annealing, and surrogate-based optimization methods. Surrogate-based methods involve using a low-order or surrogate model to represent the objective function, i.e the free energy [57]. The surrogate model provides computationally efficient approximations to the gradient that can be used in the traditional gradient methods, such as gradient descent. Regression machine learning methods, such as Deep Neural Networks (DNN), can be used effectively as surrogate models in minimization problems, as demonstrated in Chapter 5 [58, 59, 60].

1.4 Goals and outline

The overarching goals of this dissertation are to provide additional methods and a mathematical framework that will allow for the testing of materials science hypotheses in a computational setting and provide guidance in the planning of experiments and designing of materials. Specific goals include the following:

- Demonstrate a mathematical framework that allows the methodical inclusion of multiple types of displacement or deformation (e.g. motion of phase boundaries, changes in crystal structure) and chemical species (see Chapters II and III).
- Allow for the use of realistic free energy data in a way that is computationally efficient (see Chapter IV).
- Use machine learning techniques to improve computation time in certain phase-field problems (see Chapter V).

An outline of the dissertation is as follows. Chapter II describes the treatment of evolving configurations in solids. The governing equations are found within a variational framework by allowing fluctuations in both the current and material configurations of the system. These equations include the standard Euler-Lagrange equations for nonlinear elasticity, as well as additional "configurational" equations. These configurational equations are applied in two specific cases, both describing phases changes in absence of chemical diffusion. The first is the migration of a sharp interface between two material phases, where the kinetic law is suggested by the configurational equations. This example is implemented numerically using the level set method. The second case describes changes in microstructure that occur throughout the body, resulting in multiple phases separated by diffuse interfaces. Martensitic transformations are an example of this type of phase change, in which cubic crystal structures morph into tetragonal structures. This is implemented using isogeometric analysis

(IGA) and gradient elasticity, due to the non-convexity of the free energy function describing the change in crystal structure.

In Chapter III, chemical diffusion is combined with the configurational treatment of Chapter II by incorporating the Cahn-Hilliard equation. It is used in describing the oxidation of titanium, where the underlying crystal structure evolves due to the interactions between chemical diffusion (oxygen and titanium) and mechanics (expansion of the oxide). An energy well representing voids is incorporated within the free energy function to induce vacancy condensation, and a phase field computation demonstrates the resulting void formation.

The method of mathematically representing the free energy of a single variable is considered in Chapter IV. This is done through a study comparing cubic splines and Redlich-Kister polynomials in fitting chemical potential data, which is integrated to find the free energy density function. For chemical potential data describing a system with multiple regions of phase separation, the cubic splines give a more accurate representation of the data compared to the traditional Redlich-Kister polynomials. Furthermore, when used in a Cahn-Hilliard phase field computation, the cubic spline provides a speed up of nearly an order of magnitude in computation time when compared to a high order polynomial of comparable fidelity.

Chapter V presents an alternate method of finding low energy material configurations using a surrogate based optimization method based on deep neural networks. This is done in the context of precipitates in magnesium alloys. Points on the free energy surface, consisting of strain, chemical, and interfacial energies, are computed. A deep neural network is trained to predict the total energy based on the precipitate geometry and composition. Precipitate shapes that minimize this energy can be quickly found using the neural network's surface, thus predicting the low energy, equilibrium precipitate shape. Additional computations focused at and near the initial estimated minimum are used to improve the estimate. This method is compared

with commonly used phase field methods, and the possible interactions between the two kinds of models are discussed.

Chapter VI summarizes and concludes the dissertation.

CHAPTER II

A variational treatment of material configurations with application to interface motion and microstructural evolution

This chapter presents a variational treatment of evolving configurations in solids[1]. Of interest are problems in which a kinematic field can be identified, which describes the essential aspects of the material's configuration, while another distinct field, the displacement, furnishes the kinematics necessary for representing the nonlinear elastic response. Such a separation is possible upon a suitable definition of configurations for the cases at hand. A series of mathematical steps can then follow: The total free energy can then be written as a functional of both the configurational and the displacement fields. With it, one can seek equilibrium states that render the free energy stationary with respect to both fields. The corresponding Euler-Lagrange equations governing the configurational and displacement fields can be solved. The motivation from physics comes of asking whether a solid under load can seek to reach equilibrium by varying some configurational degree of freedom that can be identified as being distinct from the displacement field.

[1]This chapter is based on the following paper: G. Teichert, S. Rudraraju, K. Garikipati, 2017. A variational treatment of material configurations with application to interface motion and microstructural evolution, *Journal of the Mechanics and Physics of Solids* 99, 338–356.

The somewhat abstract arguments laid out above have relevance to crystalline solids that undergo phase transformations coupled with elastic deformation: In a classical continuum setting, the elastic deformation is obtained from the displacement, which is the only kinematic field. No phenomena are sought to be modeled, other than the mapping of the reference to current placements. In this setting, the reference and material placements coincide, and most importantly, they are fixed. In contrast stands any phenomenon in which, the material configuration evolves from a *reference material configuration*, and can be represented, on a physical basis, by a configurational field that is distinct from the displacement field. Here, the focus is on two specific examples: (a) In a multi-phase solid where phase change occurs at interphase interfaces, the configurational field would represent interface migration. The phase, and therefore the crystal structure at a material point will change if the interface migrates through that point. This causes a change in the material configuration of the point. Since the crystal structure (material configuration) changes across the mathematically sharp interface, the latter is incoherent. (b) Alternately, in a multi-phase solid, the crystal structure may change smoothly from one phase to another over an interface that has finite width, rather than being mathematically sharp. In this case also, the material configuration evolves with the crystal structure. Clearly, this would be a case of coherent interphase interfaces. Here too, the configurational field would represent the crystal structure at any point in the solid as a map from some well-defined, reference material configuration.

In each of cases a and b, with the evolved material configuration determined as above, the displacement field can be defined as the point-to-point map from this configuration to the current/deformed placement that lies in the spatial manifold. An elastic deformation can then be identified from this displacement field.

With two distinct kinematic fields thus identified, the response of the solid can be described by parameterizing the free energy functional in terms of these two fields.

The imposition of equilibrium as the conditions of stationarity under variations on the configurational and displacement fields reveals two sets of Euler-Lagrange equations. As expected, one set contains the standard partial differential equations of elasticity. The second set is novel, and consists of partial differential equations and accompanying boundary conditions that involve the conventional elastic stress, the Eshelby stress, as well as a distinct configurational stress.

The treatment of a configurational force, distinct from standard, Newtonian, forces acting on imperfections in a crystal lattice was given by Eshelby [61], building off work from the late nineteenth century [62, 63]. The last two decades have seen a resurgence in the literature on configurational forces. Some of the theoretical underpinnings can be found in references— [64, 65, 66, 67, 68] and [69]. Applications have also been developed, such as to finite element discretization [70], to the dynamics of defects [71], to spatial and material covariant balance laws [72] for modeling elastic inclusions [73], and to fracture mechanics [74]. Configurational force equations can be derived in the setting of classical balance laws, or, with appropriate assumptions, within a variational framework. Gurtin [64] regards configurational forces as fundamental quantities in continuum physics, analogous to standard forces. On that premise, he regards configurational balance laws as the corresponding, fundamental laws that must exist in order to govern these forces. This has led to a debate on whether new physics is posited by the introduction of configurational forces [68, 75]. The work presented here lies within a variational setting, and circumvents this debate by relying on the (perhaps) more accepted notion of equilibrium to arrive at balance laws as Euler-Lagrange equations of free energy functionals. The resulting partial differential equation for configurational equilibrium also arises in the work by Gurtin [64] and Maugin [68], where it has been called the fully material equilibrium equation.

The problem of configurational changes taking place at a sharp, migrating interface between two solid material phases is considered first. It is shown that the

variational method produces a partial differential equation of configurational equilibrium in addition to the standard partial differential equation of elasticity. Assuming satisfaction of quasi-static elastic equilibrium, the partial differential equation for configurational equilibrium is identically satisfied everywhere except on the interface itself. There, it takes the form of a jump condition, which also vanishes if equilibrium is satisfied at the interface. However, it is of interest to consider solids that are far from equilibrium, and therefore have migrating interfaces. Then, the second law of thermodynamics provides guidance for choosing a sufficient form for the interface velocity. The well-known and widely-used level set method [50] is adopted to track the interface's motion based on this velocity. Just a few of a vast number of level set applications are listed here: Barth & Sethian [51] modeled an isotropic etching process with a constant velocity and a directional etching process with a velocity dependent on the interface orientation. Macklin & Lowengrub [76] modeled tumor growth with a curvature dependent velocity. The interface velocity in oxidation problems [77, 78], [79] is based on material composition. Finally, it is of interest to note that Kalpakides & Arvanotakis [80] used a velocity based on configurational forces to model ferroelastic materials, although it is arrived at differently than in the present work.

The next problem considered is that of smoothly varying configurational changes in crystal structure that occur over interfaces of finite width. The smoothness implies that the configurational change extends over finite sub-volumes and transforms the crystal structure from the parent to the daughter phases. Therefore, it is in contrast to the case of phase transformation only at a migrating sharp interface. The configurational change of the crystal structure over the volume suggests that there is a contribution to the free energy density function, which is associated with this configurational field. The variational treatment based on stationarity of the free energy functional leads to a partial differential equation for configurational balance that

holds throughout the volume of the crystalline solid. There is therefore a fundamental difference in the form of the governing equations from that for phase changes that occur only at a sharp interface. The variational setup, however, is similar in both problems. Such a consideration of configurational change that occurs over the volume of a material was attempted, albeit in a limited manner, by Garikipati et al. [81] in the context of remodeling in biology. Since the parent and daughter crystal structures are equilibrium structures under suitable conditions, the free energy density function must exhibit local minima in configurational tangent space corresponding to these structures. The free energy density function is therefore non-convex and admits microstructures, thus placing the problem in a class that has spawned a rich mathematical literature [82, 83, 10]. It also is well-known that the non-convex free energy density functions must be enhanced by terms that penalize gradients in the tangent maps of the configurational variables for mathematical well-posedness and physically meaningful solutions [84]. Such considerations were accounted for by Rudraraju ad co-workers [85, 86], who treated non-convex free energy density-driven microstructure formation in nonlinear gradient elasticity following Toupin [87]. This treatment is extended to the configurational field in this communication.

Our treatment begins with consideration of the problem where the configurational change is restricted to a sharp interface in Section 2.1, and then moves on to the problem of smoothly varying configurational change over a diffuse interface in Section 2.2. The treatment is illustrated by numerical examples in both sections. Concluding remarks appear in Section 2.3.

2.1 Configurational change restricted to a sharp interface

Consider a body that is an open set $\Omega \subset \mathbb{R}^3$ with two open subsets, Ω_α and Ω_β consisting of phases α and β, respectively, that meet at a sharp interface $\Gamma \subset \Omega$. Here Γ is a 2-manifold that can be constructed as a mapping $\Gamma : \mathbb{R}^2 \mapsto \mathbb{R}^3$ (see Figure 2.1).

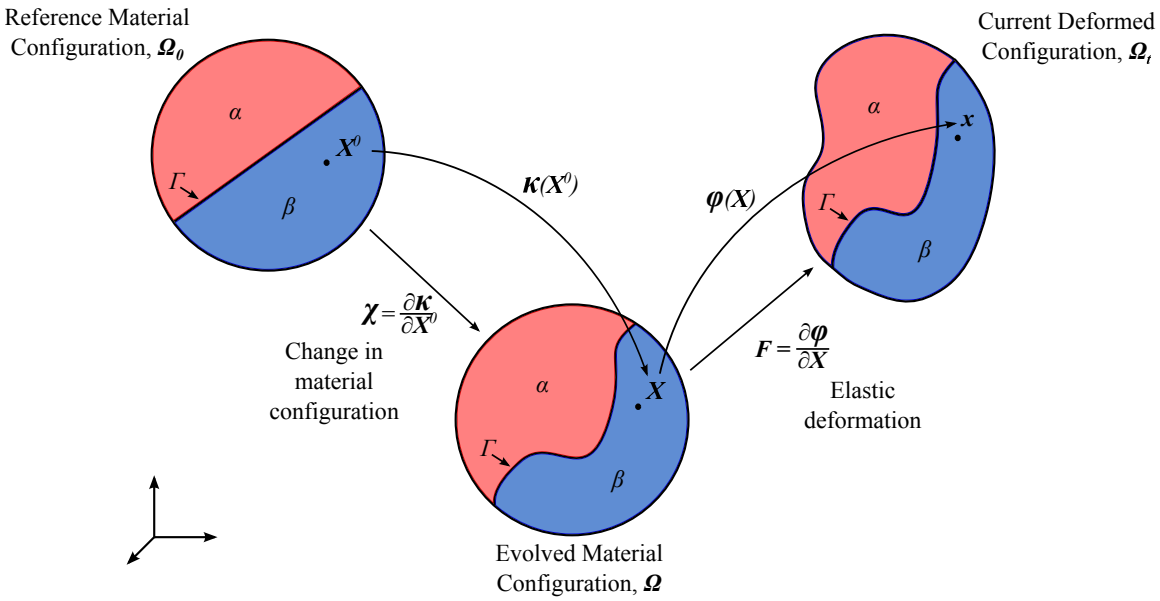

Figure 2.1: Kinematics of the configurational changes and elastic deformations with a sharp interface.

Let

$$\begin{aligned} \overline{\Omega} &= \overline{\Omega_\alpha \cup \Omega_\beta} \\ \overline{\Gamma} &= \partial\Omega_\alpha \cap \partial\Omega_\beta \\ \partial\Omega &= \partial\Omega_\alpha \cup \partial\Omega_\beta \setminus \Gamma \end{aligned} \tag{2.1}$$

The traditional traction boundary, where external, standard tractions can be imposed, is denoted by $\partial\Omega_T^{\mathrm{S}}$, while the traction-like boundary related to changes in material configuration is $\partial\Omega_T^{\mathrm{M}}$. This description is of the body in some material configuration.

It is supposed that the body has arrived at the above configuration by undergoing a phase transformation from the reference material configuration Ω_0, characterized by motion of the interface from its reference configuration Γ_0 to Γ in configurational space. The reference material configurations of Ω_α and Ω_β are, respectively, Ω_{α_0} and Ω_{β_0}. The point-to-point map $\boldsymbol{\kappa}$ is from the reference material configuration Ω_0 onto

the evolved material configuration Ω.

$$\boldsymbol{X} = \boldsymbol{\kappa}(\boldsymbol{X}^0) = \boldsymbol{X}^0 + \boldsymbol{U} \tag{2.2}$$

$$\boldsymbol{\chi} = \frac{\partial \boldsymbol{\kappa}}{\partial \boldsymbol{X}^0} = \mathbb{1} + \frac{\partial \boldsymbol{U}}{\partial \boldsymbol{X}^0} \tag{2.3}$$

Here, $\boldsymbol{X}^0$ and $\boldsymbol{X}$ are the reference and evolved values of the configurational field. The field $\boldsymbol{U}$ will be referred to as the configurational displacement, since it describes the change in material configuration through the evolution of the phases and their interface.

The elastic deformation of the body is described in the standard manner based on the mapping $\boldsymbol{\phi} : \Omega \mapsto \Omega_t$, defined as:

$$\boldsymbol{x} = \boldsymbol{\phi}(\boldsymbol{X}) = \boldsymbol{X} + \boldsymbol{u} \tag{2.4}$$

where $\boldsymbol{u}$ is the standard displacement field. The elastic deformation gradient is then defined as

$$\boldsymbol{F} = \frac{\partial \boldsymbol{\phi}}{\partial \boldsymbol{X}^0} \frac{\partial \boldsymbol{X}^0}{\partial \boldsymbol{X}} = \frac{\partial \boldsymbol{\phi}}{\partial \boldsymbol{X}} = \mathbb{1} + \frac{\partial \boldsymbol{u}}{\partial \boldsymbol{X}} \tag{2.5}$$

These variables can also be written in terms of $\boldsymbol{X}^0$, as follows:

$$\boldsymbol{x} = \boldsymbol{\phi}(\boldsymbol{\kappa}(\boldsymbol{X}^0)) = \boldsymbol{X}^0 + \boldsymbol{U} + \boldsymbol{u} \tag{2.6}$$

$$\boldsymbol{F} = \left(\mathbb{1} + \frac{\partial \boldsymbol{U}}{\partial \boldsymbol{X}^0} + \frac{\partial \boldsymbol{u}}{\partial \boldsymbol{X}^0} \right) \left(\mathbb{1} + \frac{\partial \boldsymbol{U}}{\partial \boldsymbol{X}^0} \right)^{-1} \tag{2.7}$$

It is important to note the distinctions between the configurational map, $\boldsymbol{\kappa}$ and the deformation map $\boldsymbol{\phi}$, their respective tangent maps $\boldsymbol{\chi}$ and $\boldsymbol{F}$, and the associated configurational and standard displacement fields $\boldsymbol{U}$ and $\boldsymbol{u}$.

The Gibbs free energy of the system is given by the following functional defined over Ω, where $\psi^\alpha(\boldsymbol{F}, \boldsymbol{X})$ and $\psi^\beta(\boldsymbol{F}, \boldsymbol{X})$ are the strain energy density functions for

the two phases:

$$\Pi[\boldsymbol{u};\boldsymbol{U}] = \int_{\Omega_\alpha} \psi^\alpha(\boldsymbol{F},\boldsymbol{X})\,\mathrm{d}V + \int_{\Omega_\beta} \psi^\beta(\boldsymbol{F},\boldsymbol{X})\,\mathrm{d}V - \int_{\Omega} \boldsymbol{f}(\boldsymbol{X})\cdot\boldsymbol{u}\,\mathrm{d}V - \int_{\partial\Omega^{\mathrm{S}}_T} \boldsymbol{T}\cdot\boldsymbol{u}\,\mathrm{d}S \tag{2.8}$$

A change of variables is performed to define the functional over Ω_0, noting that constancy of the traction loading during configurational change implies that $\boldsymbol{T}\mathrm{d}S = \boldsymbol{T}^0\mathrm{d}S_0$:

$$\Pi[\boldsymbol{u};\boldsymbol{U}] = \int_{\Omega_{\alpha_0}} \psi^\alpha(\boldsymbol{F},\boldsymbol{\kappa}(\boldsymbol{X}^0))\det\boldsymbol{\chi}\,\mathrm{d}V_0 + \int_{\Omega_{\beta_0}} \psi^\beta(\boldsymbol{F},\boldsymbol{\kappa}(\boldsymbol{X}^0))\det\boldsymbol{\chi}\,\mathrm{d}V_0 - \int_{\Omega_0} \boldsymbol{f}(\boldsymbol{\kappa}(\boldsymbol{X}^0))\cdot\boldsymbol{u}\det\boldsymbol{\chi}\,\mathrm{d}V_0 - \int_{\partial\Omega^{\mathrm{S}}_{T_0}} \boldsymbol{T}^0\cdot\boldsymbol{u}\,\mathrm{d}S_0 \tag{2.9}$$

2.1.1 Variational formulation

Variations are considered on the configurational displacement, $\boldsymbol{U}^\varepsilon := \boldsymbol{U} + \varepsilon\boldsymbol{W}$, and on the standard displacement, $\boldsymbol{u}^\varepsilon := \boldsymbol{u} + \varepsilon\boldsymbol{w}$. The first variation is computed using the functional defined over the fixed, reference material configuration Ω_0. A complete derivation is presented in A. Note that the two integrals $\int_{\Omega_\alpha}\psi^\alpha$ and $\int_{\Omega_\beta}\psi^\beta$ are expressed with a single integral $\int_\Omega\psi$.

$$\frac{\mathrm{d}}{\mathrm{d}\varepsilon}\Pi[\boldsymbol{u}^\varepsilon;\boldsymbol{U}^\varepsilon]\bigg|_{\varepsilon=0} = \frac{\mathrm{d}}{\mathrm{d}\varepsilon}\bigg\{ \int_{\Omega_0} \psi(\boldsymbol{F}^\varepsilon,\boldsymbol{\kappa}^\varepsilon(\boldsymbol{X}^0))\det\boldsymbol{\chi}^\varepsilon\,\mathrm{d}V_0 - \int_{\Omega_0} \boldsymbol{f}(\boldsymbol{\kappa}^\varepsilon(\boldsymbol{X}^0))\cdot\boldsymbol{u}^\varepsilon\det\boldsymbol{\chi}^\varepsilon\,\mathrm{d}V_0 - \int_{\partial\Omega^{\mathrm{S}}_{T_0}} \boldsymbol{T}^0\cdot\boldsymbol{u}^\varepsilon\,\mathrm{d}S_0\bigg\}\bigg|_{\varepsilon=0} \tag{2.10}$$

At equilibrium, the first variation of the Gibbs free energy is zero: $[\mathrm{d}\Pi/\mathrm{d}\varepsilon]_{\varepsilon=0} = 0$. The first variations of $\boldsymbol{F}$ and $\det\boldsymbol{\chi}$ are derived from equations (2.7) and (2.3), respectively:

$$\frac{d\boldsymbol{F}^{\varepsilon}}{d\varepsilon} = \left[\frac{\partial \boldsymbol{w}}{\partial \boldsymbol{X}^0} + (\mathbb{1} - \boldsymbol{F}^{\varepsilon})\,\frac{\partial \boldsymbol{W}}{\partial \boldsymbol{X}^0}\right]\boldsymbol{\chi}^{\varepsilon-1} \tag{2.11}$$

$$\frac{d\det\boldsymbol{\chi}^{\varepsilon}}{d\varepsilon} = \mathbb{1} : \left(\frac{\partial \boldsymbol{W}}{\partial \boldsymbol{X}^0}\boldsymbol{\chi}^{\varepsilon-1}\right)\det\boldsymbol{\chi}^{\varepsilon} \tag{2.12}$$

Substituting (2.11) and (2.12) into (2.10) defining the first Piola-Kirchhoff stress as $\partial\psi/\partial\boldsymbol{F} = \boldsymbol{P}$, and using $d\boldsymbol{\kappa}^{\varepsilon}/d\varepsilon = \boldsymbol{W}$ and $d\boldsymbol{u}^{\varepsilon}/d\varepsilon = \boldsymbol{w}$ gives

$$\begin{aligned} 0 = &\int_{\Omega_0} \boldsymbol{P} : \left(\frac{\partial \boldsymbol{w}}{\partial \boldsymbol{X}^0}\boldsymbol{\chi}^{-1}\right)\det\boldsymbol{\chi}\,\mathrm{d}V_0 - \int_{\Omega_0}(\boldsymbol{f}\cdot\boldsymbol{w})\det\boldsymbol{\chi}\,\mathrm{d}V_0 \\ &+ \int_{\Omega_0}(\boldsymbol{P} - (\boldsymbol{f}\cdot\boldsymbol{u})\,\mathbb{1} + \boldsymbol{\mathcal{E}}) : \left(\frac{\partial \boldsymbol{W}}{\partial \boldsymbol{X}^0}\boldsymbol{\chi}^{-1}\right)\det\boldsymbol{\chi}\,\mathrm{d}V_0 \\ &+ \int_{\Omega_0}\left(\frac{\partial\psi}{\partial\boldsymbol{\kappa}} - \boldsymbol{u}\cdot\frac{\partial \boldsymbol{f}}{\partial\boldsymbol{\kappa}}\right)\cdot\boldsymbol{W}\det\boldsymbol{\chi}\,\mathrm{d}V_0 - \int_{\partial\Omega^{\mathrm{S}}_{T_0}} \boldsymbol{T}^0\cdot\boldsymbol{w}\,\mathrm{d}S_0 \end{aligned} \tag{2.13}$$

Following a number of previous authors [65, 66, 64] the term $\boldsymbol{\mathcal{E}} := \psi\mathbb{1} - \boldsymbol{F}^{\mathsf{T}}\boldsymbol{P}$ is recognized as the Eshelby stress tensor. This weak form is now rewritten on Ω:

$$\begin{aligned} 0 = &\int_{\Omega} \boldsymbol{P} : \frac{\partial \boldsymbol{w}}{\partial \boldsymbol{X}}\,\mathrm{d}V - \int_{\Omega}(\boldsymbol{f}\cdot\boldsymbol{w})\,\mathrm{d}V \\ &+ \int_{\Omega}(\boldsymbol{P} - (\boldsymbol{f}\cdot\boldsymbol{u})\,\mathbb{1} + \boldsymbol{\mathcal{E}}) : \frac{\partial \boldsymbol{W}}{\partial \boldsymbol{X}}\,\mathrm{d}V \\ &+ \int_{\Omega}\left(\frac{\partial\psi}{\partial\boldsymbol{X}} - \boldsymbol{u}\cdot\frac{\partial \boldsymbol{f}}{\partial\boldsymbol{X}}\right)\cdot\boldsymbol{W}\,\mathrm{d}V - \int_{\partial\Omega^{\mathrm{S}}_{T}} \boldsymbol{T}\cdot\boldsymbol{w}\,\mathrm{d}S \end{aligned} \tag{2.14}$$

The strong form is derived from the weak form using standard variational arguments. In equation (2.14) discontinuities are allowed at the phase interface in all fields except $\boldsymbol{W}$ and $\boldsymbol{w}$. The corresponding strong form consists of the two following sets of

equations. The first set (2.15a - 2.15c) represents the standard governing partial differential equations and boundary conditions of nonlinear elasticity, now extended to include an interface Γ. The second set of equations (2.15d - 2.15f) has been simplified under the assumption that the preceding equations of nonlinear elasticity are satisfied. The operator $\nabla\cdot$ is used here to refer to the divergence with respect to $\boldsymbol{X}$. Note that $\boldsymbol{N}$ is the unit normal to the boundary of the body, and $\boldsymbol{N}^{\Gamma}$ is the normal to the interface.

$$\boldsymbol{P}\boldsymbol{N} - \boldsymbol{T} = 0 \text{ on } \partial\Omega_T^{\mathrm{S}} \tag{2.15a}$$

$$[\![\boldsymbol{P}\boldsymbol{N}^{\Gamma}]\!] = 0 \text{ on } \Gamma \tag{2.15b}$$

$$\nabla\cdot\boldsymbol{P} + \boldsymbol{f} = 0 \text{ in } \Omega \tag{2.15c}$$

$$\left(\boldsymbol{\mathcal{E}} + \boldsymbol{P} - (\boldsymbol{f}\cdot\boldsymbol{u})\mathbb{1}\right)\boldsymbol{N} = 0 \text{ on } \partial\Omega_T^{\mathrm{M}} \tag{2.15d}$$

$$[\![\left(\boldsymbol{\mathcal{E}} - (\boldsymbol{f}\cdot\boldsymbol{u})\mathbb{1}\right)\boldsymbol{N}^{\Gamma}]\!] = 0 \text{ on } \Gamma \tag{2.15e}$$

$$\nabla\cdot\boldsymbol{\mathcal{E}} - \frac{\partial\psi}{\partial\boldsymbol{X}} - \boldsymbol{F}^{\mathsf{T}}\boldsymbol{f} = 0 \text{ in } \Omega \tag{2.15f}$$

Note that equation (2.15f) corresponds exactly to the partial differential equation derived in [64] and [68]. This reduces further, using coordinate notation for clarity, with lower case indices for objects defined on Ω_t and upper case indices for objects defined on Ω.

$$\begin{aligned}
\left(\psi\delta_{IJ} - F_{iI}P_{iJ}\right)_{,J} - \frac{\partial\psi}{\partial X_I} - F_{iI}f_i &= 0 \\
\frac{\partial\psi}{\partial F_{iJ}}F_{iJ,I} + \frac{\partial\psi}{\partial X_I} - F_{iI,J}P_{iJ} - F_{iI}P_{iJ,J} - \frac{\partial\psi}{\partial X_I} - F_{iI}f_i &= 0 \\
P_{iJ}F_{iJ,I} - F_{iI,J}P_{iJ} - F_{iI}P_{iJ,J} - F_{iI}f_i &= 0
\end{aligned} \tag{2.16}$$

Using the relation $F_{iI,J} = F_{iJ,I}$ and $P_{iJ,J} = -f_i$ from equation (2.15c), this equation vanishes identically. Thus, if the standard governing partial differential equation for

nonlinear elasticity, $P_{iJ,J} + f_i = 0$ in Ω is satisfied, the corresponding configurational partial differential equation $\mathcal{E}_{IJ,J} - \frac{\partial \psi}{\partial X_I} - F_{iI} f_i = 0$ in Ω is trivially satisfied.

2.1.2 Interfacial energy

Interfacial energy can be included by adding the integral

$$\Pi^\Gamma = \int_\Gamma \psi^\Gamma \, \mathrm{d}S \tag{2.17}$$

to the free energy functional Π, where ψ^Γ is the interfacial free energy density. Assuming ψ^Γ is a constant, the first variation of this integral is

$$\begin{aligned} \frac{\delta \Pi^\Gamma}{\delta \boldsymbol{U}} \cdot \boldsymbol{W} = &\int_\Gamma -2\psi^\Gamma H \left(\boldsymbol{W} \cdot \boldsymbol{N}^\Gamma \right) \, \mathrm{d}S \\ &- \oint_{\partial\Gamma} \psi^\Gamma \boldsymbol{W} \cdot \left(\boldsymbol{N} \times \boldsymbol{T}^\Gamma \right) (\boldsymbol{N}^\Gamma \cdot \boldsymbol{N}) \boldsymbol{T}^\Gamma \cdot \mathrm{d}\boldsymbol{r} \end{aligned} \tag{2.18}$$

where H is the mean curvature of Γ. This term would affect equation (2.15e) and add a condition over $\partial\Gamma$, resulting in the following:

$$\left([\![\boldsymbol{\mathcal{E}} - (\boldsymbol{f} \cdot \boldsymbol{u}) \mathbb{1}]\!] - 2\psi^\Gamma H \mathbb{1} \right) \boldsymbol{N}^\Gamma = 0 \text{ on } \Gamma \tag{2.19a}$$

$$\psi^\Gamma \boldsymbol{N}^\Gamma \cdot \boldsymbol{N} = 0 \text{ on } \partial\Gamma_T \tag{2.19b}$$

A full derivation is included in B.

2.1.3 Nonequilibrium with respect to material evolution

Suppose that the body is at equilibrium everywhere except with respect to configurational evolution of the interface, Γ. Then, as the foregoing treatment demonstrates,

the first variation of the free energy reduces to

$$\frac{\delta \Pi}{\delta \boldsymbol{U}} \cdot \boldsymbol{W} = \int_{\Gamma} \boldsymbol{W} \cdot \left[\left([\![\boldsymbol{\mathcal{E}} - (\boldsymbol{f} \cdot \boldsymbol{u}) \mathbb{1}]\!] - 2\psi^{\Gamma} H \mathbb{1} \right) \boldsymbol{N}^{\Gamma} \right] \, \mathrm{d}S \tag{2.20}$$

The field $\boldsymbol{W}$ represents variation of the interface. In a rate formulation, this would be replaced by the interface velocity $\boldsymbol{V}_{\Gamma}$.

$$\dot{\Pi} = \int_{\Gamma} \boldsymbol{V}_{\Gamma} \cdot \left[\left([\![\boldsymbol{\mathcal{E}} - (\boldsymbol{f} \cdot \boldsymbol{u}) \mathbb{1}]\!] - 2\psi^{\Gamma} H \mathbb{1} \right) \boldsymbol{N}^{\Gamma} \right] \, \mathrm{d}S \tag{2.21}$$

The interface velocity can be defined by

$$\boldsymbol{V}_{\Gamma} = -\boldsymbol{M} \left[\left([\![\boldsymbol{\mathcal{E}} - (\boldsymbol{f} \cdot \boldsymbol{u}) \mathbb{1}]\!] - 2\psi^{\Gamma} H \mathbb{1} \right) \boldsymbol{N}^{\Gamma} \right] \tag{2.22}$$

with $\boldsymbol{M}$ a positive definite tensor to ensure decrease in free energy ($\dot{\Pi} \leq 0$), thus satisfying the second law of thermodynamics. The presence of H in the interface velocity makes this a general curvature driven flow.

2.1.4 Numerical treatment

The level set method is used for movement of the sharp interface in the case of nonequilibrium with respect to material evolution. All partial differential equations are solved using the finite element method.

2.1.4.1 Level set method

In the level set method, the interface is represented by the zero contour or level set of a scalar field, $\Phi(\boldsymbol{X}, t)$ [50]. The evolution of Φ (and the zero level set) is governed by the following partial differential equation:

$$\frac{\partial \Phi}{\partial t} = -v |\nabla \Phi| \tag{2.23}$$

where the scalar v is the advection velocity (i.e. the normal component of the level set velocity). The behavior of the level set evolution is improved when Φ is a signed distance function. Replacing v with v_e helps to maintain this property, where v_e is the *extensional velocity*, defined as the advection velocity at the closest point on the zero level set. This "closest point" generally does not coincide with a node or an integration point. Additionally, the field Φ is periodically reinitialized as a signed distance function based on the current location of the zero level set. The method of reinitialization used here involves solving the Eikonal equation $|\nabla\Phi| = 1$, using the following partial differential equation [88] with additional constraints on Φ to reduce spurious movement of the zero level set:

$$\begin{aligned} \frac{\partial\Phi}{\partial\hat{t}} &= \operatorname{sgn}(\Phi_0)(1 - |\nabla\Phi|) \\ \Phi_0(\boldsymbol{X}) &= \Phi(\boldsymbol{X}, 0) \end{aligned} \tag{2.24}$$

Note that $\hat{t}$ is a time-like parameter introduced only to allow relaxation of Φ to a signed distance function during reinitialization.

2.1.4.2 Finite element methods

Both the level set equation and the Eikonal equation used in reinitialization are solved using finite element methods. To reduce spatial oscillations common to advection-diffusion equations, the streamline upwind/Petrov-Galerkin (SUPG) weak form is used [89]:

$$\begin{aligned} \tilde{w} &= w + \tau\frac{\boldsymbol{v}\cdot\nabla w}{|\boldsymbol{v}|} \\ \int_\Omega \tilde{w}\frac{\partial\Phi}{\partial t}\,\mathrm{d}V &= -\int_\Omega \tilde{w}v_e|\nabla\Phi|\,\mathrm{d}V \end{aligned} \tag{2.25}$$

Since the value of Φ is only needed near the zero level set, the level set equation is only solved within a narrow band about the zero level set. The elastic, finite deformation of the body is modeled using the Bubnov-Galerkin weak form. The elasticity problem is solved over the entire domain using the field Φ to determine material properties at each integration point.

2.1.5 Numerical simulation

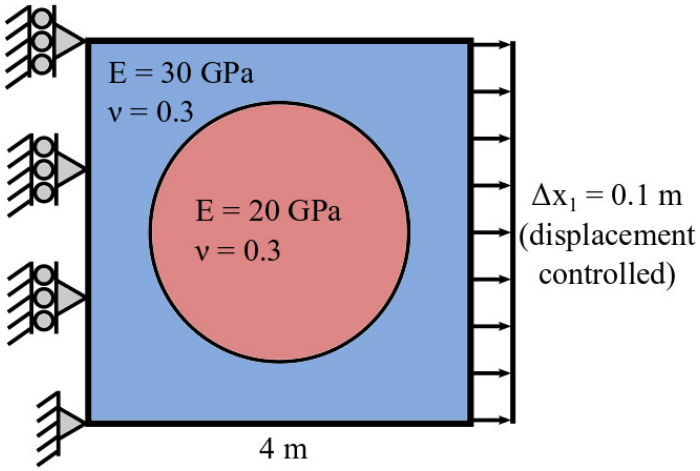

Figure 2.2: An example problem of sharp interface motion driven by displacement controlled, uniaxial tension.

Figures 2.2 - 2.5 present the plane strain computation of a two-phase material with a migrating sharp interface, under vanishing body force and zero interfacial energy. The initial phase distribution is as shown in Figure 2.2, with a compliant phase (Young's modulus $E = 20$ GPa) surrounded by a stiffer phase ($E = 30$ GPa). All other material properties and the chemical free energy density are taken to be the same for both phases. The body is subjected to displacement controlled, uniaxial tension. At each time step, the interface motion is modeled via the level set equation, and the current elastic deformation is found based on the updated interface location. The zero level set velocity is found using equation 2.22. A time step of .001 s was

used, with M equal to the isotropic tensor multiplied by 2e-8 $m^3/(Ns)$. The problem was allowed to evolve for 7000 time steps.

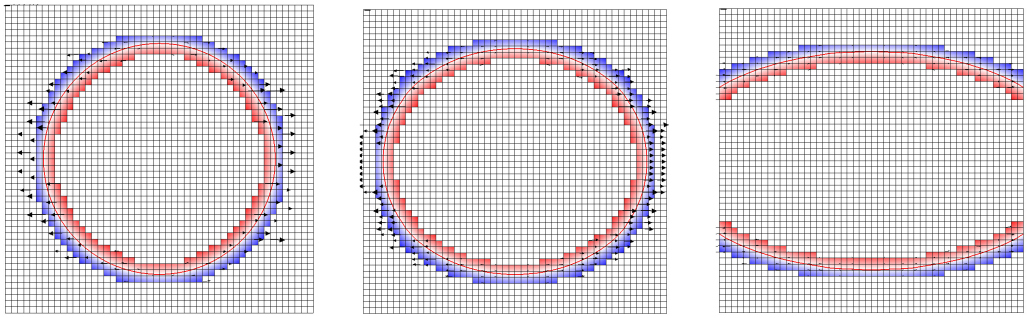

(a): Time step = 1 (b): Time step = 50 (c): Time step = 250

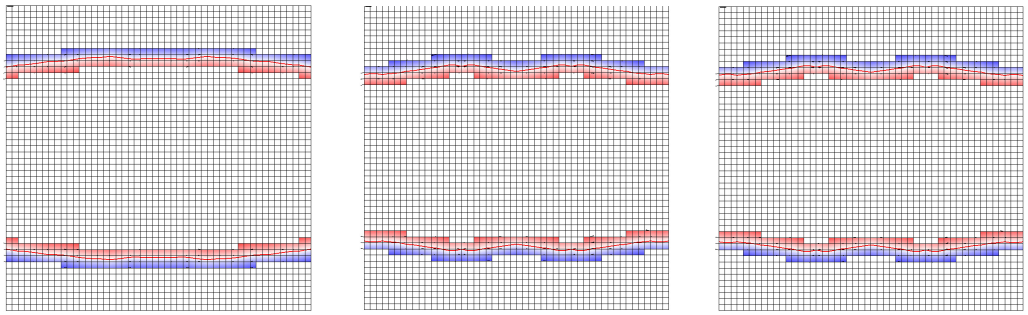

(d): Time step = 1000 (e): Time step = 4000 (f): Time step = 7000

Figure 2.3: Evolution of the sharp interface in the evolved reference configuration Ω over time. The interface is represented by the zero level set (red line) and is updated over a narrow band enclosing the zero level set (colored elements). The velocity vectors of the level sets are shown, but nearly vanish at later times, and are therefore not discernible in (c–f).

Figure 2.3 shows the evolution of the zero level set as the interface moves in the evolved reference configuration Ω, driven by the jump in the Eshelby stress tensor. the dynamics of the problem slow down after about 4000 time steps, or 4 s. The time scale of the problem is consistent with the interface velocity, which is initially about 5 m/s, and the size of the domain. It is shown in Figure 2.4 that after 7000 time steps, all of the level set velocity vectors are nearly tangential to the level set. As a result, there is little movement normal to the zero level set. This is due to a large reduction in the jump in stress across the interface; there is still, however, a jump in the strain energy density.

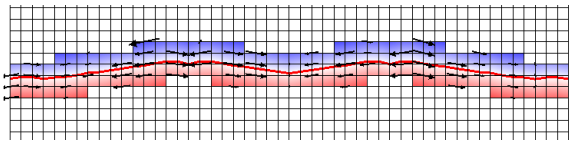

Figure 2.4: After 7000 time steps, the level set velocity vectors are all nearly tangential to the level sets (velocity vectors scaled 3x).

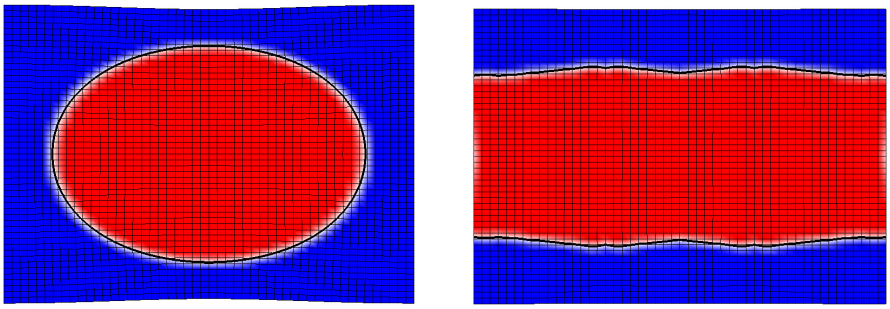

(a): Time step = 1 (b): Time step = 7000

Figure 2.5: Evolution of elastic deformation due to the change in material configuration (10x displacement shown).

The elastic deformation on the top and bottom edges of the body can be seen in Figure 2.5, which is in the current, deformed configuration Ω_t. Initially, that deformation is greatest in the middle, due to the concentration of the compliant phase in the center. However, the interface evolves in such a way that the elastic deformation along the edges becomes nearly uniform after 7000 time steps.

2.2 Configurational change over a volume; diffuse interfaces

The case of a solid that can undergo phase changes throughout the volume is treated in this section, considering again equilibrium with respect to both the configurational and standard displacements. As discussed in the Introduction, the material's configuration, represented by the crystal structure, varies smoothly between parent and daughter phases, thus creating diffuse interfaces between the phases (see Figure 2.6). In this case, the invertible map $\boldsymbol{\kappa}$ and its gradient, $\boldsymbol{\chi} = \partial\boldsymbol{\kappa}/\partial\boldsymbol{X}^0$, model the distortion of the crystal structure associated with the phase change. The mapping

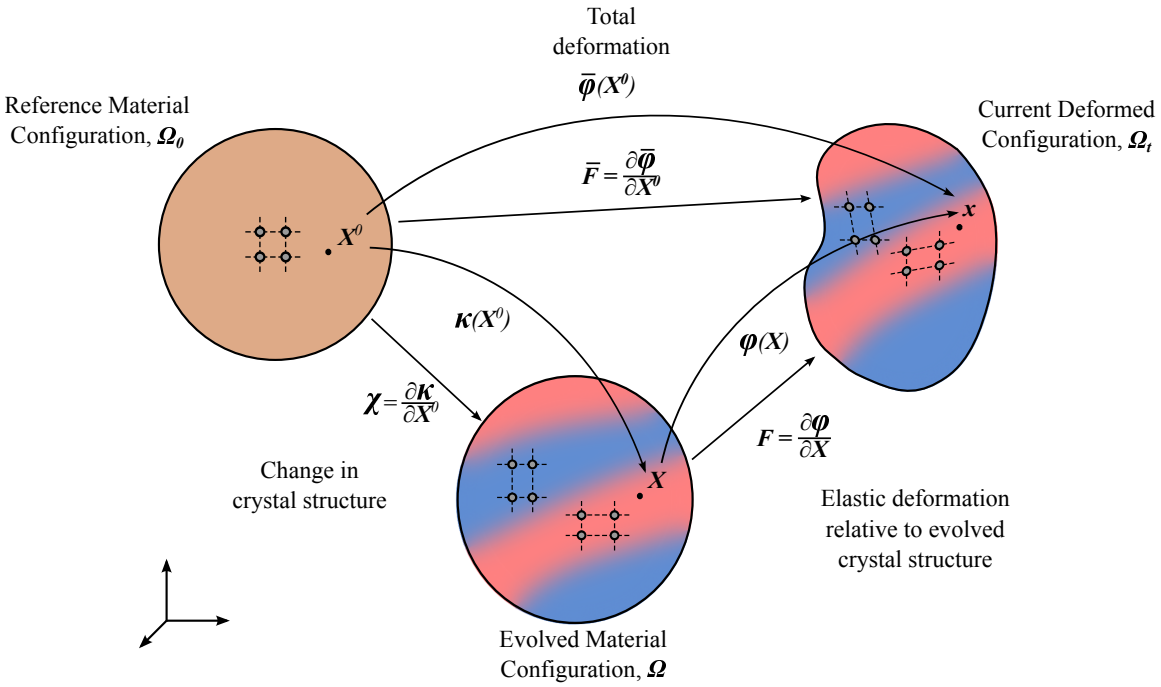

Figure 2.6: Kinematics of the configurational changes and elastic deformations causing a diffuse interface.

$\bar{\boldsymbol{\phi}}$ and gradient $\bar{\boldsymbol{F}}$ are introduced, giving the final placement of the body via configurational and standard displacements from the reference material configuration:

$$\boldsymbol{x} = \bar{\boldsymbol{\phi}}(\boldsymbol{X}^0) = \boldsymbol{X}^0 + \bar{\boldsymbol{u}} \tag{2.26}$$

$$\bar{\boldsymbol{F}} = \frac{\partial \bar{\boldsymbol{\phi}}}{\partial \boldsymbol{X}^0} = \mathbb{1} + \frac{\partial \bar{\boldsymbol{u}}}{\partial \boldsymbol{X}^0} \tag{2.27}$$

The deformation map $\boldsymbol{\phi}$ and deformation gradient $\boldsymbol{F}$ model standard elastic deformation relative to the evolved material configuration (distorted crystal structure) and are as defined previously.

2.2.1 The cubic to tetragonal transformation

To fix ideas, a diffusionless cubic to tetragonal transformation is considered here such as occurs in some martensitic transformations [7, 9, 10], although these methods have wider applicability to any smooth change in crystal structure. In the reference

material configuration, the solid is stable in the cubic crystal structure at high temperature. The free energy density function has a single well in this phase. A rapid quench is assumed to render the cubic phase unstable to a configurational change by distortion into tetragonal phase. Three such tetragonal variants are possible, and the solid is stable in any of these structures, implying that they are local minima of the free energy density. Furthermore the configurational change between one tetragonal variant and another is smooth, and these variants are separated by diffuse interfaces. In this phase, therefore, the solid's free energy density is a smooth, non-convex function of $\boldsymbol{\chi}$ with three minima corresponding to the three stable and equivalent tetragonal variants (Figure 2.7). A two-dimensional version of these configurational changes is the square to rectangle transformation (Figure 2.8), which serves well to fix ideas. The first numerical example in Section 2.2.4 will also return to two dimensions. While free energy functions with wells of equal depth are used as examples, there is nothing in this formulation that requires that the depths be equal.

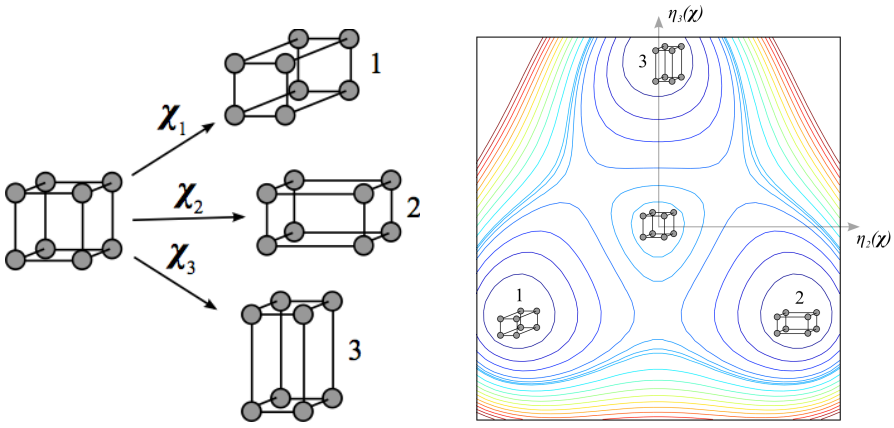

Figure 2.7: Tetragonal variants and free energy density contours in 3D. The axis, η_2 and η_3, are reparametrized strains.

2.2.2 Free energy density functions

The free energy density function associated with the configurational changes described above is $\psi^{\mathrm{M}} = \hat{\psi}^{\mathrm{M}}(\boldsymbol{X}^0, \boldsymbol{\chi}, \nabla^0\boldsymbol{\chi})$. The operator ∇^0 is used to refer to deriva-

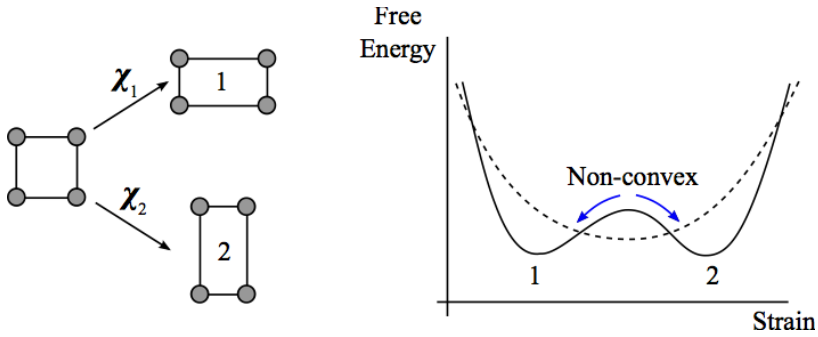

Figure 2.8: Tetragonal variants and free energy density schematic in 2D.

tives with respective to $\boldsymbol{X}^0$ for brevity in notation. This function allows for inhomogeneity via $\boldsymbol{X}^0$ and, as discussed in Section 2.2.1, is dependent on the tangent map of the configurational field $\boldsymbol{\chi}$. Since ψ^{M} is non-convex in the tetragonal phase, it allows the development of microstructures formed by laminae of the tetragonal variants, as discussed extensively in the literature. See [82, 83, 10] for a background discussion. As is also well-known, these microstructures can develop with arbitrary fineness unless the diffuse interfaces between sub-regions of a single variant are penalized. This is done by inclusion of a dependence on $\nabla^0\boldsymbol{\chi}$ for regularization [84, 85]. This ensures physically meaningful solutions and mathematical well-posedness. The free energy density function for the standard elastic deformation relative to Ω is $\psi^{\mathrm{S}} = \psi^{\mathrm{S}}(\boldsymbol{X}, \boldsymbol{F}, \boldsymbol{\chi})$, where $\boldsymbol{X} = \boldsymbol{\kappa}(\boldsymbol{X}^0)$. Similar to ψ^{M}, the elastic free energy depends on $\boldsymbol{X}$ and the elastic deformation gradient $\boldsymbol{F}$. Anisotropic elastic response can be incorporated if ψ^{S} is made to depend on $\boldsymbol{\chi}$: The local value of $\boldsymbol{\chi}$ determines the tetragonal variant arising as a result of the configurational change, and therefore sets the anisotropy of response due to elastic deformation relative to this evolved material configuration, Ω. The free energy of the system is then modeled with the following

Gibbs free energy functional (Figure 2.9):

$$\Pi[\bar{\boldsymbol{u}};\boldsymbol{U}] = \int_{\Omega_0} \left[\psi^{\mathrm{M}}(\boldsymbol{X}^0, \boldsymbol{\chi}, \nabla^0\boldsymbol{\chi}) + \psi^{\mathrm{S}}(\boldsymbol{X}, \boldsymbol{F}, \boldsymbol{\chi}) \det \boldsymbol{\chi}\right] \mathrm{d}V_0 - \int_{\Omega_0} \boldsymbol{f}^0 \cdot \bar{\boldsymbol{u}} \, \mathrm{d}V_0 - \int_{\partial\Omega^{\mathrm{S}}_{T_0}} \boldsymbol{T}^0 \cdot \bar{\boldsymbol{u}} \, \mathrm{d}S_0 \tag{2.28}$$

Attention should be drawn to the definition of quantities relative to the reference material configuration, Ω_0, extending to the work terms of the body force and traction. This seems natural because $\boldsymbol{\kappa}$ corresponds to distortion of the crystal structure, and $\boldsymbol{\phi}$ is further motion relative to the distorted crystal. Therefore, the distributed forces are dual to the total displacement $\bar{\boldsymbol{u}} = \boldsymbol{U} + \boldsymbol{u}$.

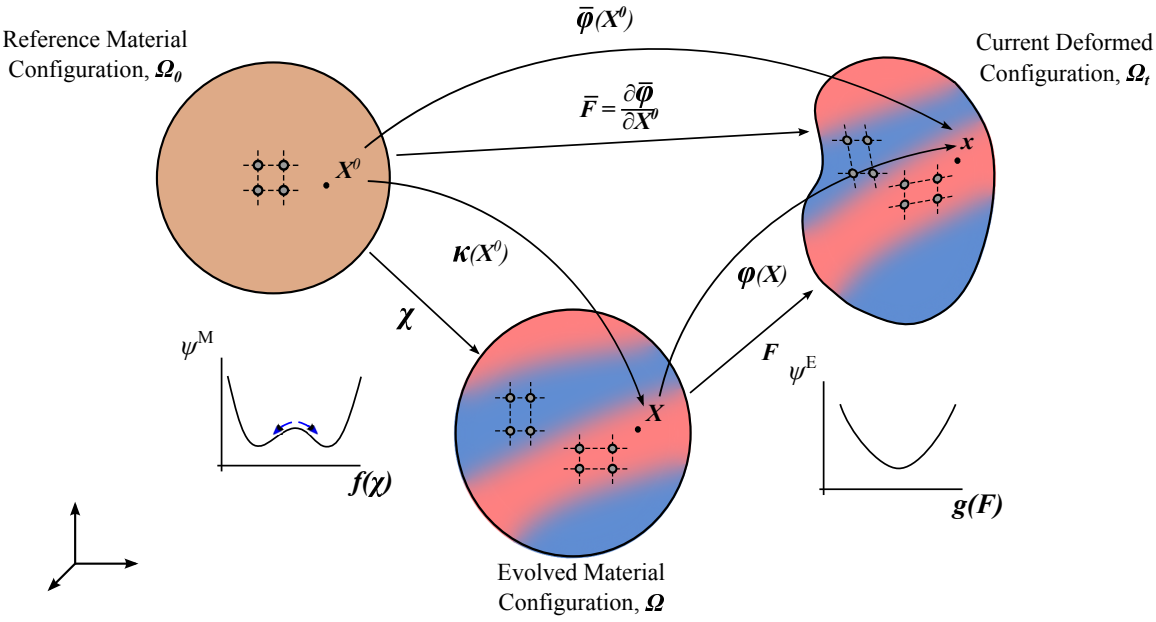

Figure 2.9: Schematic of the kinematics and free energy associated with evolution of the configuration and elastic deformation.

2.2.3 Variational formulation

Equilibrium conditions are again found by setting the first variation of the Gibbs free energy to vanish. Variations are condsidered on the configurational displacement,

$\boldsymbol{U}^\varepsilon := \boldsymbol{U} + \varepsilon \boldsymbol{W}$, and the total displacement, $\bar{\boldsymbol{u}}^\varepsilon := \bar{\boldsymbol{u}} + \varepsilon \bar{\boldsymbol{w}}$. Then, equilibrium requires

$$\begin{aligned}
\frac{\mathrm{d}}{\mathrm{d}\varepsilon}\Pi[\bar{\boldsymbol{u}}^\varepsilon; \boldsymbol{U}^\varepsilon]\bigg|_{\varepsilon=0} &= \frac{\mathrm{d}}{\mathrm{d}\varepsilon}\Bigg\{ \int_{\Omega_0} \psi^{\mathrm{M}}(\boldsymbol{X}^0, \boldsymbol{\chi}^\varepsilon, \nabla^0 \boldsymbol{\chi}^\varepsilon)\, \mathrm{d}V_0 \\
&\quad + \int_{\Omega_0} \psi^{\mathrm{S}}(\boldsymbol{X}^\varepsilon, \boldsymbol{F}^\varepsilon, \boldsymbol{\chi}^\varepsilon) \det \boldsymbol{\chi}^\varepsilon \, \mathrm{d}V_0 \\
&\quad - \int_{\Omega_0} \boldsymbol{f}^0 \cdot \bar{\boldsymbol{u}}^\varepsilon \, \mathrm{d}V_0 - \int_{\partial\Omega^{\mathrm{S}}_{T_0}} \boldsymbol{T}^0 \cdot \bar{\boldsymbol{u}}^\varepsilon \, \mathrm{d}S_0 \Bigg\}\Bigg|_{\varepsilon=0} \\
&= 0
\end{aligned} \tag{2.29}$$

The earlier results concerning the first variations of $\boldsymbol{F}$ and $\det \boldsymbol{\chi}$ are applied. Additional terms $\boldsymbol{D} := \partial\psi^{\mathrm{M}}/\partial\boldsymbol{\chi}$, $\boldsymbol{B} := \partial\psi^{\mathrm{M}}/\partial\nabla^0\boldsymbol{\chi}$ and $J_\chi := \det\boldsymbol{\chi}$ are defined.

The resulting weak form is the following:

$$\begin{aligned}
0 = &\int_{\Omega_0} \boldsymbol{B} \vdots \nabla^0\nabla^0 \boldsymbol{W} \, \mathrm{d}V_0 + \int_{\Omega_0} J_\chi \frac{\partial \psi^{\mathrm{S}}}{\partial \boldsymbol{X}} \cdot \boldsymbol{W} \, \mathrm{d}V_0 \\
&+ \int_{\Omega_0} \left[\boldsymbol{D} + J_\chi \left(\boldsymbol{\mathcal{E}} \boldsymbol{\chi}^{-\mathsf{T}} + \frac{\partial \psi^{\mathrm{S}}}{\partial \boldsymbol{\chi}} \right) \right] : \nabla^0 \boldsymbol{W} \, \mathrm{d}V_0 \\
&+ \int_{\Omega_0} J_\chi \left(\boldsymbol{P} \boldsymbol{\chi}^{-\mathsf{T}} \right) : \nabla^0 \bar{\boldsymbol{w}} \, \mathrm{d}V_0 - \int_{\Omega_0} \boldsymbol{f}^0 \cdot \bar{\boldsymbol{w}} \, \mathrm{d}V_0 - \int_{\partial\Omega^{\mathrm{S}}_{T_0}} \boldsymbol{T}^0 \cdot \bar{\boldsymbol{w}} \, \mathrm{d}S_0
\end{aligned} \tag{2.30}$$

Here, $\boldsymbol{D}$ is a configurational stress that is distinct from the Eshelby stress $\boldsymbol{\mathcal{E}}$, and $\boldsymbol{B}$ represents a higher order configurational stress. Deriving the strong form from this weak form involves several additional terms due to the dependence on $\nabla^0\boldsymbol{\chi}$, as described in [85]. The normal and surface gradient operators, ∇^n and ∇^s, are used, where

$$\nabla^n \psi = \nabla^0 \psi \cdot \boldsymbol{N}^0 \tag{2.31}$$

$$\nabla^s \psi = \nabla^0 \psi - (\nabla^n \psi)\, \boldsymbol{N}^0 \tag{2.32}$$

Also, $\boldsymbol{b} = -\nabla^s \boldsymbol{N}^0 = \boldsymbol{b}^{\mathsf{T}}$ is the second fundamental form of the smooth parts of the boundary, $\partial\Omega_0$. The term $\boldsymbol{N}^{\mathcal{C}} = \boldsymbol{\Xi} \times \boldsymbol{N}^0$ is defined, where $\boldsymbol{\Xi}$ is the unit tangent to the smooth curve $\mathcal{C}_0$ that forms an edge between subsets $\partial\Omega_0^+$ and $\partial\Omega_0^-$ of the smooth boundary surfaces $\partial\Omega_0$. If $\boldsymbol{N}^{\mathcal{C}^+}$ is the outward unit normal to $\mathcal{C}_0$ from $\partial\Omega_0^+$ and $\boldsymbol{N}^{\mathcal{C}^-}$ is the outward unit normal to $\mathcal{C}_0$ from $\partial\Omega_0^-$, then the term $[\![\boldsymbol{B} : \left(\boldsymbol{N}^{\mathcal{C}} \otimes \boldsymbol{N}^0\right)]\!]^{\mathcal{C}} := \boldsymbol{B} : \left(\boldsymbol{N}^{\mathcal{C}^+} \otimes \boldsymbol{N}^0\right) + \boldsymbol{B} : \left(\boldsymbol{N}^{\mathcal{C}^-} \otimes \boldsymbol{N}^0\right)$ is defined. Applying the appropriate integration by parts and standard variational arguments leads to the following strong form.

$$J_\chi \boldsymbol{P}\boldsymbol{\chi}^{-\mathsf{T}}\boldsymbol{N}^0 - \boldsymbol{T}^0 = 0 \text{ on } \partial\Omega_{T_0}^{\mathrm{M}} \tag{2.33a}$$

$$\nabla^0 \cdot \left(J_\chi \boldsymbol{P}\boldsymbol{\chi}^{-\mathsf{T}}\right) + \boldsymbol{f}^0 = 0 \text{ in } \Omega_0 \tag{2.33b}$$

$$[\![\boldsymbol{B} : \left(\boldsymbol{N}^{\mathcal{C}} \otimes \boldsymbol{N}^0\right)]\!]^{\mathcal{C}} = 0 \text{ on } \mathcal{C}_{T_0}^{\mathrm{M}} \tag{2.33c}$$

$$\boldsymbol{B} : \left(\boldsymbol{N}^0 \otimes \boldsymbol{N}^0\right) = 0 \text{ on } \partial\Omega_{T_0}^{\mathrm{S}} \tag{2.33d}$$

$$\boldsymbol{D}\boldsymbol{N}^0 + J_\chi \left(\boldsymbol{\mathcal{E}}\boldsymbol{\chi}^{-\mathsf{T}} + \frac{\partial \psi^{\mathrm{S}}}{\partial \boldsymbol{\chi}}\right)\boldsymbol{N}^0 - \boldsymbol{C} = 0 \text{ on } \partial\Omega_{T_0}^{\mathrm{S}} \tag{2.33e}$$

$$\nabla^0 \cdot \left(\boldsymbol{D} + J_\chi \frac{\partial \psi^{\mathrm{S}}}{\partial \boldsymbol{\chi}}\right) + \boldsymbol{F}^{\mathsf{T}}\boldsymbol{f}^0 - \nabla^0\nabla^0 \boldsymbol{B} = 0 \text{ in } \Omega_0 \tag{2.33f}$$

where, using coordinate notation for clarity,

$$\begin{aligned} C_I = {} & \nabla^n B_{I\gamma\zeta} N_\zeta^0 N_\gamma^0 + 2\nabla_\gamma^s B_{I\gamma\zeta} N_\zeta^0 \\ & + B_{I\gamma\zeta}\nabla_\gamma^s N_\zeta^0 - (b_{\xi\xi} N_\gamma^0 N_\zeta^0 - b_{\gamma\zeta}) B_{I\gamma\zeta} \end{aligned} \tag{2.34}$$

Details of the above derivations of weak and strong forms appear in C.

2.2.4 Numerical simulations

The following double well, free energy density function is used to represent the two-dimensional, square to rectangle transformation:

$$\boldsymbol{\Theta} = \tfrac{1}{2}(\boldsymbol{\chi}^{\mathsf{T}}\boldsymbol{\chi} - \mathbb{1}) \tag{2.35}$$

$$\eta_1 = \Theta_{11} + \Theta_{22},\ \eta_2 = \Theta_{11} - \Theta_{22},\ \eta_6 = \Theta_{12} \tag{2.36}$$

$$\psi^{\mathrm{M}} = \frac{d}{s^2}\left(\eta_1^2 + \eta_6^2\right) - \frac{2d}{s^2}\eta_2^2 + \frac{d}{s^4}\eta_2^4 + \frac{l^2 d}{s^2}|\nabla^0\eta_2|^2 \tag{2.37}$$

where the energy wells lie at $\eta_2 = \pm s$ with a depth of $-d$. Additionally, attention should be drawn to the last term in Equation (2.37), which is the gradient free energy contribution that regularizes the non-convex free energy density as discussed in Section 2.2.2. Using standard dimensional arguments this term has been scaled by a length parameter l, where $1/l^2$ is the ratio of standard to strain gradient moduli.

For the three-dimensional case, the following reparameterized strain space is used:

$$\begin{aligned}
&\eta_1 = \frac{1}{\sqrt{3}}(\Theta_{11} + \Theta_{22} + \Theta_{33}), \qquad \eta_2 = \frac{1}{\sqrt{2}}(\Theta_{11} - \Theta_{22}),\\
&\eta_3 = \frac{1}{\sqrt{6}}(\Theta_{11} + \Theta_{22} - 2\Theta_{33}), \qquad \eta_4 = \sqrt{2}\Theta_{23} = \sqrt{2}\Theta_{32},\\
&\eta_5 = \sqrt{2}\Theta_{13} = \sqrt{2}\Theta_{31}, \qquad \eta_6 = \sqrt{2}\Theta_{12} = \sqrt{2}\Theta_{21}
\end{aligned} \tag{2.38}$$

The corresponding free energy density function has three wells located at $(\frac{\sqrt{3}}{2}s, \frac{1}{2}s)$, $(-\frac{\sqrt{3}}{2}s, \frac{1}{2}s)$, and $(0, s)$ in (η_2, η_3) space with a depth of $-d$.

$$\begin{aligned}
\psi^{\mathrm{M}} = &\frac{3d}{2s^2}\left(\eta_1^2 + \eta_4^2 + \eta_5^2 + \eta_6^2\right) - \frac{3d}{2s^2}(\eta_2^2 + \eta_3^2) + \frac{3d}{2s^4}\left(\eta_2^2 + \eta_3^2\right)^2\\
&+ \frac{d}{s^3}\eta_3\left(\eta_3^2 - 3\eta_2^2\right) + \frac{3l^2 d}{2s^2}\left(|\nabla^0\eta_2|^2 + |\nabla^0\eta_3|^2\right)
\end{aligned} \tag{2.39}$$

Note the regularizing gradient free energy in the last two terms of Equation (2.39).

An anisotropic St. Venant-Kirchhoff model is used for the elastic deformation,

$$\psi^{\mathrm{S}} = \tfrac{1}{2}\boldsymbol{E} : \mathbb{C}(\boldsymbol{\chi}) : \boldsymbol{E} \tag{2.40}$$

where

$$\begin{aligned}\mathbb{C}(\boldsymbol{\chi}) = &\sum_{I=1}^{3} \alpha_I(\boldsymbol{\chi}) \boldsymbol{M}_I \otimes \boldsymbol{M}_I + \sum_{\substack{J,K=1 \\ J\neq K}}^{3} \beta_{JK}(\boldsymbol{\chi}) \boldsymbol{M}_J \otimes \boldsymbol{M}_K \\ &+ 2\mu(\mathbb{I} - \sum_{I=1}^{3} \boldsymbol{M}_I \otimes \boldsymbol{M}_I)\end{aligned} \tag{2.41}$$

with $\boldsymbol{E} = \frac{1}{2}(\boldsymbol{F}^{\mathsf{T}}\boldsymbol{F} - \mathbb{1})$, $\boldsymbol{M}_I = \boldsymbol{e}_I \otimes \boldsymbol{e}_I$, $\beta_{JK} = \beta_{KJ}$, and $\mathbb{I}_{ijkl} = \frac{1}{2}(\delta_{ik}\delta_{jl} + \delta_{il}\delta_{jk})$. Let $\alpha_I(\boldsymbol{\chi}) = \alpha\Lambda_I(\boldsymbol{\chi})$, where $\Lambda_I = \sqrt{\sum_{i=1}^{3} \chi_{iI}^2}$ is the distortion of the crystal structure in the $\boldsymbol{e}_I$ direction due to the configurational change. Also, let $\beta_{JK} = \beta$. Since $\partial\Lambda_I/\partial\boldsymbol{\chi} = \Lambda_I^{-1}\boldsymbol{\chi}\boldsymbol{M}_I$, this results in

$$\frac{\partial\psi^{\mathrm{S}}}{\partial\boldsymbol{\chi}} = \frac{1}{2}\sum_{I=1}^{3} \frac{\alpha}{\Lambda_I}\boldsymbol{\chi}\boldsymbol{M}_I M_{II}^2 \tag{2.42}$$

2.2.4.1 Anisotropy induced by a configurational change in crystal structure

Changes in the material configuration are considered that correspond to an evolution from a cubic crystal structure to three tetragonal crystal structures (in 3D), each oriented along one of the coordinate axes. The resulting anisotropy is reflected in the standard elastic deformation fields and the associated stresses. To demonstrate this effect, two unit cubes are considered, each initially with a cubic crystal structure. Through Dirichlet boundary conditions on the configurational domain, one cube is forced into a tetragonal crystal structure oriented along $\boldsymbol{e}_1$ and the other cube into an $\boldsymbol{e}_2$-oriented tetragonal structure. Both cubes are also subjected to simple uniaxial tension along $\boldsymbol{e}_1$ through applied Dirichlet conditions on the standard displacement.

The distinct stress plots of Figure 2.10 show the resulting anisotropy. The three well free energy function was used for ψ^{M} and $\alpha_I(\boldsymbol{\chi}) = \alpha(5\Lambda_I(\boldsymbol{\chi}) - 4)$ to accentuate the anisotropy. The anisotropic tetragonal crystal structures in the two cases also produce distinct lateral deformation. Figure 2.11 compares the two computations, and the second case shows significantly less displacement in the $\boldsymbol{e}_2$ direction due to the $\boldsymbol{e}_2$-oriented tetragonal structure.

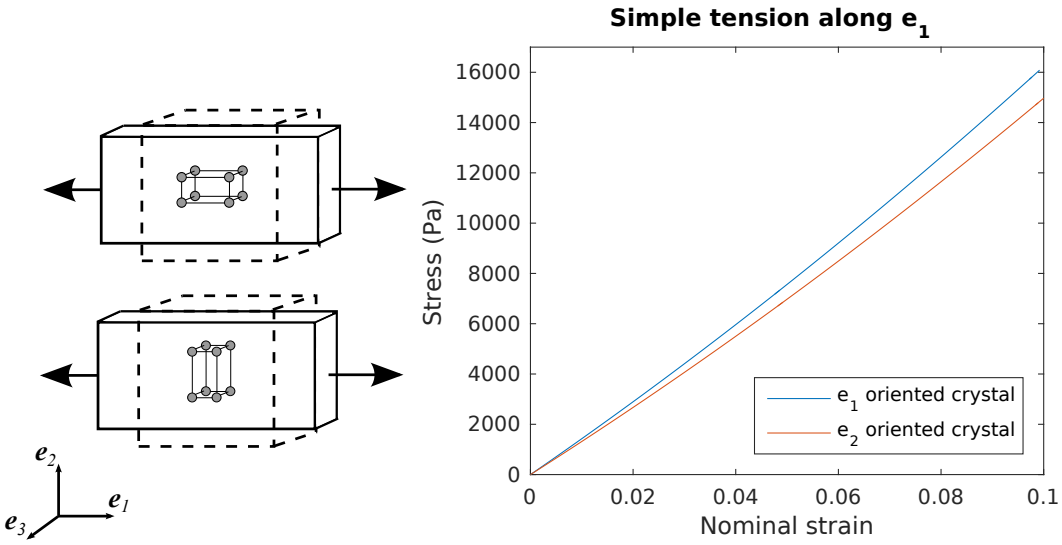

Figure 2.10: The $\boldsymbol{e}_1$-oriented tetragonal crystal structure leads to higher stresses than the $\boldsymbol{e}_2$-oriented tetragonal structure when subjected to simple uniaxial tension along $\boldsymbol{e}_1$. This demonstrates the differences in evolved anisotropy induced by the configurational changes in the two cases depicted on the left.

2.2.5 Microstructure formation by evolution of the material configuration

Figure 2.12 demonstrates a 2D plane strain problem wherein the material configuration evolves to distort the crystal structure from the the square to the rectangle. The beam is rapidly quenched from a high temperature causing the initially stable square structure to become unstable as the configuration-dependent component of the free energy function, ψ^{M}, changes from convex to double-welled. The beam is then loaded in bending. The double-welled free energy renders the rectangular variants stable, and strain accommodation of the inhomogeneous configuration results in

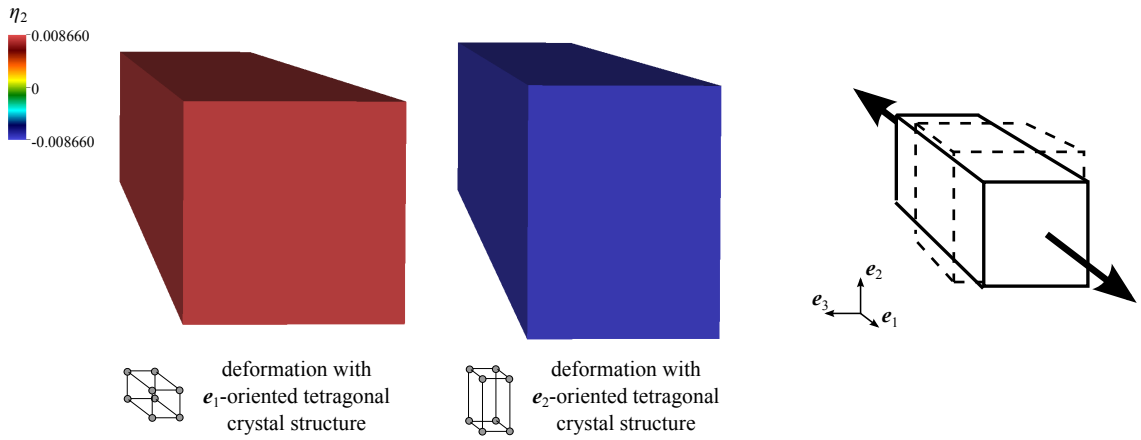

Figure 2.11: Computational results are compared for simple uniaxial tension along $\boldsymbol{e}_1$. The color contour plots of η_2 display the tetragonal variants, whose corresponding wells are located at $(\sqrt{3}/200, 1/200)$, $(-\sqrt{3}/200, 1/200)$, and $(0, -0.01)$ in (η_2, η_3) space. The distortion has been scaled by $20\times$ the elastic deformation. The results on the right show less deformation in the $\boldsymbol{e}_2$ direction due to the anisotropy induced by the $\boldsymbol{e}_2$-oriented tetragonal crystal structure, compared to the case on the left.

the microstructure shown. The parameter values used in equations 2.37 and 2.40 are $s = 0.1$, $d = 1$, $l = 0.1$ and $\mu = 1 \times 10^{-1}$, $\beta = 1 \times 10^{-1}$, $\alpha = 2 \times 10^{-1}$, respectively. Contours of η_2 appear in the plots, where $\eta_2 = \pm 0.1$ locates the wells corresponding to the two rectangular variants, and $\eta_2 = 0$ is the square structure, which exists only in the interfaces between variants in this evolved material configuration. The fineness of the microstructure in the computations is determined by the gradient length scale parameter l. The configurational displacement $\boldsymbol{U}$ at $x_1 = 10$ was specified as $0.5\bar{\boldsymbol{u}}$.

Figure 2.13 demonstrates the corresponding problem in 3D, where "plane strain boundary conditions" have been applied on the faces perpendicular to $\boldsymbol{e}_3$. The strain energy density function ψ^{M} allows for three tetragonal variants, but only two variants are seen due to the plane strain boundary conditions. The parameter values used in equations 2.37 and 2.40 are $s = 0.1$, $d = 1$, $l = 0.25$ and $\mu = 1 \times 10^{-1}$, $\beta = 1 \times 10^{-1}$, $\alpha = 2 \times 10^{-1}$, respectively. Contours of η_2 appear in the plots, where the three tetragonal variants are located at $(\sqrt{3}/20, 1/20)$, $(-\sqrt{3}/20, 1/20)$, and $(0, -0.1)$ in (η_2, η_3) space. Again, the configurational displacement $\boldsymbol{U}$ at $x_1 = 10$ was specified as

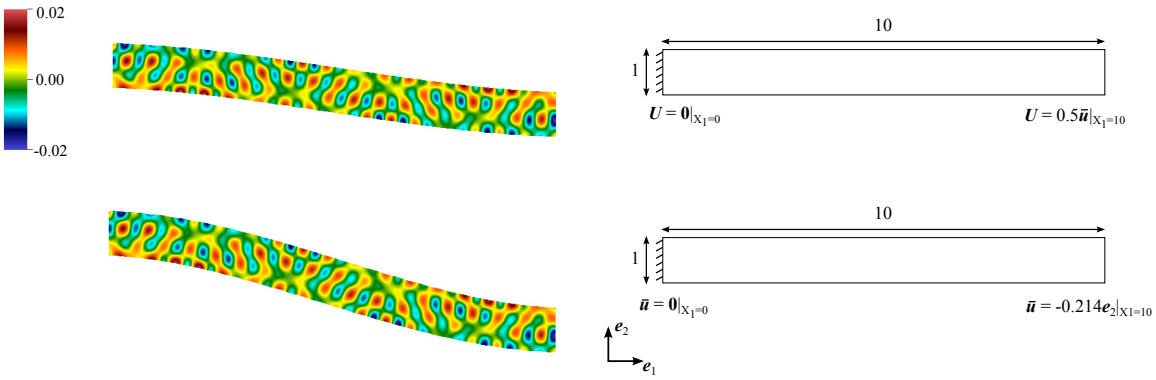

Figure 2.12: Simulation of 2D beam bending and the resulting material microstructure. The configurational displacement $\boldsymbol{U}$ was specified to be $0.5\bar{\boldsymbol{u}}$ at $X_2 = 10$. Contours of η_2 are plotted where the values ± 0.1 locate the well corresponding to the two rectangular variants. The top plot is deformed by the configurational displacement and the bottom plot by the total displacement. The displacement for both plots is scaled by a factor of $10\times$.

$0.5\bar{\boldsymbol{u}}$. Note that a larger length scale parameter was used in the 3D problem, resulting in a coarser microstructure than the 2D bending problem.

The results of these computations compare well with those obtained by [85]. However, in that work no configurational fields were identified. The entire problem was posed as a problem of elasticity relative to a high-symmetry (cubic or square) reference crystal. For a state where in the high-symmetry structure became unstable (by quenching, for instance) elastic deformation carried in the crystal structure into stable tetragonal states. The merits of the treatment presented here are that they allow us to separate out the configurational evolution as distinct from elastic deformation. This is particularly useful in describing anisotropy, as shown in Section 2.2.4.1.

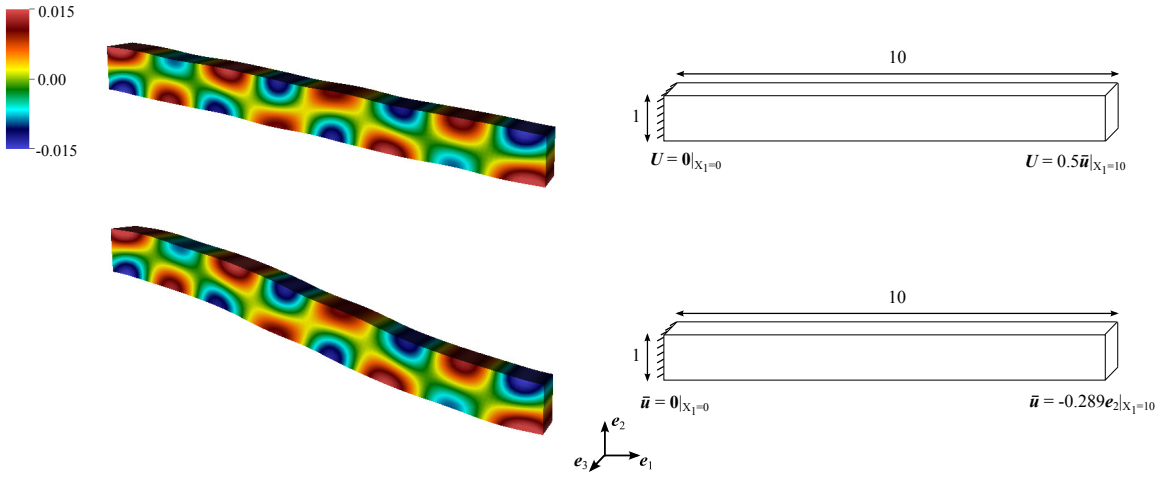

Figure 2.13: Simulation of 3D beam bending with plane strain boundary conditions and the resulting material microstructure. Contours of η_2 are plotted where the values ± 0.0866 correspond to two of the three tetragonal variants. Only two variants are seen because of the plane strain boundary conditions. The top plot is deformed by the configurational displacement and the bottom plot by the total displacement. The displacement for both plots is scaled by a factor of $10\times$. A larger length scale parameter was used in the 3D problem than the 2D, resulting in a coarser microstructure.

2.3 Concluding remarks

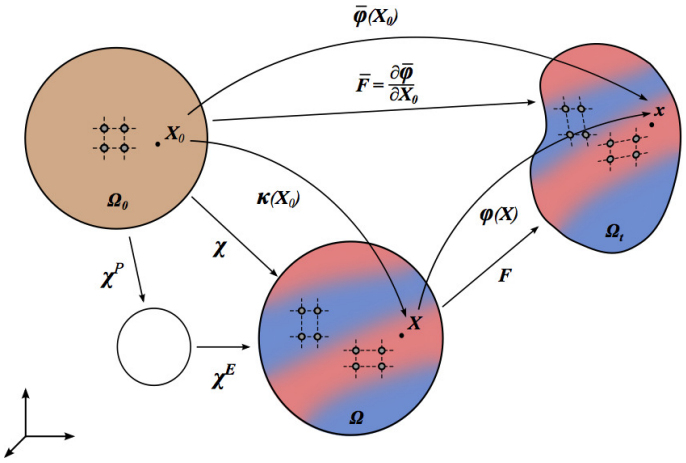

This chapter has considered the modeling of materials with multiple solid phases within a continuum setting by separating the kinematics associated with the material evolution into a newly-identified configurational field, and the standard displacement field. This applies to interfacial phases changes maintaining a sharp interface and to volume phase changes resulting in multiple diffuse interfaces. By noting that the

free energy density can be extended to depend on both these kinematic fields, equilibrium conditions associated with the configurational evolution have been obtained, separately from those that hold for the standard displacement field.

This separation of the deformation field into a configurational field in the material space and a standard spatial displacement field allows this framework to model a wide class of materials physics problems involving formation and movement of phase boundaries. In the context of crystalline materials, phase boundaries may occur due to nucleation and growth mechanisms, like those seen during precipitate evolution and formation of grain boundaries, or through phase transformations like martensitic transformations and twin-formation in HCP metals. All these phenomena involve sharp or diffused phase boundaries driven by interface kinetics or volumetric phase transformations. The framework presented here provides an overarching theoretical basis for representing the evolution of both sharp and diffuse phase boundaries. Notably, it also furnishes a variational basis for obtaining the governing partial differential equations.

This chapter has presented a preliminary exploration of phase transformations restricted to migrating sharp interfaces, such as arise at incoherent interphases, as well as phase transformations that occur throughout the volume of a material, resulting in diffuse interphase interfaces. It has been shown that evolving elastic anisotropy due to the phase changes that distort the crystal structure from a parent to a daughter phase can be captured through a dependence of the free energy density function and of the conventional elastic moduli on the tangent map of the configurational field. Additionally, this formulation is able to reproduce the results previously obtained with a treatment of all deformation relative to a high symmetry reference crystal.

Irreversibilities of crystallographic slip associated with the material evolution can be represented by imposing a further elasto-plastic decomposition on the tangent map of the configurational field $\boldsymbol{\chi} = \boldsymbol{\chi}^{\mathrm{E}}\boldsymbol{\chi}^{\mathrm{P}}$, where $\boldsymbol{\chi}^{\mathrm{E}}$ models the elastic distortion of the

crystal structure and $\boldsymbol{\chi}^{\mathrm{P}}$ models the crystallographic slip. Additionally, the common kinematic and variational underpinnings to the treatment of sharp and diffuse interfaces suggests the potential for modeling the evolution within a material from coherent (diffuse) to incoherent (sharp) interphase interfaces. The treatment introduced in this communication therefore has potential for modeling a wide array of phase transformations while clearly exposing the underlying configurational changes. That these configurational fields can be as diverse as that corresponding to interface motion in a non-crystalline material as well as crystal distortion is notable.

CHAPTER III

Phase-field description of voiding during oxidation and an application of evolving configurations

Void formation has been widely observed during the surface oxidation of some metals [90, 26, 91, 27, 92, 93, 94]. Excess voiding along the interface can lead to delamination of the oxide layer. There are multiple possible mechanisms driving the voiding process, including vacancy condensation and the effect of oxide stresses [26, 91, 27, 92, 94]. Vacancy condensation describes the creation of vacancies due to selective fast transport of the metal and their subsequent coalescence. The growth and expansion of the oxide on the surface can also create tensile stresses in the metal or within various suboxides, which can further create or expand voids.

The oxidation process can be modeled with phase-field methods using the Cahn-Hilliard equation [52], although this method represents all interfaces as diffuse. This method depends on a free energy surface, with local minima representing stable material phases. Voiding can be incorporated by introducing a well in the free energy surface at low concentrations of oxygen and metal, representing a low energy state achieved by the coalescence of vacancies. The example case taken here is the oxidation of titanium, although the method can be applied to other metals. An additional description and example of the Cahn-Hilliard equation in oxygen diffusion is found in Chapter IV.

The effect of oxide stresses can be incorporated by including finite-strain solid mechanics, with deformations due the change in the crystal structure and elasticity. This is presented as an application and extension of the method presented in Chapter II.

3.1 Vacancy condensation and phase-field

Phase-field models based on the Cahn-Hilliard equation are well-suited to modeling the physics of diffusion and the formation of distinct phases with coherent interfaces. As such, the Cahn-Hilliard description cannot capture the influence of sharp, incoherent interfaces that arise in oxidation. It may, however, be sufficient to explore the role of vacancy condensation in void formation.

The initial model neglects any oxide expansion or effects of mechanics and focuses on the mechanism of vacancies coalescing to form voids as the titanium diffuses out to the surface. The proposed method models the concentrations of oxygen and titanium as scalar fields, considering vacancies to exist where the concentration of titanium is less than one. Thus, a free energy surface was constructed as a function of concentration of titanium, c_{Ti}, and concentration of oxygen, c_{O}, both relative to some reference titanium crystal (see Figure 3.1). The surface has three wells: pure Ti ($c_{\mathrm{Ti}} = 1$, $c_{\mathrm{O}} = 0$), titanium dioxide ($c_{\mathrm{Ti}} = 1$, $c_{\mathrm{O}} = 2$), and void ($c_{\mathrm{Ti}} = 0.1$, $c_{\mathrm{O}} = 0.2$). The oxide well is significantly deeper than the other two wells to induce oxide growth. This free energy density function is given by the following:

$$\begin{aligned} f(c_{\mathrm{Ti}}, c_{\mathrm{O}}) = &\left[(c_{\mathrm{Ti}} - 1)^2 + c_{\mathrm{O}}^2\right]\left[(c_{\mathrm{Ti}} - 1)^2 + (c_{\mathrm{O}} - 2)^2\right] \\ &\times \left[(c_{\mathrm{Ti}} - 0.1)^2 + (c_{\mathrm{O}} - 0.2)^2\right] - 0.1 c_{\mathrm{O}} \end{aligned} \tag{3.1}$$

Introducing isotropic gradient energy terms as well gives the following Gibbs free

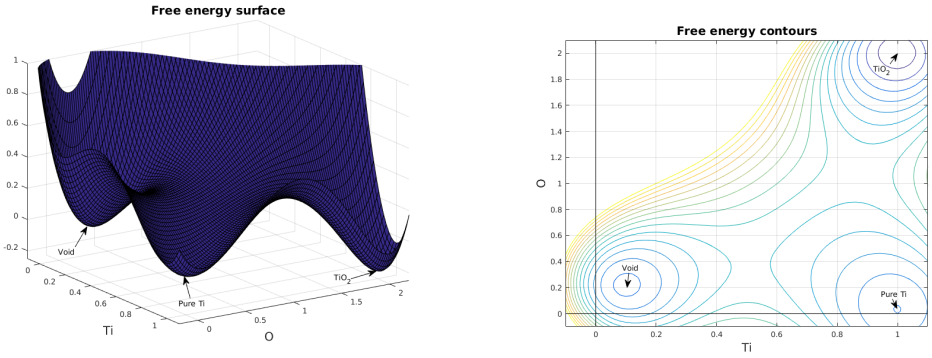

Figure 3.1: The three-well free energy surface and contour plot for titanium, oxide, and void.

energy functional:

$$\Pi[c_{\mathrm{Ti}}, c_{\mathrm{O}}] = \int_{\Omega} \left[f(c_{\mathrm{Ti}}, c_{\mathrm{O}}) + \frac{\kappa}{2} \left(\nabla c_{\mathrm{Ti}} \cdot \nabla c_{\mathrm{Ti}} + \nabla c_{\mathrm{O}} \cdot \nabla c_{\mathrm{O}} \right) \right] \mathrm{d}V \tag{3.2}$$

The chemical potentials of oxygen, μ_{O}, and titanium, μ_{Ti}, are equal to the variational derivative of the Gibbs free energy with respect to their concentrations, where X can be replaced by O or Ti:

$$\mu_X = \frac{\partial f}{\partial c_X} - \kappa \nabla^2 c_X \tag{3.3}$$

The flux for each species written in terms of the gradient of the chemical potential and combined with the conservation law. The resulting Cahn-Hilliard equation can then be written in strong form:

$$\frac{\partial c_X}{\partial t} = -\nabla \cdot (-M_X \nabla \mu_X) \tag{3.4}$$

Eq. (3.3) can be substituted into Eq. (3.4), resulting in a PDE that is fourth-order in space. Alternatively, it can be solved using a mixed method, in which the chemical potential is also considered a variable field. This consists of simultaneously solving two equations (Eqs. (3.3) and (3.4)) that are each second-order PDEs.

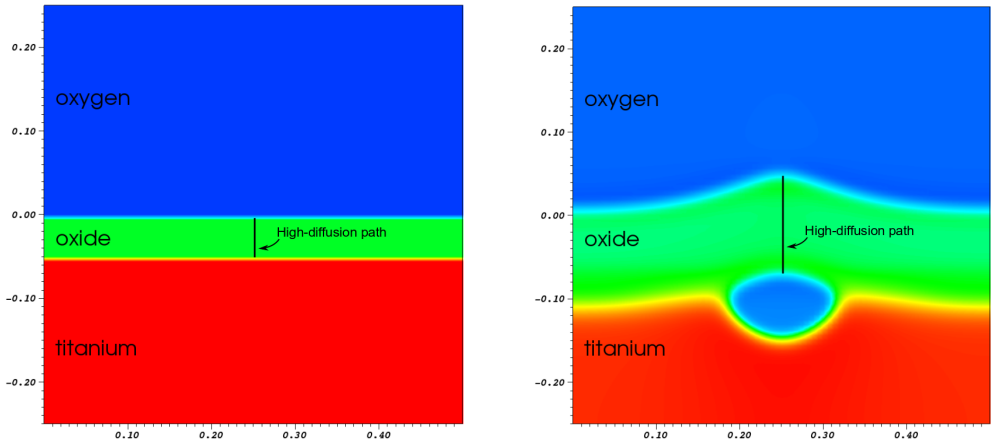

(a): Initial condition (b): Void formation

Figure 3.2: The diffusion of titanium out through the grain boundary causes a void to form.

The corresponding weak form of the equations is used to simultaneously solve the four equations (with $X = \mathrm{O}$ and $X = \mathrm{Ti}$) using the finite element method:

$$\int_\Omega \left(w \frac{\partial c_X}{\partial t} + \nabla w \cdot (M_X \nabla \mu_X) \right) \mathrm{d}V = \int_{\partial\Omega} \boldsymbol{J} \cdot \boldsymbol{N} \, \mathrm{d}S \tag{3.5}$$

$$\int_\Omega \left(w \left(\mu_X - \frac{\partial f}{\partial c_X} \right) + \nabla w \cdot (\kappa \nabla c_X) \right) \mathrm{d}V = 0 \tag{3.6}$$

assuming $\nabla c_X \cdot \boldsymbol{N} = 0$ on the boundary.

The phase-field model is given an initial field with regions representing gaseous oxygen, oxide, and titanium (see Figure 3.2). A vertical, high diffusion path for titanium through the oxide at $x = 0.25$ represents a grain boundary. In the model, as the titanium diffuses rapidly out to oxidize at the surface, a void forms where the grain boundary meets the titanium.

3.2 Mechanics and evolving configurations

The mechanics can be introduced in a setting similar to Chapter II, with multiple configurations representing different aspects of the deformation. Some intermediate

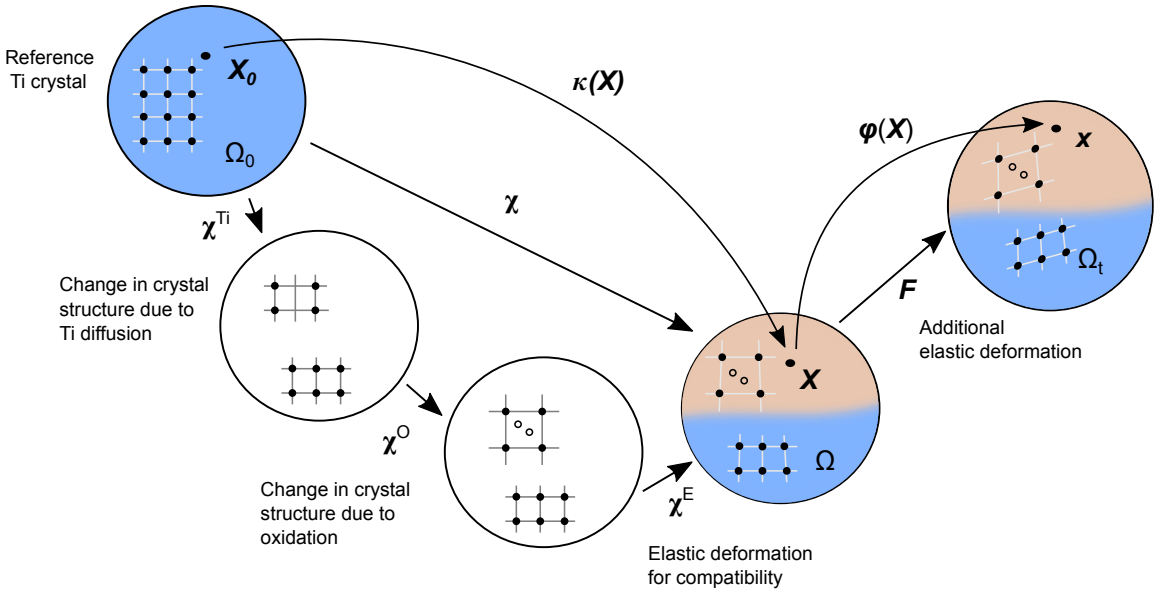

Figure 3.3: Schematic of the kinematics and configurations associated with oxidation. The white configurations represent the purely mathematical decomposition of the deformation into parts representing contraction or expansion due to titanium and oxygen diffusion.

configurations, however, may be incompatible, without a continuous mapping between the two. In these cases, a second displacement field is not applicable, and the deformation gradient can be defined using other means, such as a dependence on the composition. As an example, the treatment shown here includes both incompatible and compatible configurations.

The lattice parameters of a metallic oxide can be much larger than those of the metal itself. For example, the Pilling-Bedworth ratio (the ratio of the volume of the oxide to the volume of the corresponding metal) has been reported as 1.95 for TiO_2 [95]. This expansion due to oxidation can be represented by the tensor $\boldsymbol{F}^{\mathrm{O}}$. This model also considers the diffusion of titanium atoms and the resulting vacancies. The outdiffusion of titanium from a region could cause a contraction relative to some base titanium crystal, represented by $\boldsymbol{F}^{\mathrm{Ti}}$. These deformation tensors, on their own, may be incompatible, and a third deformation gradient, $\boldsymbol{F}^{\mathrm{E}}$, representing elasticity should be introduced to maintain a continuous crystal with no discontinuities. Then the

total deformation gradient is modeled as $\boldsymbol{F} = \boldsymbol{F}^{\mathrm{E}}\boldsymbol{F}^{\mathrm{O}}\boldsymbol{F}^{\mathrm{Ti}}$. The elastic deformation could be divided into two compatible parts: the first representing only the elasticity required by the change in crystal structure, and the second to model any additional elastic deformation caused by boundary conditions. This would be most useful if different strain energy density functions applied in the two cases. Using notation introduced previously, the deformation due to change in crystal structure would be $\boldsymbol{\chi} := \boldsymbol{\chi}^{\mathrm{E}}\boldsymbol{\chi}^{\mathrm{O}}\boldsymbol{\chi}^{\mathrm{Ti}}$ and the additional, standard deformation would be represented by $\boldsymbol{F}$. The associated configurations are shown in Figure 3.3. It is important to note that, although the arrows in the figure suggest a sequence in the configurations, this is purely a mathematical decomposition representing different aspects of the physics. All configurations, other than the reference configuration, are updated simultaneously at each time step.

The free energy functional, including gradient terms required by the phase field model, is as follows:

$$\begin{aligned}\Pi[\bar{\boldsymbol{u}}; \boldsymbol{u}; c_{\mathrm{Ti}}; c_{\mathrm{O}}] = &\int_{\Omega_0} \left[\psi^{\mathrm{M}}(\boldsymbol{X}^0, \boldsymbol{\chi}^{\mathrm{E}}, c_{\mathrm{Ti}}, c_{\mathrm{O}}) + \psi^{\mathrm{S}}(\boldsymbol{X}, \boldsymbol{F}, c_{\mathrm{Ti}}, c_{\mathrm{O}}) \det \boldsymbol{\chi}\right] \mathrm{d}V_0 \\ &+ \int_{\Omega_0} \left[f(c_{\mathrm{Ti}}, c_{\mathrm{O}}) + \frac{\kappa}{2}\left(\nabla c_{\mathrm{Ti}} \cdot \nabla c_{\mathrm{Ti}} + \nabla c_{\mathrm{O}} \cdot \nabla c_{\mathrm{O}}\right)\right] \mathrm{d}V_0 \\ &- \int_{\Omega_0} \boldsymbol{f}^0 \cdot \bar{\boldsymbol{u}} \, \mathrm{d}V_0 - \int_{\partial\Omega^{\mathrm{S}}_{T_0}} \boldsymbol{T}^0 \cdot \bar{\boldsymbol{u}} \, \mathrm{d}S_0\end{aligned} \tag{3.7}$$

where ψ^{M} is the strain energy due to change in crystal structure, ψ^{S} is the strain energy due to standard elastic deformation, and f is the chemical free energy.

The resulting strong form is

$$(\det \boldsymbol{\chi})\, \boldsymbol{P}^{\mathrm{S}} \boldsymbol{\chi}^{-\mathsf{T}} \boldsymbol{N}^0 - \boldsymbol{T}^0 = 0 \text{ on } \partial\Omega^{\mathrm{S}}_{T_0} \tag{3.8a}$$

$$\operatorname{Div}\left(\det\boldsymbol{\chi}\boldsymbol{P}^{\mathrm{S}}\boldsymbol{\chi}^{-\mathsf{T}}\right)+\boldsymbol{f}^{0}=0 \text{ in } \Omega_0 \tag{3.8b}$$

$$\left(\boldsymbol{P}^{\mathrm{M}}\left(\boldsymbol{\chi}^{\mathrm{O}}\boldsymbol{\chi}^{\mathrm{Ti}}\right)^{-\mathsf{T}}+\boldsymbol{\mathcal{E}}\boldsymbol{\chi}^{-\mathsf{T}}\right)\boldsymbol{N}^{0}=0 \text{ on } \partial\Omega^{\mathrm{M}}_{T_0} \tag{3.8c}$$

$$\operatorname{Div}\left(\det\boldsymbol{\chi}\left(\boldsymbol{P}^{\mathrm{M}}\left(\boldsymbol{\chi}^{\mathrm{O}}\boldsymbol{\chi}^{\mathrm{Ti}}\right)^{-\mathsf{T}}+\boldsymbol{\mathcal{E}}\boldsymbol{\chi}^{-\mathsf{T}}\right)\right)-\det\boldsymbol{\chi}\frac{\partial\psi^{\mathrm{S}}}{\partial\boldsymbol{X}}=0 \text{ in } \Omega_0 \tag{3.8d}$$

The chemical potentials μ^{Ti} and μ^{O}, used in the Cahn-Hilliard equation, are found from their respective variational derivatives of the free energy. If the forms taken are $\boldsymbol{\chi}^{\mathrm{Ti}}=\lambda^{\mathrm{Ti}}(c_{\mathrm{Ti}})\mathbb{1}$ and $\boldsymbol{\chi}^{\mathrm{O}}=\lambda^{\mathrm{O}}(c_{\mathrm{Ti}},c_{\mathrm{O}})\mathbb{1}$, the expressions for the chemical potentials become:

$$\begin{aligned}\mu^{\mathrm{Ti}}=&-\boldsymbol{P}^{\mathrm{M}}:\left(\boldsymbol{\chi}^{\mathrm{E}}\left(\lambda^{\mathrm{Ti}}{}_{,c_{\mathrm{Ti}}}\lambda^{\mathrm{O}}+\lambda^{\mathrm{O}}_{,c_{\mathrm{Ti}}}\lambda^{\mathrm{Ti}}\right)\left(\lambda^{\mathrm{O}}\lambda^{\mathrm{Ti}}\right)^{-1}\right)\\&+\psi^{\mathrm{M}}_{,c_{\mathrm{Ti}}}+\psi^{\mathrm{S}}_{,c_{\mathrm{Ti}}}\det\boldsymbol{\chi}+f_{,c_{\mathrm{Ti}}}-\kappa\nabla^{2}c_{\mathrm{Ti}}\end{aligned} \tag{3.9a}$$

$$\mu^{\mathrm{O}}=-\boldsymbol{P}^{\mathrm{M}}:\left(\lambda^{\mathrm{O}}_{,c_{\mathrm{O}}}\boldsymbol{\chi}^{\mathrm{E}}(\lambda^{\mathrm{O}})^{-1}\right)+\psi^{\mathrm{M}}_{,c_{\mathrm{O}}}+\psi^{\mathrm{S}}_{,c_{\mathrm{O}}}\det\boldsymbol{\chi}+f_{,c_{\mathrm{O}}}-\kappa\nabla^{2}c_{\mathrm{O}} \tag{3.9b}$$

These expressions for the chemical potentials, along with the Cahn-Hilliard equation and mechanics equations of equilibrium form a model of the effect of vacancy condensation and oxide stresses on void formation.

3.3 Alternate description for including mechanics

An alternate method can be used to include the mechanics in the oxidation problem that more closely follows the description of Section 2.2 (see Figure 3.4). This can be done by combining the free energy density function described in Section 3.1 with a dependence on the deformation gradient $\boldsymbol{\chi}$ corresponding to changes in the crystal structure.

For the same stoichiometric composition, multiple crystal structures can occur in titanium oxide. Although rutile TiO_2 is the most common, anatase and brookite TiO_2 crystal structures can also form, where rutile and anatase are both tetragonal and

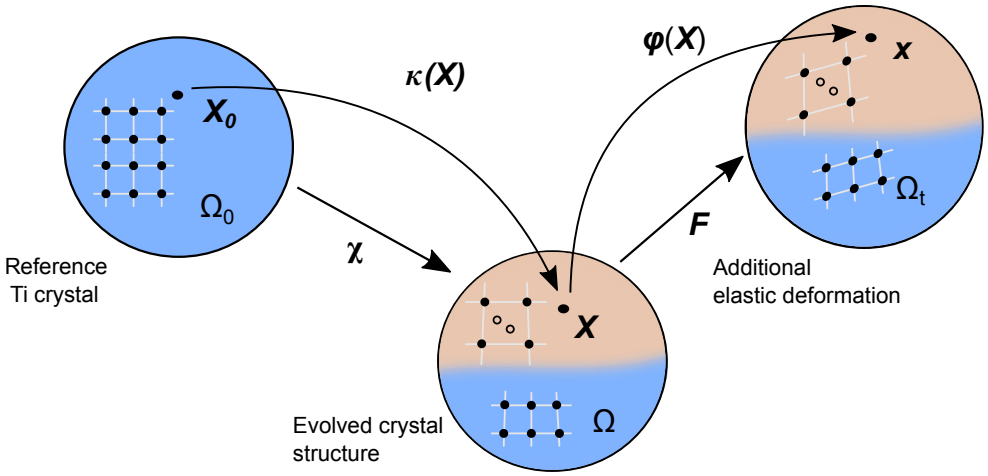

Figure 3.4: Schematic of the kinematics and configurations associated with oxidation.

brookite is orthorhombic [96]. These and other expansions and distortions compared to the based Ti crystal can be incorporated in the free energy density function f. Pure Ti can be represented in f by a minimum at $c_{\mathrm{Ti}} = 1$, $c_{\mathrm{O}} = 0$, and $\boldsymbol{\eta} = 0$, where $\boldsymbol{\eta}$ corresponds to the reparametrized strain space from Section 2.2.4. The well for void corresponds to a contraction of the crystal structure. The single well at titanium dioxide ($c_{\mathrm{Ti}} = 1$, $c_{\mathrm{O}} = 2$) in Eq. (3.1) is expanded into multiple energy wells corresponding to the crystal structures of rutile, anatase and brookite. Although each of these phases form at the same stoichiometry, given by c_{Ti} and c_{O}, there is a further strain instability causing the phases to decompose into three equivalent tetragonals for rutile and anatase and six equivalent orthorhombics for brookite. Each of these structures can be represented by a well in the free energy landscape. Additional suboxides can also be included.

The free energy functional, including gradient terms required for regularization and the phase-field model, then becomes:

$$\begin{aligned}\Pi[\bar{\boldsymbol{u}};\boldsymbol{u};c_{\mathrm{Ti}};c_{\mathrm{O}}] = &\int_{\Omega_0} \left[f(\boldsymbol{X}^0,\boldsymbol{\chi},\nabla^0\boldsymbol{\chi},c_{\mathrm{Ti}},c_{\mathrm{O}}) + \psi^{\mathrm{S}}(\boldsymbol{X},\boldsymbol{F},\boldsymbol{\chi})\det\boldsymbol{\chi}\right]\,\mathrm{d}V_0 \\ &+ \int_{\Omega_0} \frac{\kappa}{2}\left(\nabla c_{\mathrm{Ti}}\cdot\nabla c_{\mathrm{Ti}} + \nabla c_{\mathrm{O}}\cdot\nabla c_{\mathrm{O}}\right)\,\mathrm{d}V_0 \\ &- \int_{\Omega_0} \boldsymbol{f}^0\cdot\bar{\boldsymbol{u}}\,\mathrm{d}V_0 - \int_{\partial\Omega^{\mathrm{S}}_{T_0}} \boldsymbol{T}^0\cdot\bar{\boldsymbol{u}}\,\mathrm{d}S_0\end{aligned} \tag{3.10}$$

The resulting equilibrium conditions correspond to those in Section 2.2.3. The chemical potentials for titanium and oxygen can still be represented by Eq. (3.3), although the derivative $\partial f/\partial c_X$ will now have dependencies on the stress. Due to the strain gradient terms included for regularization, isogeometric analysis (IGA) would be a more appropriate solution approach than the mixed method used in Section 3.1.

3.4 Concluding remarks

The mechanisms behind the formation of voids in surface oxides potentially include vacancy condensation and the effect of oxide stresses. It is possible to represent the tendency of vacancies to coalesce into voids as a low energy state in the free energy landscape. A phase-field model using such an energy landscape, together with fast-diffusion paths representing oxide grain boundaries, did show the formation and growth of a void at the oxide-metal interface.

The equations representing the effects of oxide stress on the formation and evolution of voids were presented in the framework of evolving material configurations originally introduced in Chapter II. The description of configurations is used to define the total free energy. Variational methods then provide equilibrium conditions for the mechanics and the chemical potentials for the Cahn-Hilliard dynamics. These final equations provide a voiding model that incorporates both vacancy condensation and

oxide stresses.

CHAPTER IV

A comparison of Redlich-Kister polynomial and cubic spline representations of the chemical potential in phase field computations

Expressions for the free energy of a system, found by applying the appropriate Legendre transformation, "are regarded as fundamental equations because all thermodynamic properties of a substance can be evaluated" from them[1] [53]. The fundamental importance of the free energy has been seen in previous chapters. Their first derivatives define equilibrium conditions. Properties such as heat capacity, thermal expansivity, and compressibility are related to second derivatives. Additionally, regions of phase separation are captured by nonconvexities in the free energy [53]. The free energy often cannot, however, be measured directly. State variables associated with a derivative of the free energy, such as the chemical potential, can be measured or calculated then integrated to find the free energy [97]. For example, the chemical potential could be found using partial pressure measurements [98]. First-principles statistical mechanics methods can also be used to calculate free energies [40, 41, 42, 43, 45, 46, 47, 31].

[1] This chapter is based on the following paper: G. Teichert, H. Gunda, S. Rudraraju, A. Natarajan, B. Puchala, K. Garikipati, A. Van der Ven, 2017. A comparison of Redlich-Kister polynomial and cubic spline representations of the chemical potential in phase field computations, *Computational Materials Science* 128, 127–139.

Once free energy data is obtained, there is a need to represent it mathematically. Although the free energy density functions in previous chapters have been relatively simple, the free energy for actual materials may be much more complex, including rapid fluctuations in the free energy relative to changes in composition. A commonly used polynomial expansion is that introduced by Redlich and Kister [99]. While other polynomial expansions can also be used, "mathematically, the choice of basis (for a finite-dimensional space) makes no difference" according to Dahlquist and Björck [100]. It is known that sampling data at Chebyshev points significantly improves a polynomial *interpolation*, where the function passes through every data point. However, fitting to measured or calculated free energies generally involves many data points, making a least squares fit more appropriate than a polynomial interpolation. Chebyshev points are, therefore, not necessary [100]. Because of the mathematical equivalence of the various polynomial expansions (Redlich-Kister expansion, Legendre polynomial series, simple power series, etc.) [101, 102], the effectiveness of a polynomial expansion can be assessed by considering one basis set. Even so, Dahlquist and Björck point out that some functions are "not at all suited for approximation by one polynomial over the entire interval. One would get a much better result using approximation with piecewise polynomials" [100].

In this chapter, the use of the Redlich-Kister polynomials is compared with cubic splines (piecewise cubic polynomials with C^2 global continuity; i.e. continuous second derivatives) in fitting free energy data. This is done in the context of phase field modeling using the Cahn-Hilliard equation [103]. One physical phenomenon that this model captures is spinodal decomposition, where a material separates into two distinct phases. Spinodal decomposition arises when the free energy is concave with respect to composition resulting in a negative thermodynamic factor that causes uphill diffusion. Capturing this physics in a phase field model requires an accurate representation of the free energy and its higher order derivatives. It is shown here that there are cases

where even low-order splines are much more effective at representing the physics of the problem than are global polynomials, especially within the spinodal regions. Furthermore, the high polynomial degree sometimes required by the Redlich-Kister expansions significantly increases computation time.

4.1 Model system: oxygen dissolved in HCP Ti

Data for the Ti-O system was used to explore the effect of using different mathematical representations of the free energy. Dissolved oxygen fills octahedral interstitial sites in HCP Ti, creating TiO_x with stoichiometric compositions as high as $x = 1/2$ without significantly changing the crystal structure [25]. First-principles statistical mechanics methods can be used to predict the dependence of the free energy on composition. Results using these techniques have shown that within the range $0 < x \leq 1/2$ and at low temperatures, stable phases can occur at compositions of $x = 1/6$, $x = 1/3$, and $x = 1/2$ [104].

The oxygen chemical potential is equal to the derivative of the free energy according to

$$\mu = \left(\frac{\partial g}{\partial x} \right)_{T,P} \tag{4.1}$$

where g is the Gibbs free energy per Ti atom and x is the number of O atoms per Ti atom. The free energy can be determined from measured or calculated chemical potential data be integrating with respect to oxygen concentration x.

The chemical potential data obtained for use in this chapter was created using the CASM software package [45, 105, 46] and VASP plane-wave DFT code [106, 107]. Chemical potential data was calculated for both 1800 K and 800 K and integrated to find the free energy, as shown in Figure 4.1 [1]. The disordered solid solution is stable at 1800 K, resulting in a convex free energy curve. Multiple ordered suboxides are stable at 800 K, resulting a nonconvex free energy. Each ordered phase can

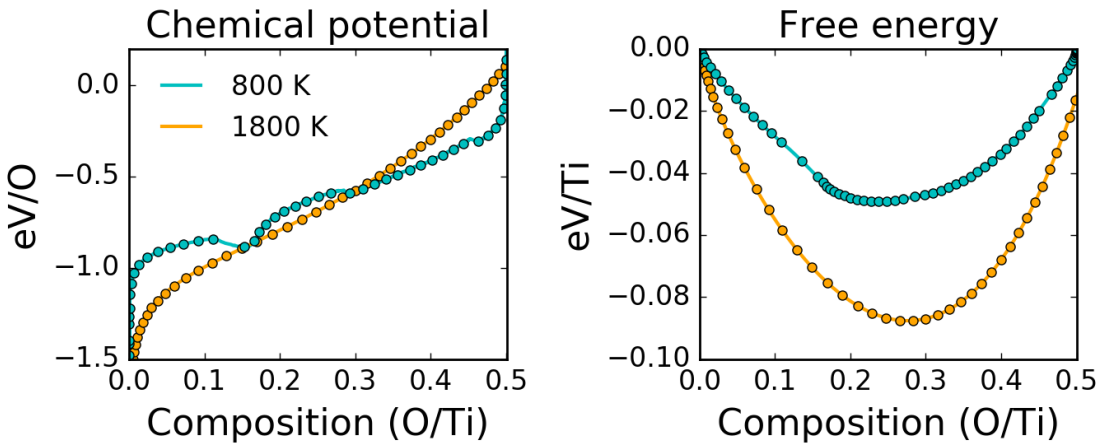

Figure 4.1: The calculated oxygen chemical potentials and free energies at 1800 K and 800 K used in this chapter [1].

be represented by an order parameter η_i, where eta_i is nonzero when its associated phase exists and zero otherwise. The free energy can then be written as a function of concentration and order parameters $g(x, \eta_1, \ldots, \eta_n)$. The free energies in Figure 4.1 can be considered as the curves that minimize $g(x, \eta_1, \ldots, \eta_n)$ with respect to η_i.

4.2 Different free energy representations

The ability of a truncated Redlich-Kister series and a spline fit to faithfully represent the free energies of TiO_x are compared. The high temperature free energy curve corresponding to a solid solution is considered first. The low temperature free energy poses more challenges due to the presence of several two-phase regions where the free energy is concave.

4.2.1 Methodology

The free energy is here expressed as

$$g(x) = k_B T \left[x \log(x) + (1 - x) \log(1 - x) \right] + \Delta g(x) \tag{4.2}$$

where the first term corresponds to an ideal solution entropy and $\Delta g(x)$ is an excess free energy representing a deviation from thermodynamic ideality. As usual k_B is Boltzmann's constant and natural logarithms are used. The inclusion of an ideal solution entropy term is especially useful in describing the free energy in the dilute limits (i.e. $x \to 0$ and $x \to 1$) where alloys behave as ideal solutions and where the excess free energy goes to zero. With the above free energy expression, the oxygen chemical potential in TiO_x then becomes

$$\mu(x) = k_B T \log\left(\frac{x}{1-x}\right) + \Delta\mu(x) \tag{4.3}$$

where $\Delta\mu(x)$ is the derivative with respect to x of $\Delta g(x)$. The ideal solution term captures the logarithmic divergences in the chemical potential μ in the dilute limits ($x \to 0$ and $x \to 1$).

The ability of a Redlich-Kister polynomial series and splines in fitting calculated values for the excess free energy Δg is compared below. Since the free energy is often found by first measuring or computing the chemical potential and then integrating, $\Delta\mu$ is fit to the difference between the chemical potential data and the logarithmic term $k_B T \log(x/(1-x))$.

4.2.1.1 Redlich-Kister polynomial series

Consider a R-K polynomial expansion for the function $\Delta g(x)$ of the following form:

$$\Delta g(x) = g_0 + g_1 x + x(1-x)\sum_{k=0}^{n} L_k (2x-1)^k \tag{4.4}$$

Then the function $\Delta\mu$ used in the curve fitting of the chemical potential has the form:

$$\Delta\mu = g_1 + \sum_{k=0}^{n} L_k[2kx(1-x) - (2x-1)^2](2x-1)^{k-1} \tag{4.5}$$

The coefficients L_k can be found by a least squares method.

The TiO_x chemical potential data for compositions from $x = 0$ to $x = 1/2$ was used. To avoid the noise where the data is steepest near $x = 0$ and $x = 1/2$, only data between 0.001 and 0.499 is used to fit the function.

4.2.1.2 Splines

A spline is a piecewise polynomial with a specified order of continuity at the subdomain junctions. The endpoints of each subdomain are called *knots* or *breaks*. Quoting verbatim from [100], a more formal definition is as follows:

Definition IV.1. A spline function $s(x)$ of order $k \geq 1$ (degree $k-1 \geq 0$), on a grid

$$\Delta = \{a = x_0 < x_1 < \cdots < x_m = b\}$$

of distinct knots is a real function s with the following properties:

(a) For $x \in [x_i, x_{i+1}]$,$i = 0 : m-1$, $s(x)$ is a polynomial of degree $< k$.

(b) For $k = 1$, $s(x)$ is a piecewise constant function. For $k \geq 2$, $s(x)$ and its first $k-2$ derivatives are continuous on $[a, b]$, i.e. $s(x) \in C^{k-2}[a, b]$

Note that the order of the spline is equal to the degree of the polynomial plus one. For example, cubic splines (order = 4) are piecewise cubic polynomials that are C^2 continuous across all knots (see Figure 4.2). Splines are able to capture local features due to the local nature of piecewise polynomials. The continuity conditions at the knots maintain a specified global continuity across the entire function. These local

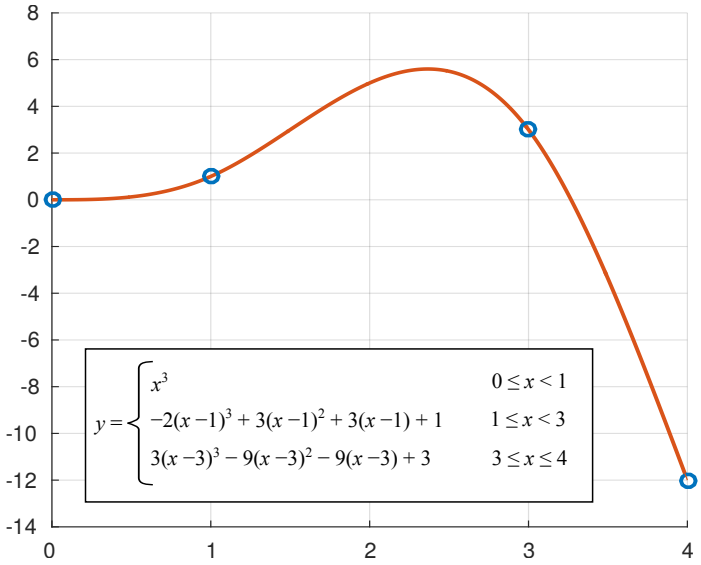

Figure 4.2: An example cubic spline, defined as a piecewise cubic polynomial over three subdomains. The function values at the four knots are $\{(0,0),(1,3),(3,3),(4,-12)\}$. Note that the first and second derivatives are continuous at the knots.

and global characteristics of splines make them an important and often ideal tool in function interpolation and fitting.

There are multiple ways of representing splines. The simplest form is as a standard piecewise polynomial, where a standard polynomial is given for each subdomain. There is nothing in this structure that guarantees that the function is, in fact, a spline; the polynomial coefficients must be chosen to ensure the necessary continuity across knots. Splines may also be written as a linear combination of *B-splines* (short for basis splines). A B-spline of order k at knot i will be denoted by $N_{i,k}$, and let τ_i be the location of knot i. Additional knots may be added at the endpoints, called *exterior knots*. The original set of knots will be called *interior knots*. The B-spline $N_{i,k}$ is strictly positive on the interval (τ_i, τ_{i+k}) and zero outside the interval. Given $m+1$ interior knots, B-splines have the summation property $\sum_i N_{i,k}(x) = 1$, for $x \in [\tau_0, \tau_m]$ [100]. B-splines can be represented using the following Cox-de Boor

recurrence relation [108]:

$$N_{i,k}(x) = \frac{x - \tau_i}{\tau_{i+k-1} - \tau_i} N_{i,k-1}(x) + \frac{\tau_{i+k} - x}{\tau_{i+k} - \tau_{i+1}} N_{i+1,k-1}(x) \tag{4.6}$$

$$N_{i,1}(x) = \begin{cases} 1 & \tau_i \leq x < \tau_{i+1} \\ 0 & \text{otherwise} \end{cases} \tag{4.7}$$

A spline function $s(x)$ of order k with $m+1$ interior knots can be represented as a linear combination of B-splines:

$$s(x) = \sum_{i=-k+1}^{m-1} c_i N_{i,k} \tag{4.8}$$

where c_i are the appropriate B-spline coefficients. The piecewise polynomial representation is

$$\begin{aligned} s(x) &= \sum_{i=0}^{m-1} P_{i,k} \\ P_{i,k} &= \begin{cases} \sum_{j=0}^{k-1} D_{i,j}(x - \tau_i)^{k-1-j} & \tau_i \leq x < \tau_{i+1} \\ 0 & \text{otherwise} \end{cases} \end{aligned} \tag{4.9}$$

where $\{D_{i,0}, \ldots, D_{i,k-1}\}$ are the coefficients for the polynomial in subdomain i.

In the case of spline interpolation, each given data point becomes a knot in the spline function. For n given data points, there are n knots and $n-1$ subdomains. For a spline of order k, there are k polynomial coefficients within each subdomain, for a total of $k(n-1)$ unknowns for the entire spline. The function value at each subdomain endpoint is specified, giving $2(n-1)$ constraints. This gives at least C^0 continuity across the function. Specifying continuity of order m at each subdomain junction adds $m(n-2)$ total constraints, for a total of $2(n-1) + m(n-2)$ constraints. Since the number of constraints must be less than or equal to the number of unknowns, then function interpolation using k^{th} order splines allows C^{k-2}. The interpolation

is performed by solving for the unknown with these constraints. This interpolation process can be done using splines written as a linear combination of B-splines or using the simple piecewise polynomial representation.

Where many data points are given, as in this study, it is useful to perform a spline fit instead of a spline interpolation. This allows fewer knots in the spline than data points, which can smooth out noise in the data and simplify the evaluation of the function. The curve fit can be done using a least square spline approximation. The B-spline representation of a spline allows us to express the least squares problem as follows:

$$\min_{\vec{\mathbf{c}}} \sum_{j=1}^{n} \left(\sum_{i=-k+1}^{m-1} c_i N_{i,k}(x_j) - f_j \right)^2 \tag{4.10}$$

where $\vec{\mathbf{c}}$ is the vector of coefficients, k is the B-spline order, $m+1$ is the number of interior knots, and (x_j, f_j) is the j^{th} data point [100].

Cubic splines are used to fit $\Delta\mu$ in the chemical potential function. A spline fit, as opposed to a spline interpolation, is used to smooth out the noise from the data and simplify the representation and evaluation of the function. The Octave `splinefit` function takes as input the data points and allows us to specify the location of the knots in the spline fit. It performs a least squares fit to the given data using B-splines. However, this function returns the spline's coefficients for the simple piecewise polynomial form shown in Eq. (4.9). This set of coefficients can then be evaluated for a given value of x in Octave using the `ppval` function or manually as standard piecewise polynomials.

To accurately capture local features of the data while minimizing the number of knots, regions where the data are changing rapidly are first identified. In the final spline fit, a higher density of knots are used in those regions. To do this, a cubic spline is first fit to the data with knots at relatively small intervals of 0.005 to approximate

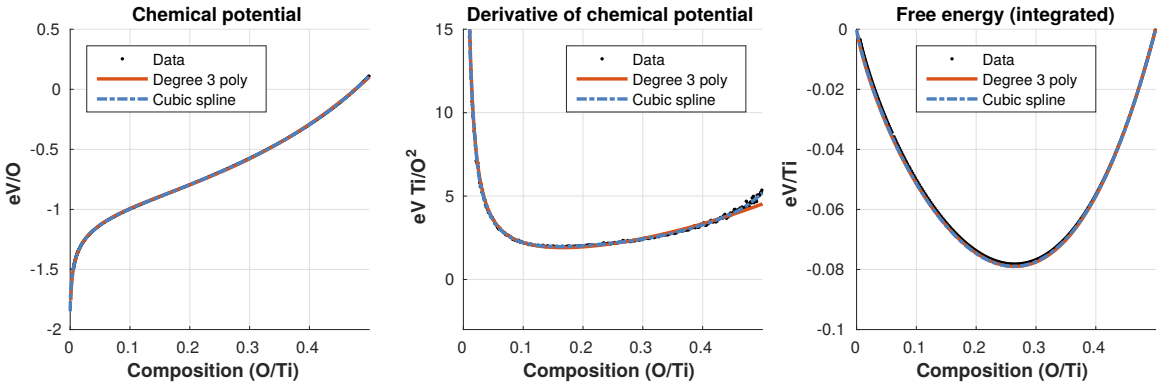

Figure 4.3: A degree three R-K polynomial provides a sufficient fit to the chemical potential for titanium oxide at 1800 K, as does a cubic spline.

$\Delta\mu$. This initial spline fit of $\Delta\mu$ is used to approximate $\Delta\mu''(x)$, and any region where $|\Delta\mu''(x)| > 600$ is identified as a region with rapidly changing data. For the final fit, knots are specified at intervals of 0.004 within the regions of rapidly changing data and at intervals of 0.03 outside those regions. This allows all the physics to be captured while reducing the number of knots. The function `splinefit` is used with this new set of knots to fit the data and update the spline representation of $\Delta\mu$.

4.2.2 Results

4.2.2.1 Data with no spinodal regions

At 1800 K, the titanium oxide system has a simple free energy landscape with no spinodals, and a degree three R-K polynomial expansion gives a sufficient fit of the chemical potential, as does the cubic spline. The chemical potential data and curve fit are shown in the left plot of Figure 4.3. The center plot shows the derivative of the chemical potential fit and the numerically differentiated data. This is also the second derivative of the free energy with respect to composition, which shows where the free energy curve is concave or convex. When the second derivative of the free energy is negative, the free energy is concave and represents a two-phase region. The numerical derivative was taken by first smoothing the data with a running average to

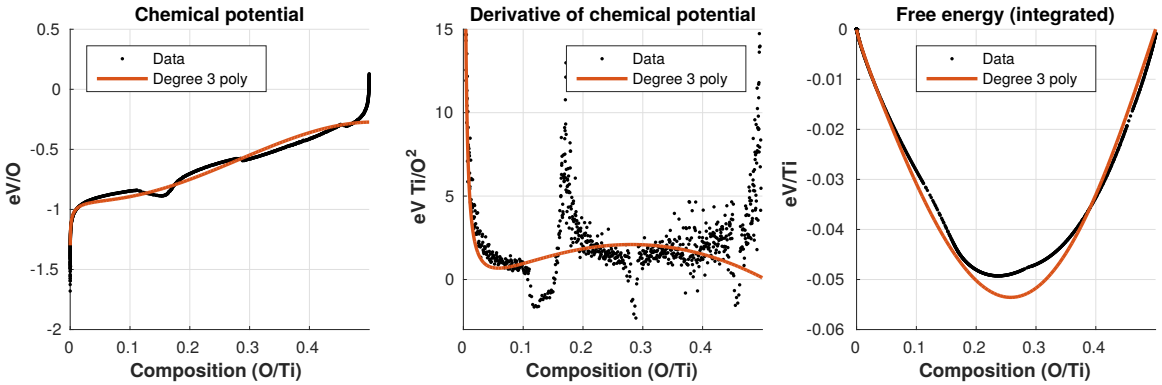

Figure 4.4: A degree three R-K polynomial with the term $\log(x/(1-x))$ fails to capture the divergent behavior in the chemical potential at $x = 1/2$ for titanium oxide at 800 K.

remove some of the noise, then performing a central difference derivative. The plot on the right shows the free energy found by integrating the curve fit and data. It is plotted with respect to the end members at $x = 0$ and $x = 1/2$. A cubic spline fit of the data is also presented. Note that the cubic spline, while it also fits the data well, does not give a significantly better representation of this set of data.

4.2.2.2 Data with three spinodal regions

At 800 K, the HCP form of TiO_x exhibits three spinodal regions. To accurately capture this physics, the function representing the free energy must have three corresponding concave regions. Fewer data points were calculated with the variance constrained Monte Carlo within these spinodal regions. They were weighted $10\times$ to help capture the spinodals with the polynomial function. The data are fitted with a degree three R-K polynomial as before. The data and fit are plotted in Figure 4.4 along with their corresponding derivatives and free energy. Note that the chemical potential data was smoothed before computing the numerical data to reduce the effects of noise. Also, as in all plots in this work, the free energies are plotted with respect to the end members at $x = 0$ and $x = 1/2$.

The data diverge due to an ordering at $x = 1/2$, but the equation used here does

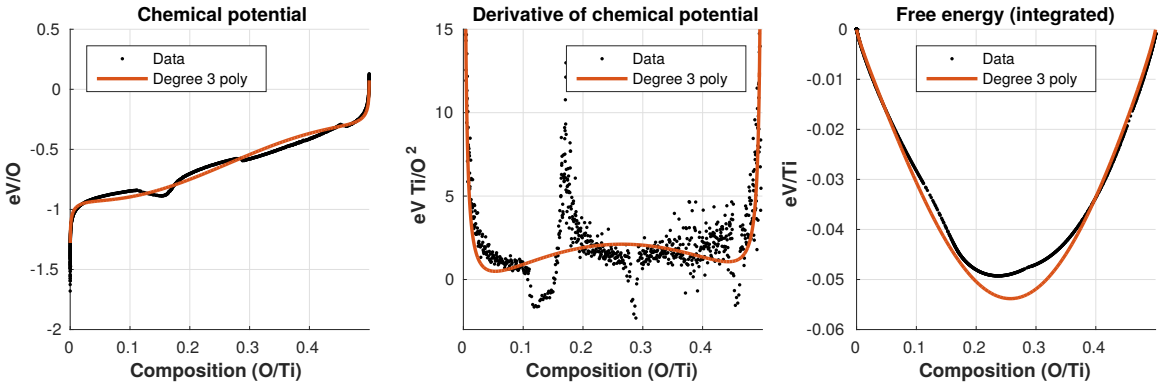

Figure 4.5: The term $\log(2x/(1-2x))$ is able to capture the divergent behavior in the chemical potential for titanium oxide at 800 K.

not capture this divergence. The divergent behavior of the system can be represented by scaling the logarithmic term. This gives us the modified form

$$\mu(x) = k_B T \log\left(\frac{2x}{1-2x}\right) + \Delta\mu(x) \tag{4.11}$$

to model the chemical potential curve over the domain $[0, 1/2]$. This corresponds to a free energy density of

$$g(x) = \tfrac{1}{2} k_B T \left[2x \log(2x) + (1-2x)\log(1-2x)\right] + \Delta g(x) \tag{4.12}$$

For consistency, the Redlich-Kister polynomial is also rescaled to the same domain of $[0, 1/2]$.

$\Delta\mu(x)$ is now fit to the difference between the chemical potential data and $k_B T \log(2x/(1-2x))$. The resulting fit is shown in Figure 4.5. Note that the divergence of the data at $x = 1/2$ is now represented in the curve fit. It is clear, however, that a degree three R-K polynomial cannot represent the spinodal regions. Polynomials of higher degree are used to fit the chemical potential and are plotted in Figure 4.6. The curve fit represents a spinodal region wherever the derivative of the chemical potential is negative, meaning the free energy is concave (see the center plots of Figure 4.6). Us-

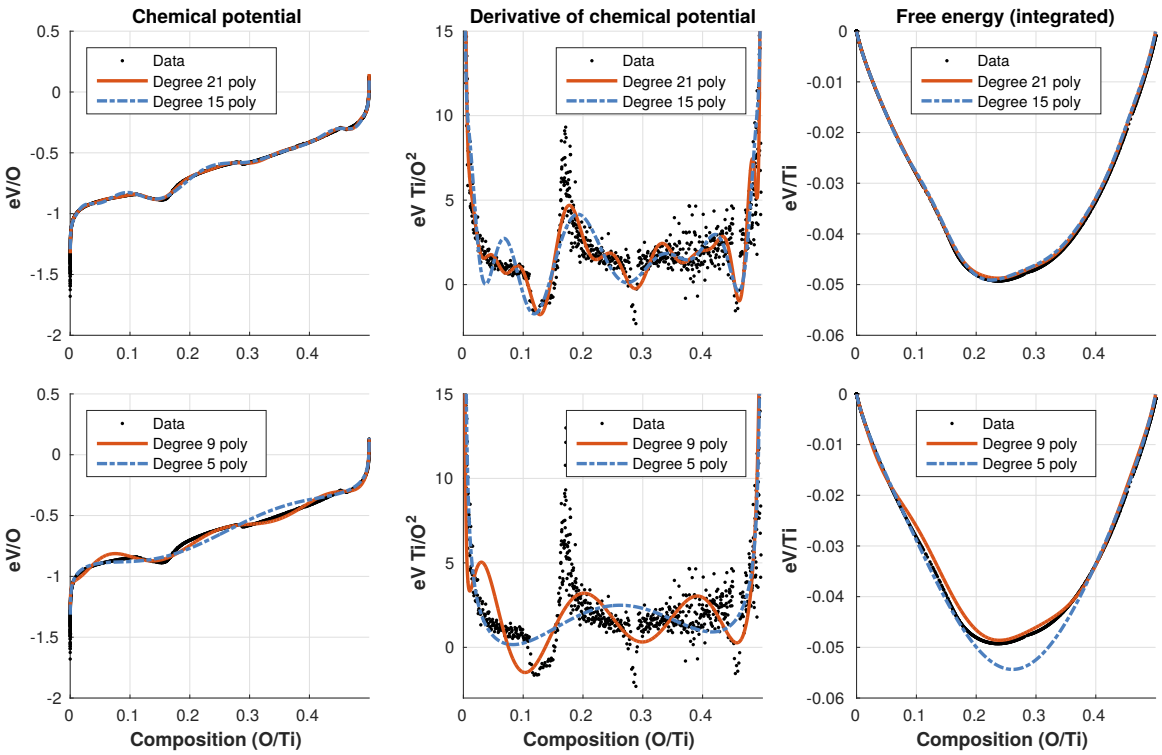

Figure 4.6: R-K polynomials of degree 5, 9, 15, and 21 are used to fit the chemical potential data. The corresponding numerical and analytical derivatives are plotted. The free energy is found from the chemical potential integral and is with respect to end members at $x = 0$ and $x = 1/2$. Only the degree 21 polynomial captures all three spinodals.

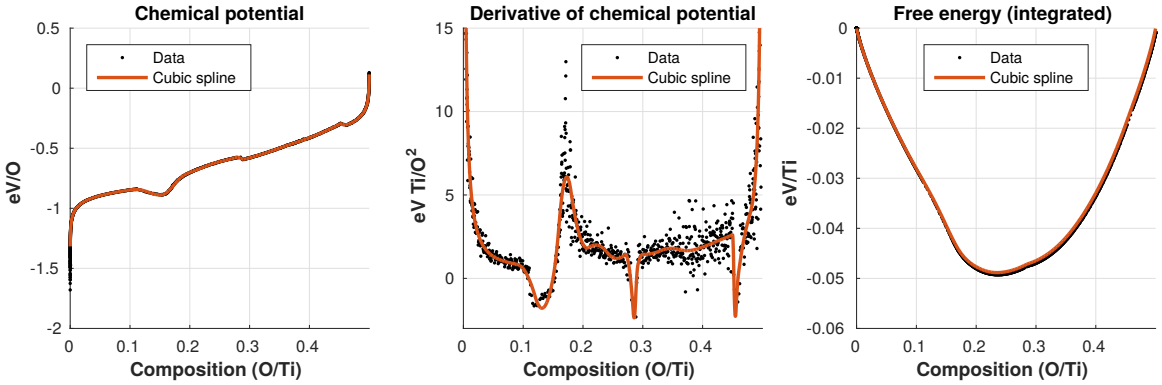

Figure 4.7: The chemical potential data is fit using a cubic spline with 25 knots. The corresponding numerical and analytical derivatives are plotted. The free energy is found from the chemical potential integral and is with respect to end members at $x = 0$ and $x = 1/2$. The spline accurately represents all three spinodals.

ing the curve fit methods described here, the degree 21 polynomial capture all three spinodals. The degree 15 polynomial represents only two (the first and third), and it

nearly produces a spurious spinodal at composition 0.05. The polynomial of degree nine captures one (the first spinodal), and degree five polynomial does not capture any spinodal regions. Clearly, to accurately represent all three spinodals with a R-K polynomial, a polynomial of high degree must be used.

A cubic spline was also used to fit $\Delta\mu$. Compare these results, shown in Figure 4.7, with the previous R-K polynomial fits. The spline clearly captures all three two-phase regions. This is done with minimal spurious oscillations in the derivative of the chemical potential and no spurious spinodal regions (see the center plot of Figure 4.7).

4.3 Phase field computations

This section explores the effect of the functional form chosen for the free energy fit on phase field simulations. Simulations of the diffusion of oxygen in HCP TiO_x were performed using free energy data fitted by various Redlich-Kister polynomial expansions and a cubic spline.

When in an oxygen rich environment, titanium will form such oxides as rutile [17, 18, 19], anatase TiO_2, and rock salt TiO [20, 21, 22, 23]. Additionally, due to the high solubility of oxygen in HCP titanium, a diffusion zone with lower concentrations of oxygen can exist below the oxide layer [24]. It has been shown that at low partial pressures, the relatively oxygen-rich oxides can become unstable, causing the oxygen to dissolve further within the titanium [16]. At these lower concentrations, a solid solution of HCP TiO_x forms, along with ordered $TiO_{1/6}$, $TiO_{1/3}$, and $TiO_{1/2}$ suboxides.

The solid solution TiO_x and the suboxides share the same HCP Ti sublattice. This allows the system to be well represented by a combined Cahn-Hilliard and Allen-Cahn description [103, 49, 109]. The free energy of the solid can be expressed as a function

of oxygen concentration x, order parameters $\eta_1, \ldots, \eta_p$, and their gradients:

$$\Pi = \int_V \frac{\mathrm{d}\boldsymbol{r}}{\Omega} \left(g(x, \eta_1, \ldots, \eta_p) + \sum_{i,j} \kappa_{ij} \frac{\partial x}{\partial r_i} \frac{\partial x}{\partial r_j} + \sum_{\alpha,\beta} \sum_{i,j} \Gamma_{ij}^{\alpha\beta} \frac{\partial \eta^\alpha}{\partial r_i} \frac{\partial \eta^\beta}{\partial r_j} \right) \tag{4.13}$$

where Ω is the volume of TiO_x per Ti atom, and the terms κ_{ij} and $\Gamma_{ij}^{\alpha\beta}$ are gradient energy coefficients. Note that x is a conserved variable while the order parameters are nonconserved variables.

The long-range diffusion of oxygen is modeled with the Cahn-Hilliard equation, where the oxygen flux $\boldsymbol{J}$ is related to the gradient of the oxygen chemical potential μ by the Onsager transport coefficient L [110], according to

$$\boldsymbol{J} = -L \nabla \mu \tag{4.14}$$

Combining this expression with the continuity equation gives the Cahn-Hilliard equation for the time evolution of oxygen concentration $c = x/\Omega$:

$$\frac{\partial c}{\partial t} = -\nabla \boldsymbol{J} \tag{4.15}$$

The oxygen chemical potential is equal to the variational derivative of the total free energy with respect to oxygen concentration:

$$\mu = \frac{\delta \Pi}{\delta x} \tag{4.16}$$

The Cahn-Hilliard equation is sufficient on its own to model the HCP solid solution TiO_x. However, an Allen-Cahn description is needed to capture the ordered suboxides that become stable at 800 K. The Allen-Cahn equation describing the evolution of

order paraemeter η_i has the form [109]

$$\frac{\partial \eta_i}{\partial t} = -\sum_j M_{ij} \frac{\delta \Pi}{\delta \eta_j} \tag{4.17}$$

where M_{ij} is a kinetic coefficient.

Since the ordering processes modeled by the Allen-Cahn equation involve only short-range diffusion, they will reach a local minimum much faster than the long-range diffusion processes represented by Cahn-Hilliard. The order parameters relax quickly to values that minimize the free energy based on the local value of the concentration. This suggests an effective Cahn-Hilliard description, where the order parameters are written as functions of the local concentration, i.e. $\eta_i(x(\boldsymbol{r}))$. The homogeneous free energy g can then be written solely as a function of x, and the gradients of the order parameters can be written in terms of ∇x. Eq. 4.13 then simplifies to the following form:

$$\Pi = \int_V \frac{\mathrm{d}\boldsymbol{r}}{\Omega} \left(g(x) + \sum_{i,j} \tilde{\kappa}_{ij} \frac{\partial x}{\partial r_i} \frac{\partial x}{\partial r_j} \right) \tag{4.18}$$

where the gradient energy coefficients $\tilde{\kappa}_{ij}$ depend on κ_{ij}, $\Gamma_{ij}^{\alpha\beta}$, and $\partial \eta_i / \partial x$.

The corresponding equation for the chemical potential is found by taking the variational derivative of the free energy in Eq. 4.18 with respect to the concentration, yielding the following:

$$\mu = \frac{1}{\Omega} \left[\frac{\partial g}{\partial x} - 2 \sum_{i,j} \tilde{\kappa}_{ij} \frac{\partial^2 x}{\partial r_i \partial r_j} \right] \tag{4.19}$$

where $\partial g / \partial x = \bar{m} u$ is the homogeneous chemcial potential defined in Eq. 4.3.

Considering the case where $\tilde{\kappa}_{ij} = (\hat{\kappa}/2)\delta_{ij}$ simplifies this equation further:

$$\mu = \frac{1}{\Omega} \left(\bar{\mu} - \hat{\kappa} \nabla^2 x \right) \tag{4.20}$$

By inserting this equation for the chemical potential into Eq. (4.14) and (4.15), the

result is the following Cahn-Hilliard equation:

$$\frac{\partial x}{\partial t} = \nabla \cdot \left[L \nabla \left(\bar{\mu} - \hat{\kappa} \nabla^2 x \right) \right] \tag{4.21}$$

The parameter $\hat{\kappa}$ and the average homogeneous chemical potential give a length scale for the interface $\sim \sqrt{\hat{\kappa}/|\bar{\mu}_{avg}|}$. Substituting the expression for the homogeneous chemical potential in Eq. (4.11) gives the following:

$$\frac{\partial x}{\partial t} = \nabla \cdot \left[L \nabla \left(k_B T \log \left(\frac{2x}{1-2x} \right) + \Delta\mu - \hat{\kappa} \nabla^2 x \right) \right] \tag{4.22}$$

The corresponding boundary conditions are

$$\begin{aligned} \nabla x \cdot \vec{\boldsymbol{n}} &= 0, \\ L \nabla \mu \cdot \vec{\boldsymbol{n}} &= \vec{J}, \end{aligned} \tag{4.23}$$

where the first boundary condition results from assuming equilibrium at the boundary, and the second represents an influx $\vec{J}$ at the boundary.

Because the cubic spline representation of the excess chemical potential is central to this study, the spline function is inserted into Eq. (4.22). The final form for the local Cahn-Hilliard equation, using the piecewise polynomial spline representation from equation (4.9) for $\Delta\mu$, is given by

$$\frac{\partial x}{\partial t} = \nabla \cdot \left[L \nabla \left(k_B T \log \left(\frac{2x}{1-2x} \right) + \sum_{i=0}^{m-1} P_{i,4} - \hat{\kappa} \nabla^2 x \right) \right] \tag{4.24}$$

where the piecewise cubic polynomials $P_{i,4}(x)$ are given by

$$P_{i,4} = \begin{cases} \sum_{j=0}^{3} D_{i,j} (x - \tau_i)^{3-j} & \tau_i \leq x < \tau_{i+1} \\ 0 & \text{otherwise} \end{cases} \tag{4.25}$$

The polynomial coefficients $D_{i,j}$ used in the computations presented here were obtained using the Octave `splinefit` function.

As described previously, the spline function can also be expressed as a linear combination of B-splines, following Eq. (4.8). This alternative form gives the following Cahn-Hilliard equation:

$$\frac{\partial x}{\partial t} = \nabla \cdot \left[L \nabla \left(k_B T \log \left(\frac{2x}{1-2x} \right) + \sum_{i=-3}^{m-1} c_i N_{i,k}(x)) - \hat{\kappa} \nabla^2 x \right) \right] \tag{4.26}$$

In addition to the phase field computations using a cubic spline fit for the excess chemical potential, simulations were also performed using the Redlich-Kister polynomial representation. A comparison of the resulting composition profiles, total energy, and computation times is presented here.

The code used solves the weak form of the Cahn-Hilliard equation with Isogeometric Analysis (IGA), which is a mesh-based numerical method that uses NURBS (Non-Uniform Rational B-Splines) as basis functions [111, 112]. The code was implemented using the `PetIGA` library [113].

4.3.1 Composition profiles

To demonstrate the effect of the curve fits from the previous section, 2D simulations were performed of the diffusion of oxygen within metallic Ti at 800K. The data for the excess chemical potential was fit with the cubic spline fit shown in Figure 4.7 and the R-K polynomial fits of degree 15 and 21 shown in Figure 4.6. The domain was $[0, 1] \times [0, 1]$ µm with a 1×500 element mesh. Initial conditions were a uniform composition gradient between $x = 0.005$ at $r_2 = 0$ and $x = 0.495$ at $r_2 = 1$. Zero flux boundary conditions were applied. The average value of the homogeneous chemical potential is $\bar{\mu}_{avg} = -0.634$. The value $\hat{\kappa} = 2.5e-4$ is used, which gives a length scale of about 0.02 µm. This is well resolved by the element length of 0.002 µm in the r_2

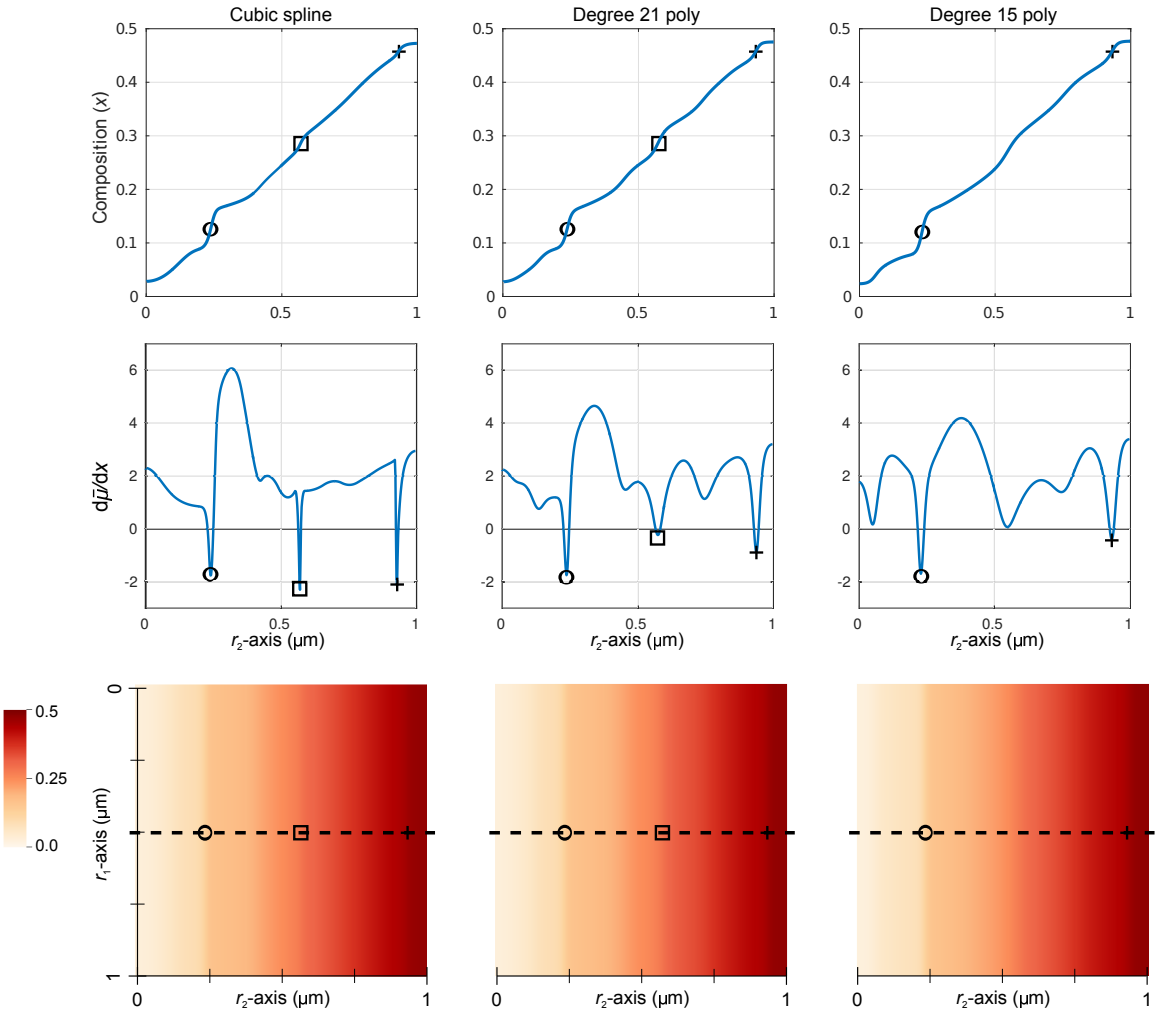

Figure 4.8: Simulation results show the effect of the curve fit on the composition profile. The bottom row of plots show the 2D simulation results after 100 s, colored according to the composition. The top row of plots show the composition profile found along the dotted line in the corresponding 2D plot. The middle row shows the derivative of the homogeneous free energy with respect to composition, $\mathrm{d}\bar{\mu}/\mathrm{d}x$. The phase interfaces (spinodals) captured by the respective chemical potential curve fits occur where $\mathrm{d}\bar{\mu}/\mathrm{d}x$ is negative, and they are marked by the circle, square, and plus sign. Note that the degree 15 polynomial missed the middle spinodal, causing that interface to be smoothed out.

direction.

Figure 4.8 shows the composition profile after 100 s for the three simulations, as well as the derivative of the homogeneous component of the chemical potential with respect to composition, $\mathrm{d}\bar{\mu}/\mathrm{d}x$. Recall that the two-phase regions correspond to the concave regions of the free energy, which is identified by a negative value

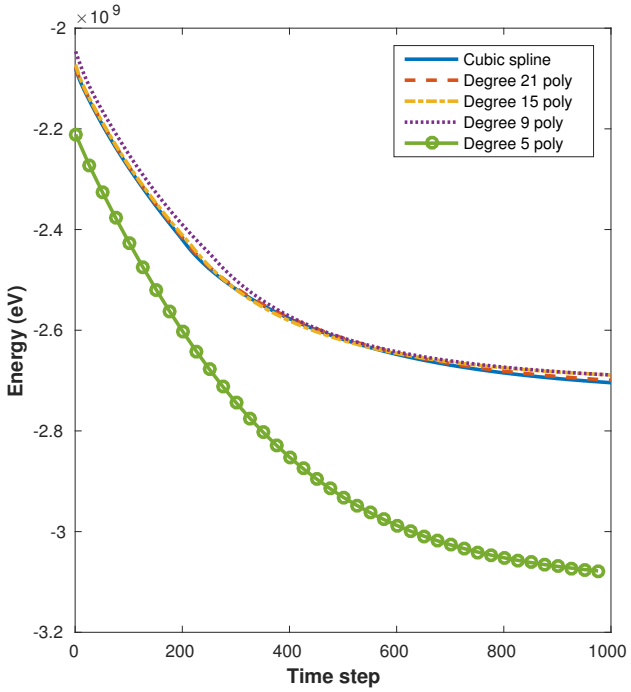

Figure 4.9: The time progression of total energy for a cubic spline fit is compared to polynomials of degree 5, 9, 15, and 21. Initial conditions were a uniform composition gradient of $[0, 0.49]$ per micrometer over a 1×500 element mesh. The results show 1000 time steps of 10 s using a constant mobility of $9 \times 10^{-6}\ \mu\text{m}^2/\text{s}$.

for $\mathrm{d}\bar{\mu}/\mathrm{d}x$. While the 800K data has three spinodal regions between $x = 0$ and $x = 0.5$, recall from Figure 4.6 that the degree 15 R-K polynomial does not capture the middle two-phase region. The effect of this is seen in Figure 4.8. Note that the cubic spline and the degree 21 polynomial have a well-defined interface near $r_2 = 0.6$, but this interface is smoothed out when using the degree 15 polynomial. Additionally, because a constant mobility L is used, every oscillation in the excess chemical potential function is reflected in the composition profile. Some of these oscillations are in the data itself; others result from the curve fit and can appear to be interfaces. However, even when it is difficult to identify the spinodal regions from the composition profile alone, the derivative of the homogeneous chemical potential clearly represents what is a true two-phase region.

4.3.2 Total free energy as a measure of accuracy

The accuracy of the free energy representations is compared by evaluating the time evolution of their total free energies, $\mathbf{F}$, given by Eq. (4.18). Two-dimensional simulations with the same conditions described previously ran for 1000 time steps of 10 s each, using a constant mobility of $9 \times 10^{-6}\,\mu m^2/s$. A thickness of $1\,\mu m$ was used in the calculation of total energy. These results are compared to the simulation that used the cubic spline fit, which is considered to most accurately represent the chemical potential of the physical system (see Figure 4.9). One would expect a good fit of the chemical potential to compute a total energy that matches the energy when using the spline fit.

The zero flux boundary conditions, together with the initial uniform composition gradient, result in a composition profile that gradually approaches a uniform composition of $x = 0.25$ in each simulation. The degree five R-K polynomial clearly overestimates the magnitude of the total free energy. To a lesser degree, the degree nine order polynomial underestimates the magnitude of the total free energy. This is consistent with the computed homogeneous free energy curves shown in Figure (4.6), where the degree 5 polynomial fit for the excess chemical potential results in a free energy curve significantly lower than the reference curve. The degree 9 R-K polynomial is slightly above the reference. The other two R-K polynomial fits and the spline fit match the reference free energy curve relatively well, which is reflected in the simulation results of Figure 4.9.

4.3.3 Assembly time

The effect on computation time of using the cubic spline as opposed the degree 21 polynomial was explored. Evaluation of the chemical potential and its derivatives takes place when the residual and Jacobian are evaluated and assembled in the phase field code. The additional terms in the degree 21 polynomial relative to the cubic

spline incur a significant increase in the number of floating point operations in the computation. To quantify this effect, 3D simulations of oxygen diffusion in metallic Ti were performed on a cube of length 2 μm with a $100 \times 100 \times 100$ element mesh using 160 processors. Zero flux boundary conditions were applied, with initial conditions of a uniform composition gradient between $x = 0.001$ at $r_1 = 0$ and $x = 0.499$ at $r_1 = 2$.

Wall times for assembly of the residual and the Jacobian for the first time step are shown in Table 4.1. There is a significant difference in the assembly times, with the polynomial fit taking more that 15 times as long to evaluate and assemble the residual and about 5 times as long for the Jacobian. This difference in computation time continues long after the first time step. The wall times, averaged over each time step, are plotted in Figure 4.10 for the first 100 time steps. The wall times for both simulations remain essentially constant over that time, with the residual and Jacobian taking about five and 15 times longer, respectively, when using the degree 21 polynomial instead of the cubic spline.

Note that for a system where a polynomial of lower degree provides a sufficient fit, the difference in wall time would decrease. For example, if the oxgyen diffusion in titanium at 1800K were simulated, as in Figure 4.3, a cubic polynomial would sufficiently represent the excess chemical potential, and there would be no decrease in computation time from using a cubic spline instead. However, for a complex free energy landscape, such as present in the diffusion of oxygen in Ti at 800K, the decrease in computation time achieved by using a cubic spline as opposed to a polynomial of high degree is significant.

4.4 Concluding remarks

Redlich-Kister polynomials have commonly been used to represent free energy functions. The global nature of the these polynomials often prevents them from capturing local phenomena. Spline functions present an effective alternative for rep-

Table 4.1: Comparison of wall times for residual and Jacobian assembly with cubic spline and degree 21 R-K polynomial fit for the first time step.

Newton	Residual time (s)		Jacobian time (s)	
iteration	Polynomial	Spline	Polynomial	Spline
0	21.0	1.37	1230	249
1	21.0	1.40	1240	249
2	20.9	1.32	1230	249
3	21.3	1.34	1230	249
4	20.9	1.32	1240	250

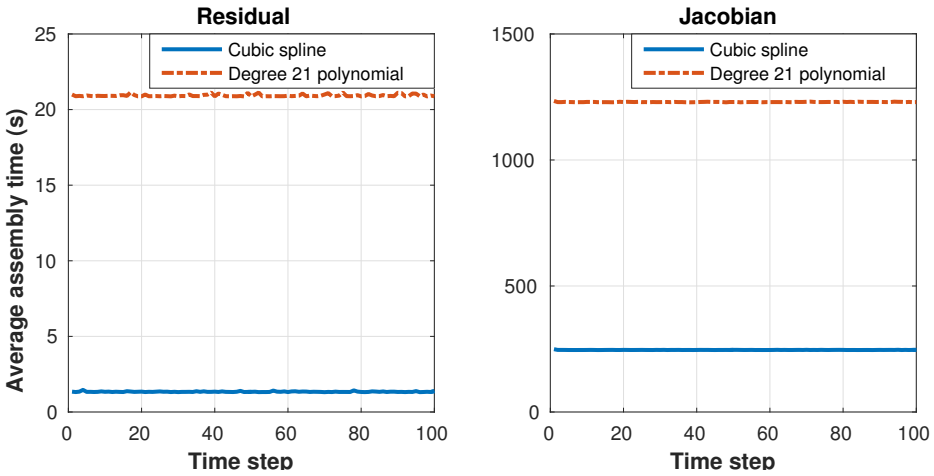

Figure 4.10: The residual and Jacobian assembly wall times, averaged over each time step, for 100 time steps.

resenting chemical potential and free energy data. Splines are piecewise polynomials with a specified order of continuity across the entire domain. Because of their piecewise structure, they are able to accurately represent local features of the data. The inherent constraints prescribing that the spline and a certain number of its derivatives be continuous across all subdomain junctions give splines an order of global continuity. These local and global properties make splines an important tool in curve fitting.

For a simple landscape, the R-K polynomial sufficiently models the chemical potential with a low polynomial degree. This is demonstrated by the high temperature data for diffusion of oxygen in metallic Ti, where a cubic R-K polynomial gave a sufficient representation of the excess chemical potential. This contrasts, however,

with more complex cases involving multiple regions of phase separation, where much higher polynomial degrees are needed when using the R-K polynomials. At the lower temperature of 800K, for example, the diffusion of oxygen in Ti produces three spinodal regions, and the R-K expansion requires a polynomial degree of around 20 to represent all three. These polynomials of high degree add complexity and can introduce spurious oscillations, but polynomials of lower degree potentially miss significant physics, such as the two-phase regions corresponding to a negative curvature of the free energy. Splines, however, are able to represent the fitted data and the associated physics with high accuracy while using a low degree.

To demonstrate the effect of the function type used to fit the excess chemical potential, phase field computations were performed of the diffusion of oxygen in titanium using a cubic spline fit and R-K polynomial fits of multiple degrees. Because the Allen-Cahn equations reach a minimum more rapidly than the Cahn-Hilliard equation, our phase field model is based on an effective Cahn-Hilliard equation. Using this model, the performance of a cubic spline fit was compared to the R-K polynomial fits in three ways. First, it is observed that, for this example, R-K polynomials of degree less than 21 fail to represent all three well-defined phase interfaces, while the cubic spline does. The effect of the function on the evolution of the total free energy of the system as it relaxes toward a homogeneous composition was studied, and it was found that the degree five and, to a lesser extent, the degree nine R-K polynomials misrepresent the magnitude of the total free energy. These two studies demonstrate that a degree 21 R-K polynomial gives a sufficient representation of the excess chemical potential for this particular data. An additional comparision was made of the computation time for the assembly of the residual and Jacobian using the cubic spline and the degree 21 R-K polynomial. The computation with the cubic spline evaluated and assembled the residual with a speedup of 15$\times$ and the Jacobian with a speedup of 5$\times$ relative to the computation using the degree 21 polynomial.

The ability of the cubic spline to capture all of the local physics of the system while minimizing spurious oscillations and computation time makes it a valuable tool in representing chemical potential and free energy functions.

CHAPTER V

Machine learning for predicting equilibrium precipitate morphology, and a comparison with the phase-field method

Magnesium alloys are attractive structural materials for multiple reasons. Magnesium has a low density compared to other commonly used structural metals, having two thirds the density of aluminum and one quarter the density of steel. It is an abundant material, making up 2.7% of the Earth's cruSt. Its specific heat and melting point make it ideal for casting methods [28, 29, 30, 31]. Its current use is limited by poor mechanical properties such as yield strength, formability, creep resistance, and corrosion resistance, even in many alloys. The improvement of material properties in Mg alloys depends in large part on precipitation and age hardening. This has been the focus of many studies and computational models, some of them focusing on promising Mg-Rare Earth alloys [32, 33, 34, 5, 35, 31, 3, 36, 37, 2]. This chapter presents a new approach to computational studies of precipitation, with Mg-RE alloys as a case study to develop the methods.

As shown in previous chapters, phase-field models such as those based on the Cahn-Hilliard or Allen-Cahn equations [52, 49] provide an effective framework for modeling the dynamics of material phase evolution. The effects of solid mechanics and

chemistry can be captured in the free energy functional so that their interactions will then be reflected in the variational derivatives used in both the phase-field equations and the Euler-Lagrange equations for mechanics. Phase-field models have been used repeatedly in studies of precipitate morphology [114, 115, 34, 5, 35, 36, 37]. The ability of phase-field methods to accommodate very general precipitate shapes is one of the strengths of this approach. The computations can, however, be time consuming due to the inherently serial nature of time-stepping schemes used in dynamic problems. Furthermore, as is well-known phase field dynamics can get stuck in local minima, and basins, or evolve slowly over very gradually descending free energy landscapes. Most phase field computations thererfore never reach equilibrium [116]. For these reasons it may be desirable to consider approaches of traversing the free energy landscape, or perhaps combine other approaches with phase field dynamics to mitigate these challenges.

Alternative methods that are natively better suited to explore the dynamics in parallel can be used to rapidly estimate equilibrium precipitate shapes. One method proposed and demonstrated in this chapter is to treat the prediction of equilibrium precipitate shape as an optimization problem, in which the energy is minimized over a set of potential geometries, subject to certain constraints (e.g. for a given volume). Such a problem can be made simpler through a change in how the precipitate shape is represented. The precipitate geometry in phase-field methods is often represented by a scalar field, which when discretized can easily lead to hundreds of thousands or millions of unknowns. The precipitate can instead be defined by many fewer parameters, such as the aspect ratios and volume of an ellipsoid or coefficients in a parametric representation of a surface. These geometric parameters become the variables in the optimization process.

If the free energy is an analytical function based solely on the shape parameters, standard gradient-based optimization methods may be applied. When finite

strain mechanics is included, there generally is not an analytical function relating the shape to the total strain energy. The values of the total energy will need to be numerically computed for a given set of shape parameters. In this or similar cases, derivative-free methods can be used [56]. Some examples of derivative-free optimization methods are genetic algorithms, simulated annealing, branch-and-bound search, and surrogate-based methods. Surrogate-based optimization methods use a surrogate model to approximate the objective function using data points over a given domain [57]. The surrogate model is used to find an approximate minimum, after which new data points are obtained and the model is updated. The process is repeated until specified stopping criteria are met. Machine learning regression methods, including Deep Neural Networks (DNN), have been as surrogate models in derivative-free optimization [58, 59, 60].

This chapter first demonstrates the use of Deep Neural Networks within a surrogate-model optimization framework to estimate the equilibrium shape of Mg-Y precipitates (see Figure 5.1). A phase-field approach is then described, and the resulting shape and computation time are compared with the DNN method. The DNN method is shown to be faster, but it lacks both the generality of shape type and the effect of dynamics and growth that exist in the phase-field method. Therefore, additional algorithms are discussed that combine the strengths of both methods, using phase-field for shape definition and dynamic effects and the DNN surrogate model optimization for improved computation time. An expanded role of machine learning in precipitate geometry prediction is also discussed.

5.1 DNN based shape prediction

This section describes the methodology for predicting the equilibrium shape of a Mg-Y precipitate for a given volume, using a DNN-based optimization routine. The corresponding results are reported.

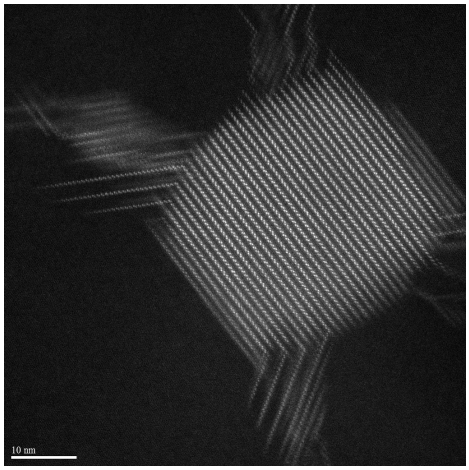

Figure 5.1: HAADF-STEM image of a MgY β' precipitate aged at 200° C (used by permission) [2].

5.1.1 Surrogate-based optimization

The basic approach in surrogate-based optimization methods is described by Vu ad co-workers [57] and is given by the following algorithm (quoting verbatim):

1. Phase 1 (design): Let $k := 0$. Select and evaluate a set S_0 of starting points.

2. While some given stopping criteria are not met:

   (a) Phase 2 (model): From the data $\{(x, f(x)) \,|\, x \in S_k\}$, construct a surrogate model $s_k(\cdot)$ that approximates the black-box function.

   (b) Phase 3 (search): Use $s_k(\cdot)$ to search for a new point to evaluate. Evaluate the new chosen point, update the data set S_k. Assign $k := k + 1$.

Phase 1 consists of sampling data points from the domain of the chosen variables. There are two important requirements for a good sampling (again quoting verbatim) [57]:

1. Space-fill: The design points should be uniformly spread over the entire design space.

2. Noncollapse: Two design points should not share any coordinate value if we do not know *a priori* which dimensions are important.

One commonly used noncollapsing method is Latin hypercube sampling [117], which can also be made space-filling. Another method that is both space-filling and non-collapsing is based on Sobol sequences [118, 119, 120]. Sobol sequences consist of n-dimensional points in a unit domain where the first m points are well-distributed for any m and no point projections are coincident. Using a Sobol sequence allows additional points to be continually added to an initial set of well-distributed points while maintaining the space-filling property of the updated set. Such a sequence was first suggested by Sobol [118] in the context of numerical integrals, but it has since been adopted in optimization schemes. The data points used in the current method are determined by the Sobol sequence. A description of the Direct Numerical Simulation (DNS) used to find the energy data points is given in Section 5.1.2.

Phase 2 involves the construction of the surrogate model. As mentioned previously, this work uses a Deep Neural Network for the surrogate model. This is done using the TensorFlow machine learning library [121] and is described in Section 5.1.3.

Phase 3, the search phase, can use a wide range of optimization techniques to minimize the surrogate model. Assuming the computation of gradients using the surrogate model is reasonable, standard gradient methods can be used. Since the TensorFlow library has implemented several variations of gradient descent for use in training the DNN weights, one of these gradient descent methods is also used here to minimize the energy as represented by the surrogate model. Multiple new data points are computed based on this minimum, and the dataset is updated accordingly.

5.1.2 Energy data from Direct Numerical Simulation (DNS)

The equilibrium precipitate shapes in this first work are assumed to depend on the strain energy and the interfacial energy. This total energy, given by the following

integral, is minimized for a given precipitate volume:

$$\Pi = \int_{\Omega} \psi \, \mathrm{d}V + \int_{\Gamma} \gamma(\boldsymbol{n}) \, \mathrm{d}S \tag{5.1}$$

where ψ is the strain energy density and $\gamma(\boldsymbol{n})$ is the orientation-dependent interfacial energy. The bulk chemical free energy, along with compositions and composition-dependent parameters, could also be included.

5.1.2.1 Strain energy

The strain energy of the precipitates was modeled with finite strain, continuum elasticity using the finite element method. The C++ code uses the deal.II finite element library [122]. The predefined precipitate surface is represented by the zero contour of a function, $F(x, y, z)$, or as a parametric surface, $\boldsymbol{r}(\phi, \theta)$. A structured finite element mesh was used that had been locally refined at the precipitate interface using hanging nodes. The jump in material parameters at the precipitate-matrix interface were smoothed linearly over multiple elements, representing a diffuse interface.

The displacement field is driven by the eigenstrain, resulting from the lattice parameter mismatch between the precipitate and the matrix. The value of the misfit strain is dependent on the composition of the precipitate [3]. The Mg-Y β' precipitate has a composition of Mg_7Y, corresponding to $c_Y = 0.125$ (see Table 5.1). The eigenstrain is applied within the precipitate using the multiplicative decomposition of the deformation gradient, $F = F^e F^\lambda$, where F^e is due to elasticity and F^λ is due to the eigenstrain.

The precipitate is embedded in a cube with a volume 6.4×10^4 times greater than that of the precipitate, and normal displacements on the boundary of the cube are constrained to be zero. A standard St. Venant-Kirchhoff strain energy density function is used, $\psi(\boldsymbol{E}) = \frac{1}{2}\boldsymbol{E} : \mathbb{C} : \boldsymbol{E}$, which is numerically integrated over the entire

Table 5.1: Deformation gradient representing the eigenstrain in the Mg-Y β' precipitate [3].

	$c_Y = 0.125$
F_{11}	1.0307
F_{22}	1.0196
F_{33}	0.9998

Table 5.2: Elasticity constants used for the Mg matrix [4] and the β' precipitate (calculated by AR Natarajan, unpublished data) (GPa).

	Mg	β'
$\mathbb{C}_{1111}$	62.6	78.8
$\mathbb{C}_{2222}$	62.6	62.9
$\mathbb{C}_{3333}$	64.9	65.6
$\mathbb{C}_{1122}$	26.0	24.6
$\mathbb{C}_{2233}$	20.9	19.9
$\mathbb{C}_{3311}$	20.9	23.1
$\mathbb{C}_{1212}$	18.3	11.9
$\mathbb{C}_{2323}$	13.3	11.6
$\mathbb{C}_{3131}$	13.3	8.46

domain to find the total strain energy. The elasticity constants used for the Mg matrix were calculated and reported by [4]. The elasticity constants for the matrix correspond with experimental data, although no such experimental data is available for the precipitate material. The elasticity constants used for the precipitate were also calculated using first principles methods (see Table 5.2).

The precipitate shape family was based on images of Mg-Y β' precipitates (see, for example, Figure 5.1) and is represented using the following function:

$$F(x, y, z) = \frac{x^4}{a^4} + \frac{y^4}{b^4} + \frac{z^4}{c^4} - 1 \tag{5.2}$$

where a, b,and c are the semi-axis lengths (see Figure 5.2). The interface can also be

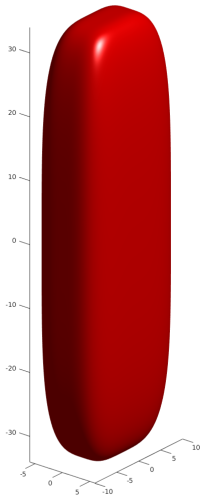

Figure 5.2: Example from the shape family used to represent the Mg-Y precipitate, with $a = 6$, $b = 10$, and $c = 34$.

expressed as a parametric surface on the domain $\phi \in [0, \pi)$, $\theta \in [0, 2\pi)$:

$$x = a\,\mathrm{sign}(\cos\theta)|\sin\phi\cos\theta|^{1/2} \tag{5.3}$$

$$y = b\,\mathrm{sign}(\sin\theta)|\sin\phi\sin\theta|^{1/2} \tag{5.4}$$

$$z = c\,\mathrm{sign}(\cos\phi)|\cos\phi|^{1/2} \tag{5.5}$$

The volume is given by the following integral:

$$V = 2abc \int_0^{\pi/2}\int_0^{\pi/2} \frac{(\cos\phi)^{3/2}}{(\sin\theta\cos\theta)^{1/2}}\,\mathrm{d}\phi\mathrm{d}\theta \tag{5.6}$$

$$\approx 6.481987abc \tag{5.7}$$

5.1.2.2 Interfacial energy

The interfacial energy per unit area at a point on the surface of the precipitate is dependent on the orientation of the surface normal. This anisotropic interfacial

Table 5.3: Interfacial energy between a β' Mg-Y precipitate and the Mg matrix [5].

Crystallographic plane	Interfacial energy (J/m^2)
(100)	0.03016
(010)	0.00436
(001)	0.02776

energy, $\boldsymbol{\gamma}$, and the unit normal, $\boldsymbol{n}$, are used to find the interfacial energy per unit area. The total interfacial energy, Π_Γ, is found by numerically integrating this expression over the parametric surface of the precipitate:

$$\Pi_\Gamma = \int_0^{\pi} \int_0^{2\pi} \boldsymbol{n} \cdot \boldsymbol{\gamma} \boldsymbol{n} \left\| \frac{\partial \boldsymbol{r}}{\partial \theta} \times \frac{\partial \boldsymbol{r}}{\partial \phi} \right\| \mathrm{d}\theta \mathrm{d}\phi \tag{5.8}$$

where $\boldsymbol{r}$ is the position vector $\langle x, y, z \rangle$ and $\boldsymbol{\gamma}$ is a diagonal matrix with the (100), (010), and (001) interfacial energies on the diagonals. The interfacial energy, $\boldsymbol{\gamma}$, for β' precipitates in Mg-Y was calculated and reported by Liu et al [5]. These values are shown in Table 5.3.

5.1.3 Deep Neural Network (DNN)

A neural network takes a set of inputs or "features" and maps them to a set of output or "target" values. It can be used for regression or classification problems. It is defined by multiple layers of units or "neurons", their associated weights, and activation functions (see Figure 5.3) [123, 124, 125, 126]. The input and output layers consist of the values of the input and output variables, with one or more hidden layers between the input and output layers. The number of layers and the number of units within each layer are called *hyperparameters* and define the neural network. A DNN has multiple hidden layers. The value of each unit within a given layer is computed based on the unit values and weights in the previous layer and the unit's activation function. Sigmoid functions have often been used as activation functions, although

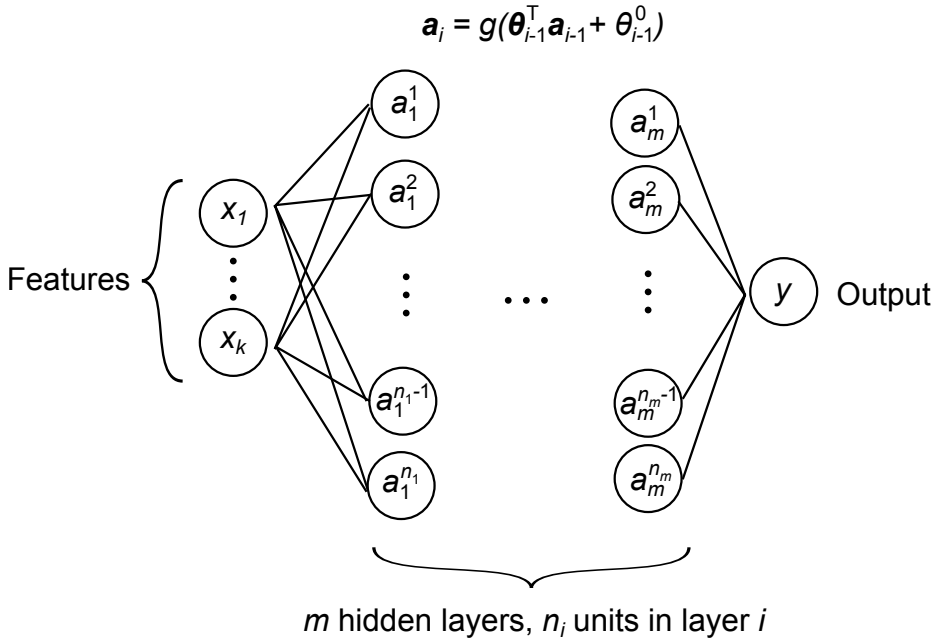

Figure 5.3: Schematic of a fully connected DNN.

rectified linear units (ReLU), defined by the function $g(x) = \max(x, 0)$, are commonly used as well. The activation value of unit j in layer i, denoted here by a_i^j, is calculated by the following equations:

$$a_i^j = g(z_{i-1}^j) \tag{5.9}$$

$$z_{i-1}^j = \theta_{j,i-1}^0 + \sum_k \theta_{j,i-1}^k a_{i-1}^k \tag{5.10}$$

where $g(x)$ is the activation function, $\boldsymbol{a}_{i-1}$ is the vector of activation values for the previous layer, $\boldsymbol{\theta}_{j,i-1}$ is the vector of weights, and $\theta_{j,i-1}^0$ is a bias value. When used for regression, activation functions are used to evaluate the activation values in the hidden layers, but not in the output layer. For example, if a single layer were used, the output value for regression would be given by $y = z_m^1 = \boldsymbol{\theta}_{1,m}^T \boldsymbol{a}_m + \theta_{1,m}^0$.

Training the DNN involves optimizing the weights and bias values to minimize a cost or loss function for a set of training data. The mean squared error (MSE) is a

commonly used loss function:

$$E = \frac{1}{N} \sum_I E_I \tag{5.11}$$

$$E_I = \left(y_I - y_I^{train}\right)^2 \tag{5.12}$$

where E is the MSE, N is the number of points in the training set, y_I is the DNN predicted target value for data point I, and y_I^{train} is the given target value of data point I. The weights and biases are often optimized using stochastic gradient descent or one of its variants. The gradient descent method finds a minimum by taking steps from a starting point in the direction given by the negative gradient, which is the direction of steepest descent. Evaluating the gradient can be computationally time consuming due to large numbers of data points in the training set. Stochastic gradient descent bypasses this difficulty by evaluating an average gradient based on a small set of example data points and updating the weights accordingly. This process is repeated for many different small sets from the training data until some stopping criteria is met (e.g. the loss function stops decreasing) [125].

The gradients of the error with respect to the weights are found using the *back-propagation* algorithm, which is derived using the chain rule. It makes use of the terms $\delta_i^j := \partial E_I / \partial z_i^j$ and consists of the following steps: [123]:

1. Evaluate the DNN for a given data point and store the values z_i^j (*forward propagation*).

2. Evaluate the terms δ_m^j for the output units, given by

$$\delta_m^j = g'(z_m^j) \frac{\partial E_I}{\partial y_j} \tag{5.13}$$

3. Back-propagate the values of δ_i^j through each layer, using the equation

$$\delta_i^j = g'(z_i^j) \sum_k \theta_{k,i+1}^j \delta_{i+1}^k \tag{5.14}$$

4. Evaluate the desired derivative using

$$\frac{\partial E_I}{\partial \theta_{j,i}^k} = \delta_i^j a_i^k \tag{5.15}$$

These gradients are then used with stochastic gradient descent to optimize the DNN weights.

A fully connected, deep neural network with ReLU activation functions is used for the surrogate model for the energy. The DNNRegressor model with AdagradOptimizer from the open source software library TensorFlow is used to create and train the neural network. The DNNRegressor model is defined by the number of hidden layers in the neural network and the number of units or neurons in each layer. The optimization function AdagradOptimzer requires a learning rate. The values of these hyperparameters (learning rate, number of hidden layers, number of units per layer) were determined through a random search [127].

Given a set of data, multiples sets of hyperparameters are created for comparison. These values are randomly selected over the following intervals:

- learning rate, log-uniformly between 1e-4 and 0.1
- number of hidden layers, uniformly between 8 and 15
- units per layer, uniformly between 5 and 120

The data are randomly split into 75% training data and 25% validation data. A deep neural network defined by each set of hyperparameters is trained with the training data for 15,000 iterations of the optimizer. The L_2-norm of the error between the

predicted and actual values for the validation data is computed. The hyperparameter set that produced the lowest error is then used to define the neural network for the current set of data.

5.1.4 Workflow and algorithm

A description of the algorithm used is described here, expanding on the basic algorithm from Section 5.1.1.

1. Values for the geometric features are chosen according to the Sobol sequence from a specified range of potential values, and the finite element computations are submitted to the HPC cluster. New jobs are immediately submitted upon completion of current jobs, so that a steady number of jobs are continually running in parallel with the training of the DNN. This develops a skeleton of the energy surface as a function of the chosen features.

2. Once a minimum number of DNS data are available, an initial set of hyperparameters is selected from 30 random hyperparameter sets. The following steps are then iterated over until a stopping criteria is met:

   (a) The five previous best hyperparameter sets are compared with five new, random hyperparameter sets to choose the hyperparameters for the current set of DNS data.

   (b) The DNS data is sorted according to the energy, and a set of 100 data points with the lowest energy are chosen for training.

   (c) A DNN is trained with the resulting data.

   (d) The energy as predicted by the DNN is minimized with respect to the geometry features. The result is a prediction for the equilibrium precipitate shape. This minimization is done using the AdagradOptimizer function in TensorFlow.

(e) 75 additional elasticity computations with geometry feature values near the current minimum are submitted to the HPC cluster, waiting for all but five to complete before proceeding. The range of geometry features used in new computations is exponentially tightened around the minimum as the iterations continue.

5.1.5 Simulation

The simulation workflow was executed on the ConFlux High Performance Computing (HPC) cluster at the University of Michigan. The ConFlux cluster includes 43 IBM Power8 CPU "Firestone" compute nodes with 20 physical cores (80 virtual cores) each and seventeen additional Power8 CPU "Minsky" nodes that each host four NVIDIA Pascal GPUs. All compute nodes and storage are connected using 100 Gb/s InfiniBand fabric. The workflow, machine learning, and optimization routines were implemented in Python and executed on the Minsky nodes, allowing the TensorFlow library to utilize the GPUs during machine learning and optimization. The DNS energy data were computed using a C++ finite element code on the Firestone nodes using 20 virtual cores for each computation. The high-speed interconnects enabled rapid transfer of the DNS data from the compute nodes to the GPUs performing the machine learning.

The equilibrium shape was found for a precipitate with a volume of 8,000 nm^3 and the shape family described in Section 5.1.2.1. The geometry features used were the log of the aspect ratios, i.e. $\ln(a/b)$ and $\ln(c/b)$. The precipitate was centered in a cube with side lengths of 800 nm to remove any boundary effects on the elasticity. The mesh was locally refined at the precipitate interface with element length of 0.26 nm. The thickness of the diffuse interface was 2 nm.

5.2 Phase-field model

The aging process for a single β' precipitate in Mg–10 wt.% Y (Mg–2.95 at.% Y) at 200° C was simulated using a phase field model. The crystal structure was described by an order parameter, η, where $\eta = 0$ corresponds to α-Mg, $\eta = 1$ to the ordered β' precipitate. Values of η between 0 and 1 define the diffuse interface. The composition of Y is described by a composition field variable, c. Finite strain effects were also considered, so a displacement vector field, $\boldsymbol{u}$, was also included in the model. The Kim-Kim-Suzuki (KKS) model was used, in which the two phases in the diffuse interface are considered to have the same chemical potential rather than the same composition [128]. The form of the equations used here closely follows that of Ji et al. [35].

The Gibbs free energy is defined by the following integral:

$$\Pi[c, \eta, \boldsymbol{u}] = \int_{\Omega} \left(f(c, \eta) + f_{grad}(\nabla\eta) + \psi(\boldsymbol{F}^e(\eta, \boldsymbol{F}), \eta) \right) \mathrm{d}V - \int_{\partial\Omega_T} \boldsymbol{T} \cdot \boldsymbol{u} \, \mathrm{d}S \qquad (5.16)$$

where $f(c, \eta)$ is the local chemical free energy density, $f_{grad}(c, \eta)$ is the gradient energy term, and $\psi(\boldsymbol{F}^e(\eta, \boldsymbol{F}), \eta)$ is the strain energy density.

5.2.1 Local free energy

The local chemical free energy density includes the bulk chemical free energy and the Landau free energy describing the structure change. The bulk chemical free energy is written in terms of the chemical free energies of the α and β' phases and the function $h(\eta)$, where $h(0) = 1$, $h(1) = 1$, and $h'(0) = h'(1) = 0$. The Landau free

Table 5.4: Coefficients in the chemical free energy density for the Mg-Y solid solution at 200° C (kJ mol^{-1}) [6].

G_{Mg}	-16.564
G_{Y}	-21.561
L_0	-20.016
L_1	-2.836

energy has wells at $\eta = 0$ and $\eta = 1$.

$$f(c,\eta) = f^{\alpha}(c^{\alpha})\,(1 - h(\eta)) + f^{\beta'}(c^{\beta'})h(\eta) + \omega f_{Landau}(\eta) \tag{5.17}$$

$$h(\eta) = 3\eta^2 - 2\eta^3 \tag{5.18}$$

$$f_{Landau}(\eta) = \eta^2 - 2\eta^3 + \eta^4 \tag{5.19}$$

The full form of the chemical free energy of the Mg-Y solid solution is given by the following function [6, 5]:

$$\begin{aligned} f^{\alpha}(c^{\alpha}) = {} & (1-c^{\alpha})G_{\mathrm{Mg}} + c^{\alpha}G_{\mathrm{Y}} + c^{\alpha}(1-c^{\alpha})(L_0 + L_1(1-2c^{\alpha})) \\ & + RT((1-c^{\alpha})\log(1-c^{\alpha}) + c^{\alpha}\log(c^{\alpha})) \end{aligned} \tag{5.20}$$

where the values for the coefficients at 200° C are given in Table 5.4. The chemical free energy of the β' precipitate is written such that a common tangent exists at $f^{\alpha}(0.01)$ and $f^{\beta'}(0.125)$ [5]. The functions $f^{\alpha}(c^{\alpha})$ and $f^{\beta'}(c^{\beta'})$ can approximated as quadratic functions of the following form:

$$f^{\alpha}(c^{\alpha}) = A^{\alpha}(c^{\alpha} - c_0^{\alpha})^2 + B^{\alpha} \tag{5.21}$$

$$f^{\beta'}(c^{\beta'}) = A^{\beta'}(c^{\beta'} - c_0^{\beta'})^2 + B^{\beta'} \tag{5.22}$$

where the parameters are given in Table 5.5.

The following constraint equations act to maintain the equal chemical potential

Table 5.5: Parameters in the quadratic chemical free energy density descriptions.

A^{α}	6.2999	nN/nm^2
B^{α}	-1.6062	nN/nm^2
c_0^{α}	0.2635	
$A^{\beta'}$	704.23	nN/nm^2
$B^{\beta'}$	-1.5725	nN/nm^2
$c_0^{\beta'}$	0.1273	

condition and define the values c^{α} and $c^{\beta'}$:

$$c = (1 - h(\eta))c^{\alpha} + h(\eta)c^{\beta'} \tag{5.23}$$

$$\frac{\partial f}{\partial c} = \frac{\partial f^{\alpha}}{\partial c^{\alpha}} = \frac{\partial f^{\beta'}}{\partial c^{\beta'}} \tag{5.24}$$

Equations (5.21)-(5.24) can be used to find the following expressions for c^{α} and $c^{\beta'}$:

$$c^{\alpha} = \frac{A^{\beta'}\left[c - c_0^{\beta'}h(\eta)\right] + A^{\alpha}c_0^{\alpha}h(\eta)}{A^{\alpha}h(\eta) + A^{\beta'}(1 - h(\eta))} \tag{5.25}$$

$$c^{\beta'} = \frac{A^{\alpha}\left[c - c_0^{\alpha}(1 - h(\eta))\right] + A^{\beta'}c_0^{\beta'}(1 - h(\eta))}{A^{\alpha}h(\eta) + A^{\beta'}(1 - h(\eta))} \tag{5.26}$$

5.2.2 Gradient energy

An anisotropic gradient energy term is used, where the second order tensor $\boldsymbol{\kappa}$ is related to the anisotropic interfacial energy:

$$f_{grad}(\nabla\eta) = \frac{1}{2}\nabla\eta \cdot \boldsymbol{\kappa}\nabla\eta \tag{5.27}$$

The components of $\boldsymbol{\kappa}$ can be related to the barrier height ω, the interface thickness (2λ), and the interfacial energy $\boldsymbol{\gamma}$:

$$\gamma_{ij} = \frac{\sqrt{\kappa_{ij}\omega}}{3\sqrt{2}} \tag{5.28}$$

$$2\lambda = 2.2\sqrt{\frac{2\kappa_{ij}}{\omega}} \tag{5.29}$$

This study used the following values for $\boldsymbol{\kappa}$ and ω:

$$\boldsymbol{\kappa} = \begin{bmatrix} 0.08225 & 0 & 0 \\ 0 & 0.001743 & 0 \\ 0 & 0 & 0.06968 \end{bmatrix}, \omega = 0.199056 \tag{5.30}$$

5.2.3 Strain energy

The strain energy is modeled using a St. Venant-Kirchhoff model. The elasticity constants are modeled as being dependent on the order parameter to represent the difference in elasticity between the two phases. The strain energy is driven by a strain mismatch between the crystal structures of the phases. The stress-free transformation tensor of the β' precipitate $\boldsymbol{F}^{\beta'}$ and the order parameter are used to determine the misfit strain, represented by $\boldsymbol{F}^{\lambda}$. A multiplicative decomposition of the total deformation gradient into the parts due to elasticity and the misfit strain is used:

$$\psi(\boldsymbol{F}^e(\eta, \boldsymbol{F}), \eta) = \frac{1}{2}\boldsymbol{E} : (\mathbb{C}^{\alpha}(1 - h(\eta) + \mathbb{C}^{\beta'}h(\eta)) : \boldsymbol{E} \tag{5.31}$$

$$\boldsymbol{E} = \frac{1}{2}\left(\boldsymbol{F}^{e\mathsf{T}}\boldsymbol{F}^e - \mathbb{1}\right) \tag{5.32}$$

$$\boldsymbol{F}^e(\eta, \boldsymbol{F}) = \boldsymbol{F}\boldsymbol{F}^{\lambda^{-1}}(\eta) \tag{5.33}$$

$$\boldsymbol{F}^{\lambda}(\eta) = \mathbb{1}(1 - h(\eta)) + \boldsymbol{F}^{\beta'}h(\eta) \tag{5.34}$$

5.2.4 Phase-field and equilibrium equations

The phase field dynamics following the KKS model are modeled with the diffusion and Allen-Cahn equations, of the following forms [49]:

$$\frac{\partial c}{\partial t} = -\nabla \cdot (-M\nabla\mu_c) \tag{5.35}$$

$$\frac{\partial \eta}{\partial t} = -L\mu_{\eta} \tag{5.36}$$

where M is the mobility and L is the kinetic coefficient. The chemical potentials $\mu_c = \delta\Pi/\delta c$ and $\mu_\eta = \delta\Pi/\delta\eta$ are found using standard variational methods, giving the following expressions when assuming $\nabla\eta \cdot \boldsymbol{\kappa}\boldsymbol{n} = 0$:

$$\mu_c = \frac{\partial f^\alpha}{\partial c}\left(1 - h(\eta)\right) + \frac{\partial f^{\beta'}}{\partial c} h(\eta) \tag{5.37}$$

$$\mu_\eta = \left[f^{\beta'} - f^\alpha - \mu_c(c^{\beta'} - c^\alpha)\right]\frac{\partial h}{\partial \eta} - \nabla\eta \cdot \boldsymbol{\kappa}\nabla\eta + \omega\frac{\partial f_{Landau}}{\partial \eta} + \frac{\partial \psi}{\partial \eta} \tag{5.38}$$

where

$$\frac{\partial \psi}{\partial \eta} = \left(\frac{1}{2}\boldsymbol{E} : (\mathbb{C}^{\beta'} - \mathbb{C}^\alpha) : \boldsymbol{E} - \boldsymbol{P} : \left(\boldsymbol{F}^e(\boldsymbol{F}^{\beta'} - \mathbb{1})\boldsymbol{F}^{g^{-1}}\right)\right)\frac{\partial h}{\partial \eta} \tag{5.39}$$

Using the definition $\bar{\mu}_\eta := \mu_\eta + \nabla \cdot (\boldsymbol{\kappa}\nabla\eta)$, the corresponding weak forms are the following (assuming M and L to be uniform and constant):

$$\int_\Omega \left(w\frac{\partial c}{\partial t} + \nabla w \cdot (M\nabla\mu_c)\right) \mathrm{d}V + \int_{\partial\Omega} w\boldsymbol{J} \cdot \boldsymbol{n}\, \mathrm{d}S = 0 \tag{5.40}$$

$$\int_\Omega \left(w\left(\frac{\partial \eta}{\partial t} + L\bar{\mu}_\eta\right) + L\nabla w \cdot (\boldsymbol{\kappa}\nabla\eta)\right) \mathrm{d}V = 0 \tag{5.41}$$

where the flux is defined by $\boldsymbol{J} := -M\nabla\mu_c$.

The equilibrium conditions for mechanics are found by setting the first variation of the free energy functional with respect to the displacement equal to zero. This gives the following weak form:

$$\int_\Omega \nabla\boldsymbol{w} : \left(\boldsymbol{P}\boldsymbol{F}^{\lambda^{-\mathsf{T}}}\right) \mathrm{d}V = \int_{\partial\Omega_T} \boldsymbol{w} \cdot \boldsymbol{T}\, \mathrm{d}S \tag{5.42}$$

with the corresponding strong form:

$$\text{Div}\left(\boldsymbol{P}\boldsymbol{F}^{\lambda^{-\mathsf{T}}}\right) = 0 \text{ in } \Omega \tag{5.43}$$

$$\left(\boldsymbol{P}\boldsymbol{F}^{\lambda^{-\mathsf{T}}}\right)\boldsymbol{N} - \boldsymbol{T} = 0 \text{ on } \partial\Omega_T \tag{5.44}$$

5.2.5 Simulation

The phase-field and equilibrium equations were solved simultaneously using the finite element method and implemented in C++ using the deal.II library. A backward Euler time stepping scheme was used for the phase-field dynamics. The code was run in parallel on 160 cores over ten compute nodes. A single, spherical precipitate at about one-half the volume of interest was used as an initial condition. This was allowed to evolve and grow until reaching a volume of 8,000 nm^3. The same domain and a similar mesh refinement were used as in Section 5.1.5.

5.3 Results

At a volume of 8,000 nm^3, the DNS-DNN method predicted aspect ratios of $a/b \approx 0.60$ and $c/b \approx 3.4$, which corresponds to dimensions 10.1 nm $\times$ 16.9 nm $\times$ 57.9 nm. The results from the phase-field method show aspect ratios of $a/b \approx 0.69$ and $c/b \approx 2.5$, which corresponds to 14.0 nm $\times$ 20.2 nm $\times$ 49.6 nm. Figures 5.4 and 5.5 show the predicted shapes using the two methods using 2D slices of the 3D simulations.

The convergence of the DNS-DNN based optimization method is shown in Figure 5.6. This plot shows the decrease in the L_2-norm of the error of the feature vector $[\ln(a/b)\ \ln(c/b)]^{\mathsf{T}}$, where the DNS data point giving the lowest overall energy is taken as the true minimum. After six iterations, the percent error for $\ln(a/b)$ was 0.0255% and for $\ln(c/b)$ was 0.00624% . The computation time elapsed after six iterations was

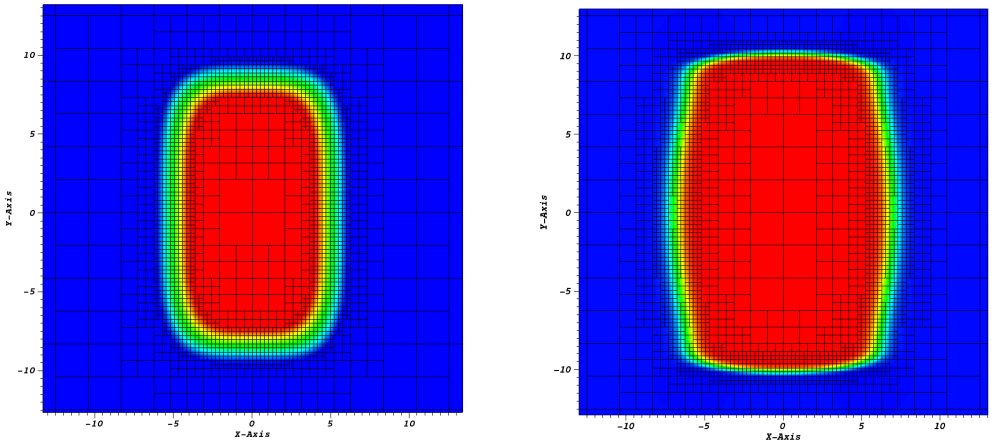

(a): DNS-DNN method (b): Phase-field method

Figure 5.4: Precipitate simulation results showing the xy-plane at $z = 0$. The precipitate is colored red and the solid-solution is blue.

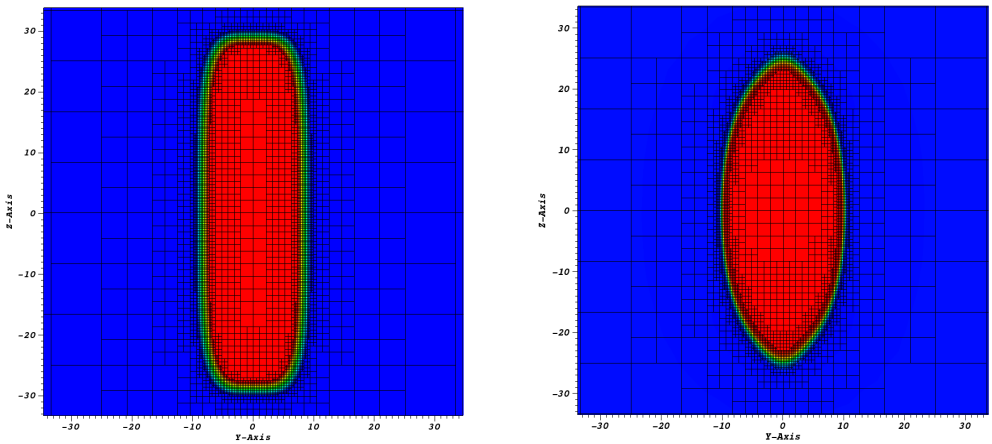

(a): DNS-DNN method (b): Phase-field method

Figure 5.5: Precipitate simulation results showing the yz-plane at $x = 0$. The precipitate is colored red and the solid-solution is blue.

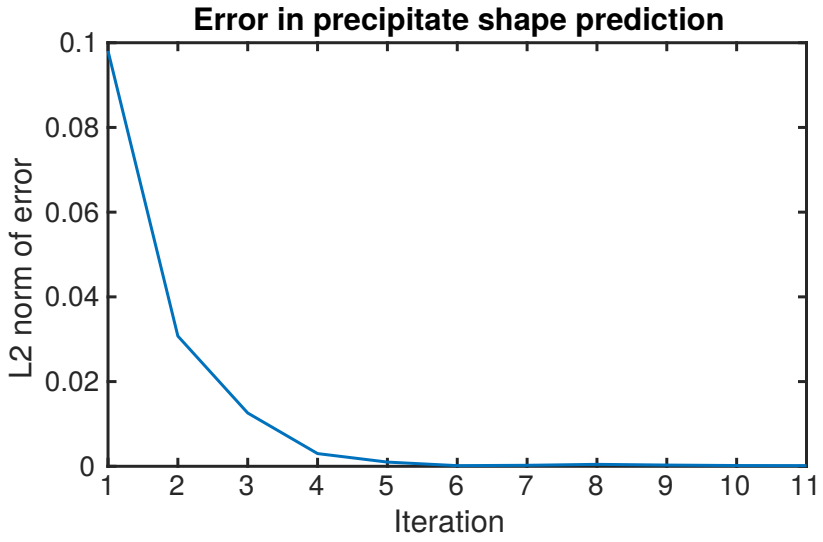

Figure 5.6: Convergence of the DNN based optimization scheme based on the L_2-norm of the error of the feature vector $[\ln(a/b)\ \ln(c/b)]^{\mathsf{T}}$.

Table 5.6: Computation time for the DNS-DNN optimzation and phase-field methods.

	DNS-DNN	Phase-field
Computation time (sec)	12832	91037
Iterations/time steps	6	75
Avg. iteration/step time (sec)	2139	1214

12832 sec (3.56 hrs).

The precipitate modeled with the phase-field method grew to 8,000 nm^3 after 78 time steps, with a computation time of 91037 sec (25.3 hr), or about 7 times as long as the DNS-DNN based method. Computation times are compared in Table 5.6.

5.4 Discussion

As expected, the DNS-DNN method of predicting the precipitate shape is significantly faster than the phase-field method, due to the time-dependent nature of the phase-field equations. However, this advantage comes at the price of simplifying the shape description. The result is that while, in general, the dimensions and shapes are comparable, particularly in the xy-plane shown in Figure 5.4, the yz-plane in Figure 5.5 shows noticeable differences. Phase-field's ability to represent a wide

range of shapes is one great advantage. This advantage is particularly important if there is little or no experimental data on a precipitate's shape. While the DNS-DNN method could be improved by using a more general shape description with a higher number of parameters, it is possible to use the DNS-DNN and phase field methods together to take advantage of both of their strengths. The following algorithms are some suggestions.

5.4.1 Geometry-informed DNS-DNN algorithm

Use the phase-field method to determine the shape family to be used in the DNS-DNN method. Multiple 2D simulations or a coarse 3D simulation could be sufficient to identify an appropriate shape family, while keeping the phase-field computation time to a minimum. This more accurate shape family is then be used with the DNS-DNN method as described in Section 5.1.4.

5.4.2 Geometry-informed phase-field algorithm

Use a generic shape family with the DNS-DNN method to predict an equilibrium shape. Use this shape as the initial condition in the phase field model. The phase-field model will refine this to a more accurate precipitate shape. The computation time required for the phase-field dynamics should be significantly reduced by having an initial condition that is near the equilibrium condition. This algorithm could be combined with the previous algorithm when necessary.

5.4.3 DNS-DNN algorithm with composition and volume features

Another reason for discrepancies in the results is due to the fact that the precipitate in the phase-field simulation is far from equilibrium with respect to bulk chemical free energy, causing the precipitate to continue to grow. A single equilibrium precipitate would be orders of magnitude larger than 8,000 nm^3 for the domain size and

average concentration of Y used here. However, in an actual system there would be many more precipitates, leading relatively smaller equilibrium sizes. Including these additional precipitates in the simulation or simply decreasing the domain size would be possible ways to ensure that the precipitates reach a near equilibrium state at a realistic size. If seeking equilibrium with respect to bulk chemical free energy as well as strain and interfacial energies, the following method can be used:

Use the DNS-DNN method as previously described, but seek an equilibrium shape for a given average concentration c_{avg} rather than a given volume. The precipitate volume $V^{\beta'}$ and precipitate composition $c^{\beta'}$ are included as features to be optimized, and the bulk chemical free energy is included in the total energy. The total energy would then be as follows:

$$\Pi = f^{\beta'}(c^{\beta'})V_{\beta'} + f^{\alpha}(c^{\alpha})(V_{\Omega} - V_{\beta'}) + \int_{\Omega} \psi \, \mathrm{d}V + \int_{\Gamma} \gamma(\boldsymbol{n}) \, \mathrm{d}S \tag{5.45}$$

The dependence of the misfit strain or other parameters on the composition could be included as well. The concentration of Y in the α-Mg matrix, c^{α}, is calculated using the total domain volume V_{Ω}:

$$c^{\alpha} = \frac{c_{avg} V_{\Omega}}{V_{\Omega} - V_{\beta'}} \tag{5.46}$$

5.4.4 An expanded role for machine learning

Machine learning can play a larger role than simply using a DNN as a surrogate model for the total energy. The simulations and algorithms described to this point in the chapter have dealt with finding the precipitate shape for a given material. These methods can be applied to compute precipitate shape data for a wide range of material types. With sufficient data, a DNN can then be trained to directly predict the precipitate shape (rather than the energy) based on material parameters such

as elasticity constants for the precipitate and the matrix, interfacial energies, and misfit strain values. A classification DNN might predict the shape family while a regression DNN predicts the corresponding parameter values. This would include a large number of features, which in turn requires an enormous number of data points. For the 24 features mentioned here (18 elasticity constants, 3 interfacial energies, 3 components of the misfit strain), two data points in each dimension would result in over 16 million data points. Three data points in each dimension is over 282 billion. Due to the curse of dimensionality, the number of features would initially be smaller and increase over time as additional data are computed or observed. Such a tool would become increasingly valuable in the design of materials as the dataset grows and training progesses.

5.5 Concluding remarks

Precipitation in Mg alloys is a key element in improving their material properties and expanding the potential applications of Mg alloys. The ability to predict precipitate morphology can be a valuable tool in designing alloys. The phase-field method is well-suited to modeling the dynamics of precipitate growth and evolution and incorporating the effects of elasticity. Its inhibiting factor is its time dependence. This chapter has demonstrated the use of a DNN-based optimization method using DNS data as a way to remove the dependence on inherently serial time-stepping schemes. It was compared to a phase-field model using diffusion, Allen-Cahn, and equilibirum, finite-strain elasticity.

While the DNS-DNN method gives comparable results to the phase-field method for the example in this chapter, it is restricted by the chosen shape family. Multiple additional algorithms were suggested to use the DNS-DNN and phase-field methods together to mitigate the effects of time-dependence in phase-field and the restrictive shape family in the DNS-DNN method. The combination of methods has the poten-

tial to predict more accurate precipitate shapes with relatively shorter computation times.

CHAPTER VI

Conclusion

The purpose of the methods presented in this dissertation is to provide additional mathematical and computational tools to study physical phenomena in materials with multiple phases. Although these methods can be applied generally, they have been explained in the setting of specific material phenomena. These include the diffusionless phase changes of martensitic transformations, the multiple ordered phases in the oxidation of titanium, and the morphology of β' Mg-Y precipitates. The free energy of each system plays a central role in the framework and methods presented, including in the derivation of Euler-Lagrange equations of equilibrium, the definition of chemical potentials used in phase-field dynamics, and the DNN-based energy minimization algorithms.

The goal to provide a framework incorporating displacements associated with phase changes along with standard deformations and chemical diffusion was treated in Chapters II and III. This framework relies on a configurational description of these displacement fields and their associated free energy. Variational methods are used to find the equilibrium equations and define chemical potentials. This framework can be applied in other material system involving displacements or deformations caused by phase changes.

The need to represent free energy data in a manner that is both accurate and

computationally efficient was explored in Chapter IV. Cubic splines are shown to be effective in capturing rapid fluctuations in free energy data while maintaining low computation times in comparison to high-order global polynomials.

Algorithms to predict precipitate morphology, based on machine learning methods, were discussed in Chapter V. The benefit of these methods lies in the potential reduction in computational time compared with using phase-field dynamics alone. The interactions between the DNN-based optimization routine and the phase-field model play a key role in these algorithms. Due to the influence of precipitate morphology on material properties, these methods can provide a tool in planning experiments and designing metal alloys.

This dissertation suggests several avenues for future work, including the following:

1. The framework described in Chapter II described both sharp and diffuse interfaces. This framework could potentially be extended to describe the transition that occurs as coherent interfaces become incoherent.

2. Chapter III presented a model for voiding that incorporated mechanics and Cahn-Hilliard dynamics to model vacancy condensation and the effects of oxide stresses. The implementation of this model will require the ideas described in Section 3.3 for the free energy surface to be represented mathematically. It may be possible to represent such a surface qualitatively with combinations of basic global functions. Representation of a more realistic free energy surface, however, may require more advanced function types. This leads into the next item.

3. The free energy data used in Chapter IV was dependent on a single variable. The free energy can, however, depend on many more variables. The mathematical representation of realistic free energy data as a function of multiple variable is an area of interest. Potential function types include non-uniform rational basis

splines (NURBS) and DNN representations.

4. Multiple algorithms combining the DNS-DNN method and phase-field dynamics were presented in Chapter V. The implementation of these algorithms require only slight modifications to the computations presented.

5. The implementation of machine learning to directly predict precipitate morphology based on a wide range of material parameters would be a valuable tool in materials' design. Such an implementation will involve an ongoing series of computations to create a large dataset of material parameters and their associated precipitate shape. The free energies, elasticity constants, kinetic parameters, etc. that will be needed for a large set of materials will be supplied by connecting to statistical mechanics and DFT-based codes. These codes will also apply machine learning wrappers, allowing the prediction of desired parameters for a given material. The software can be made available, allowing for collaboration in the creation of data and refinement of the models. The continual addition of data will require ongoing training of the machine learning methods used.

APPENDICES

APPENDIX A

Variational formulation for the sharp interface problem

Consider variations on the configurational displacement, $\boldsymbol{U}^{\varepsilon} := \boldsymbol{U} + \varepsilon \boldsymbol{W}$, and on the Newtonian displacement, $\boldsymbol{u}^{\varepsilon} := \boldsymbol{u} + \varepsilon \boldsymbol{w}$. The first variation is found using the functional defined over Ω_0. At equilibrium, the first variation of the Gibbs free energy is zero.

$$
\begin{aligned}
\frac{\mathrm{d}}{\mathrm{d}\varepsilon}\Pi[\boldsymbol{u}^\varepsilon;\boldsymbol{U}^\varepsilon]\bigg|_{\varepsilon=0} =& \frac{\mathrm{d}}{\mathrm{d}\varepsilon}\Bigg\{ \int_{\Omega_0} \psi(\boldsymbol{F}^\varepsilon, \boldsymbol{\kappa}^\varepsilon(\boldsymbol{X}^0)) \det \boldsymbol{\chi}^\varepsilon \,\mathrm{d}V_0 \\
& - \int_{\Omega_0} (\boldsymbol{\kappa}^\varepsilon(\boldsymbol{X}^{\mathbf{0}})) \cdot \boldsymbol{u}^\varepsilon \det \boldsymbol{\chi}^\varepsilon \,\mathrm{d}\mathbf{V_0} \\
& - \int_{\partial\Omega^{\mathrm{S}}_{T_0}} \boldsymbol{T}^0 \cdot \boldsymbol{u}^\varepsilon \,\mathrm{d}S_0 \Bigg\}\Bigg|_{\varepsilon=0} \\
=& \Bigg\{ \int_{\Omega_0} \left[\frac{\partial \psi}{\partial \boldsymbol{F}} : \frac{d\boldsymbol{F}^\varepsilon}{d\varepsilon} + \frac{\partial \psi}{\partial \boldsymbol{\kappa}} \cdot \frac{d\boldsymbol{\kappa}^\varepsilon}{d\varepsilon} \right] \det \boldsymbol{\chi} \,\mathrm{d}V_0 \\
& + \int_{\Omega_0} \psi \frac{\mathrm{d}}{\mathrm{d}\varepsilon} \det \boldsymbol{\chi}^\varepsilon \,\mathrm{d}V_0 - \int_{\Omega_0} \cdot \boldsymbol{u} \frac{\mathrm{d}}{\mathrm{d}\varepsilon} \det \boldsymbol{\chi}^\varepsilon \,\mathrm{d}\mathbf{V_0} \\
& - \int_{\Omega_0} \left(\cdot \frac{\mathbf{d}\boldsymbol{u}^\varepsilon}{\mathbf{d}\varepsilon} + \boldsymbol{u} \cdot \frac{\partial}{\partial \boldsymbol{\kappa}} \cdot \frac{\mathbf{d}\boldsymbol{\kappa}^\varepsilon}{\mathbf{d}\varepsilon} \right) \det \boldsymbol{\chi} \,\mathrm{d}V_0 \\
& - \int_{\partial\Omega^{\mathrm{S}}_{T_0}} \boldsymbol{T}^0 \cdot \frac{d\boldsymbol{u}^\varepsilon}{d\varepsilon} \,\mathrm{d}S_0 \Bigg\}\Bigg|_{\varepsilon=0} \\
=& \, 0
\end{aligned}
\tag{A.1}
$$

Consider the first variation of $\boldsymbol{F}$, recalling equation (2.7):

$$
\begin{aligned}
\frac{d\boldsymbol{F}^\varepsilon}{\partial\varepsilon} =& \left(\frac{\partial \boldsymbol{w}}{\partial \boldsymbol{X}^0} + \frac{\partial \boldsymbol{W}}{\partial \boldsymbol{X}^0} \right) \boldsymbol{\chi}^{\varepsilon-1} \\
& - \left(\mathbb{1} + \frac{\partial \boldsymbol{u}^\varepsilon}{\partial \boldsymbol{X}^0} + \frac{\partial \boldsymbol{U}^\varepsilon}{\partial \boldsymbol{X}^0} \right) \boldsymbol{\chi}^{\varepsilon-1} \frac{\partial \boldsymbol{W}}{\partial \boldsymbol{X}^0} \boldsymbol{\chi}^{\varepsilon-1} \\
=& \left(\frac{\partial \boldsymbol{w}}{\partial \boldsymbol{X}^0} + \frac{\partial \boldsymbol{W}}{\partial \boldsymbol{X}^0} \right) \boldsymbol{\chi}^{\varepsilon-1} - \boldsymbol{F}^\varepsilon \frac{\partial \boldsymbol{W}}{\partial \boldsymbol{X}^0} \boldsymbol{\chi}^{\varepsilon-1} \\
=& \left[\frac{\partial \boldsymbol{w}}{\partial \boldsymbol{X}^0} + (\mathbb{1} - \boldsymbol{F}^\varepsilon) \frac{\partial \boldsymbol{W}}{\partial \boldsymbol{X}^0} \right] \boldsymbol{\chi}^{\varepsilon-1}
\end{aligned}
\tag{A.2}
$$

Now consider the first variation of $\det \boldsymbol{\chi}$, recalling equation (2.3):

$$\begin{aligned}\frac{d \det \boldsymbol{\chi}^{\varepsilon}}{d\varepsilon} &= \frac{\partial \det \boldsymbol{\chi}^{\varepsilon}}{\partial \boldsymbol{\chi}^{\varepsilon}} : \frac{d\boldsymbol{\chi}^{\varepsilon}}{d\varepsilon} \\ &= \det \boldsymbol{\chi}^{\varepsilon} \boldsymbol{\chi}^{\varepsilon - T} : \frac{\partial \boldsymbol{W}}{\partial \boldsymbol{X}^0} \\ &= \mathbb{1} : \left(\frac{\partial \boldsymbol{W}}{\partial \boldsymbol{X}^0} \boldsymbol{\chi}^{\varepsilon - 1} \right) \det \boldsymbol{\chi}^{\varepsilon} \end{aligned} \tag{A.3}$$

Substituting (A.2) and (A.3) into (A.1) and using the relations $\partial\psi/\partial \boldsymbol{F} = \boldsymbol{P}$, $d\boldsymbol{\kappa}^{\varepsilon}/d\varepsilon = \boldsymbol{W}$, and $d\boldsymbol{u}^{\varepsilon}/d\varepsilon = \boldsymbol{w}$ gives

$$\begin{aligned} 0 = &\int_{\Omega_0} \left[\boldsymbol{P} : \left[\frac{\partial \boldsymbol{w}}{\partial \boldsymbol{X}^0} \boldsymbol{\chi}^{-1} + (\mathbb{1} - \boldsymbol{F}) \frac{\partial \boldsymbol{W}}{\partial \boldsymbol{X}^0} \boldsymbol{\chi}^{-1} \right] + \frac{\partial \psi}{\partial \boldsymbol{\kappa}} \cdot \boldsymbol{W} \right] \det \boldsymbol{\chi} \, \mathrm{d}V_0 \\ &+ \int_{\Omega_0} (\psi - \cdot \boldsymbol{u}) \mathbb{1} : \left(\frac{\partial \boldsymbol{W}}{\partial \boldsymbol{X^0}} \boldsymbol{\chi^{-1}} \right) \det \boldsymbol{\chi} \, \mathrm{d}\mathbf{V_0} \\ &- \int_{\Omega_0} \left(\cdot \boldsymbol{w} + \boldsymbol{u} \cdot \frac{\partial}{\partial \boldsymbol{\kappa}} \cdot \boldsymbol{W} \right) \det \boldsymbol{\chi} \, \mathrm{d}V_0 - \int_{\partial \Omega^{\mathrm{S}}_{T_0}} \boldsymbol{T}^0 \cdot \boldsymbol{w} \, \mathrm{d}S_0 \end{aligned} \tag{A.4}$$

Terms are grouped according to $\boldsymbol{w}$, $\boldsymbol{W}$, and their gradients.

$$\begin{aligned} 0 = &\int_{\Omega_0} \boldsymbol{P} : \left(\frac{\partial \boldsymbol{w}}{\partial \boldsymbol{X}^0} \boldsymbol{\chi}^{-1} \right) \det \boldsymbol{\chi} \, \mathrm{d}V_0 \\ &- \int_{\Omega_0} (\cdot \boldsymbol{w}) \det \boldsymbol{\chi} \, \mathrm{d}\mathbf{V_0} - \int_{\partial \boldsymbol{\Omega}^{\mathrm{S}}_{\mathbf{T_0}}} \boldsymbol{T^0} \cdot \boldsymbol{w} \, \mathrm{d}\mathbf{S_0} \\ &+ \int_{\Omega_0} (\boldsymbol{P} - (\cdot \boldsymbol{u}) \, \mathbb{1} + \boldsymbol{\mathcal{E}}) : \left(\frac{\partial \boldsymbol{W}}{\partial \boldsymbol{X}^0} \boldsymbol{\chi}^{-1} \right) \det \boldsymbol{\chi} \, \mathrm{d}V_0 \\ &+ \int_{\Omega_0} \left(\frac{\partial \psi}{\partial \boldsymbol{\kappa}} - \left(\frac{\partial}{\partial \boldsymbol{\kappa}} \right)^T \boldsymbol{u} \right) \cdot \boldsymbol{W} \det \boldsymbol{\chi} \, \mathrm{d}V_0 \end{aligned} \tag{A.5}$$

Note that $\boldsymbol{\mathcal{E}} := \psi \mathbb{1} - \boldsymbol{F}^T \boldsymbol{P}$ is the Eshelby stress tensor. The integrals are now

converted back to the Ω domain.

$$
\begin{aligned}
0 = & \int_{\Omega} \boldsymbol{P} : \frac{\partial \boldsymbol{w}}{\partial \boldsymbol{X}} \, \mathrm{d}V \\
& - \int_{\Omega} (\cdot \boldsymbol{w}) \, \mathrm{d}\mathbf{V} - \int_{\partial \boldsymbol{\Omega}_{\mathbf{T}}^{\mathrm{S}}} \boldsymbol{T} \cdot \boldsymbol{w} \, \mathrm{d}\mathbf{S} \\
& + \int_{\Omega} (\boldsymbol{P} - (\cdot \boldsymbol{u}) \, \mathbb{1} + \boldsymbol{\mathcal{E}}) : \frac{\partial \boldsymbol{W}}{\partial \boldsymbol{X}} \, \mathrm{d}V \\
& + \int_{\Omega} \left(\frac{\partial \psi}{\partial \boldsymbol{X}} - \left(\frac{\partial}{\partial \boldsymbol{X}} \right)^{T} \boldsymbol{u} \right) \cdot \boldsymbol{W} \, \mathrm{d}V
\end{aligned} \tag{A.6}
$$

Integration by parts is now performed, recognizing the potential jump terms at the interface of phases α and β. The operator $\nabla \cdot$ is used here to refer to the divergence with respect to $\boldsymbol{X}$. Note that $\boldsymbol{N}$ is the unit normal to the boundary of the body, and $\boldsymbol{N}^{\Gamma}$ is the normal to the interface.

$$
\begin{aligned}
0 = & \int_{\Omega} [\nabla \cdot (\boldsymbol{w}^{T} \boldsymbol{P}) - \boldsymbol{w} \cdot (\nabla \cdot \boldsymbol{P} +)] \, \mathrm{d}\mathbf{V} - \int_{\partial \boldsymbol{\Omega}_{\mathbf{T}}^{\mathrm{S}}} \boldsymbol{T} \cdot \boldsymbol{w} \, \mathrm{d}\mathbf{S} \\
& + \int_{\Omega} \nabla \cdot \left[\boldsymbol{W}^{T} (\boldsymbol{P} - (\cdot \boldsymbol{u}) \, \mathbb{1} + \boldsymbol{\mathcal{E}}) \right] \, \mathrm{d}V \\
& - \int_{\Omega} \boldsymbol{W} \cdot \left[\nabla \cdot (\boldsymbol{P} - (\cdot \boldsymbol{u}) \, \mathbb{1} + \boldsymbol{\mathcal{E}}) - \frac{\partial \psi}{\partial \boldsymbol{X}} + \left(\frac{\partial}{\partial \boldsymbol{X}} \right)^{T} \boldsymbol{u} \right] \, \mathrm{d}V \\
= & \int_{\partial \Omega_{T}^{\mathrm{S}}} \boldsymbol{w} \cdot (\boldsymbol{P}\boldsymbol{N} - \boldsymbol{T}) \, \mathrm{d}S - \int_{\Omega} \boldsymbol{w} \cdot (\nabla \cdot \boldsymbol{P} +) \, \mathrm{d}\mathbf{V} \\
& + \int_{\Gamma} [\![\boldsymbol{w} \cdot \boldsymbol{P} \boldsymbol{N}^{\Gamma}]\!] \, \mathrm{d}S + \int_{\Gamma} [\![\boldsymbol{W} \cdot (\boldsymbol{P} - (\cdot \boldsymbol{u}) \, \mathbb{1} + \boldsymbol{\mathcal{E}}) \, \boldsymbol{N}^{\Gamma}]\!] \, \mathrm{d}S \\
& + \int_{\partial \Omega_{T}^{\mathrm{M}}} \boldsymbol{W} \cdot [\boldsymbol{P} - (\cdot \boldsymbol{u}) \, \mathbb{1} + \boldsymbol{\mathcal{E}}] \, \boldsymbol{N} \, \mathrm{d}S \\
& - \int_{\Omega} \boldsymbol{W} \cdot \left[\nabla \cdot (\boldsymbol{P} - (\cdot \boldsymbol{u}) \, \mathbb{1} + \boldsymbol{\mathcal{E}}) - \frac{\partial \psi}{\partial \boldsymbol{X}} + \left(\frac{\partial}{\partial \boldsymbol{X}} \right)^{T} \boldsymbol{u} \right] \, \mathrm{d}V
\end{aligned} \tag{A.7}
$$

By allowing only continuous fields $\boldsymbol{W}$ and $\boldsymbol{w}$, the equation is simplified further.

$$
\begin{aligned}
0 = & \int_{\partial\Omega_T^{\mathrm{S}}} \boldsymbol{w} \cdot (\boldsymbol{P}\boldsymbol{N} - \boldsymbol{T}) \, \mathrm{d}S - \int_{\Omega} \boldsymbol{w} \cdot (\nabla \cdot \boldsymbol{P}+) \, \mathrm{d}\mathbf{V} \\
& + \int_{\Gamma} \boldsymbol{w} \cdot [\![\boldsymbol{P}\boldsymbol{N}^{\Gamma}]\!] \, \mathrm{d}S + \int_{\Gamma} \boldsymbol{W} \cdot [\![\left(\boldsymbol{P} - (\cdot\boldsymbol{u}) \, \mathbb{1} + \boldsymbol{\mathcal{E}} \right) \boldsymbol{N}^{\Gamma}]\!] \, \mathrm{d}S \\
& + \int_{\partial\Omega_T^{\mathrm{M}}} \boldsymbol{W} \cdot \left[\boldsymbol{P} - (\cdot\boldsymbol{u}) \, \mathbb{1} + \boldsymbol{\mathcal{E}} \right] \boldsymbol{N} \, \mathrm{d}S \\
& - \int_{\Omega} \boldsymbol{W} \cdot \left[\nabla \cdot (\boldsymbol{P} - (\cdot\boldsymbol{u}) \, \mathbb{1} + \boldsymbol{\mathcal{E}}) - \frac{\partial \psi}{\partial \boldsymbol{X}} + \left(\frac{\partial}{\partial \boldsymbol{X}} \right)^{T} \boldsymbol{u} \right] \mathrm{d}V
\end{aligned}
\tag{A.8}
$$

The corresponding strong form for the sharp interface problem consists of the two following sets of equations. The second set of equations (A.9d - A.9f) has been simplified under the assumption that the first set of equations (A.9a - A.9c) is satisfied.

$$\boldsymbol{P}\boldsymbol{N} - \boldsymbol{T} = 0 \text{ on } \partial\Omega_T^{\mathrm{S}} \tag{A.9a}$$

$$[\![\boldsymbol{P}\boldsymbol{N}^{\Gamma}]\!] = 0 \text{ on } \Gamma \tag{A.9b}$$

$$\nabla \cdot \boldsymbol{P}+ = 0 \text{ in } \Omega \tag{A.9c}$$

$$(\boldsymbol{\mathcal{E}} + \boldsymbol{P} - (\cdot\boldsymbol{u})\mathbb{1}) \, \boldsymbol{N} = 0 \text{ on } \partial\Omega_T^{\mathrm{M}} \tag{A.9d}$$

$$[\![\left(\boldsymbol{\mathcal{E}} - (\cdot\boldsymbol{u})\mathbb{1} \right) \boldsymbol{N}^{\Gamma}]\!] = 0 \text{ on } \Gamma \tag{A.9e}$$

$$\nabla \cdot \boldsymbol{\mathcal{E}} - \frac{\partial \psi}{\partial \boldsymbol{X}} - \boldsymbol{F}^{T} = 0 \text{ in } \Omega \tag{A.9f}$$

Consider the following simplification of equation (A.9f):

$$
\begin{aligned}
0 &= \nabla \cdot (\boldsymbol{\mathcal{E}} - (\cdot\boldsymbol{u})\mathbb{1}) - -\frac{\partial \psi}{\partial \boldsymbol{X}} + \left(\frac{\partial}{\partial \boldsymbol{X}} \right)^{\mathbf{T}} \boldsymbol{u} \\
&= \nabla \cdot \boldsymbol{\mathcal{E}} - \left(\frac{\partial}{\partial \boldsymbol{X}} \right)^{T} \boldsymbol{u} - \left(\frac{\partial \boldsymbol{u}}{\partial \boldsymbol{X}} + \mathbb{1} \right)^{T} - \frac{\partial \psi}{\partial \boldsymbol{X}} + \left(\frac{\partial}{\partial \boldsymbol{X}} \right)^{\mathbf{T}} \boldsymbol{u} \\
&= \nabla \cdot \boldsymbol{\mathcal{E}} - \frac{\partial \psi}{\partial \boldsymbol{X}} - \boldsymbol{F}^{T}
\end{aligned}
\tag{A.10}
$$

APPENDIX B

First variation of constant interfacial energy

The mean curvature-driven term in Equation (2.19a) and the additional boundary condition (2.19b) can be obtained by considering pure curvature-driven motion. The ojbective is to minimize the interface energy

$$\Pi^{\Gamma} = \int_{\Gamma} \psi^{\Gamma} \, \mathrm{d}S \tag{B.1}$$

with respect to the interface Γ, where ψ^{Γ} is a constant. To do so, find Γ such that the first variation of Π is zero. The interface Γ is defined by the parameterization $\boldsymbol{r}(u, v)$, where u and v are defined over the domain T. The surface $\boldsymbol{r}(u, v)$ is varied by $\varepsilon \boldsymbol{W}$ to allow variations of the interface location. To avoid integration over a varying surface, a change of variables is performed. Let Γ^0 be a surface defined by the parameterization $\boldsymbol{r}^0(u, v)$ where $\boldsymbol{r}^0$, $\boldsymbol{r}$, and $\boldsymbol{r}^{\varepsilon}$ are related as follows:

$$\boldsymbol{r}(u, v) = \boldsymbol{r}^0(u, v) + \boldsymbol{U}(\boldsymbol{r}^0(u, v)) \tag{B.2}$$

$$\boldsymbol{r}^{\varepsilon}(u, v) = \boldsymbol{r}^0(u, v) + \boldsymbol{U}(\boldsymbol{r}^0(u, v)) + \varepsilon \boldsymbol{W}(\boldsymbol{r}^0(u, v)) \tag{B.3}$$

Then it can be written

$$\int_{\Gamma} \psi^{\Gamma} \, \mathrm{d}S = \int_{T} \psi^{\Gamma} \, |\boldsymbol{r}_{,u} \times \boldsymbol{r}_{,v}| \, \mathrm{d}u\mathrm{d}v \tag{B.4}$$

The first variation is

$$\begin{aligned}
\frac{\mathrm{d}}{\mathrm{d}\varepsilon}\Pi^{\Gamma_\varepsilon}\big|_{\varepsilon=0} &= \frac{\mathrm{d}}{\mathrm{d}\varepsilon}\left\{\int_{\Gamma^\varepsilon} \psi^{\Gamma} \, \mathrm{d}S^{\varepsilon}\right\}\Big|_{\varepsilon=0} \\
&= \frac{\mathrm{d}}{\mathrm{d}\varepsilon}\left\{\int_{T} \psi^{\Gamma} \left|\boldsymbol{r}^{\varepsilon}_{,u} \times \boldsymbol{r}^{\varepsilon}_{,v}\right| \, \mathrm{d}u\mathrm{d}v\right\}\Big|_{\varepsilon=0} \\
&= \int_{T} \psi^{\Gamma} \frac{\frac{\mathrm{d}}{\mathrm{d}\varepsilon}\left(\boldsymbol{r}^{\varepsilon}_{,u} \times \boldsymbol{r}^{\varepsilon}_{,v}\right)\big|_{\varepsilon=0} \cdot (\boldsymbol{r}_{,u} \times \boldsymbol{r}_{,v})}{|\boldsymbol{r}_{,u} \times \boldsymbol{r}_{,v}|} \, \mathrm{d}u\mathrm{d}v \\
&= \int_{T} \psi^{\Gamma} \frac{\mathrm{d}}{\mathrm{d}\varepsilon}\left(\boldsymbol{r}^{\varepsilon}_{,u} \times \boldsymbol{r}^{\varepsilon}_{,v}\right)\big|_{\varepsilon=0} \cdot \boldsymbol{N}^{\Gamma} \, \mathrm{d}u\mathrm{d}v
\end{aligned} \tag{B.5}$$

From equation (B.3), comes the result

$$\tfrac{\mathrm{d}}{\mathrm{d}\varepsilon}\boldsymbol{r}^{\varepsilon}\big|_{\varepsilon=0} = \boldsymbol{W} \tag{B.6}$$

Substituting this result gives

$$\begin{aligned}
\frac{\mathrm{d}}{\mathrm{d}\varepsilon}\Pi^{\Gamma_\varepsilon}\big|_{\varepsilon=0} &= \int_{T} \psi^{\Gamma}(\boldsymbol{W}_{,u} \times \boldsymbol{r}_{,v} + \boldsymbol{r}_{,u} \times \boldsymbol{W}_{,v}) \cdot \boldsymbol{N}^{\Gamma} \, \mathrm{d}u\mathrm{d}v \\
&= \int_{T} \psi^{\Gamma}[((\nabla \boldsymbol{W})\boldsymbol{r}_{,u}) \times \boldsymbol{r}_{,v} - ((\nabla \boldsymbol{W})\boldsymbol{r}_{,v}) \times \boldsymbol{r}_{,u}] \cdot \boldsymbol{N}^{\Gamma} \, \mathrm{d}u\mathrm{d}v
\end{aligned} \tag{B.7}$$

Continuing in coordinate notation for clarity, this becomes

$$\begin{aligned}\frac{\mathrm{d}}{\mathrm{d}\varepsilon}\Pi^{\Gamma_\varepsilon}\big|_{\varepsilon=0} &= \int_T \psi^\Gamma \partial_\ell(W_j)\left(r_{\ell,u}r_{k,v} - r_{\ell,v}r_{k,u}\right)\varepsilon_{ijk}N_i^\Gamma \,\mathrm{d}u\mathrm{d}v \\ &= \int_T \psi^\Gamma \partial_\ell(W_j)\left(\delta_{\ell m}\delta_{kn} - \delta_{\ell n}\delta_{km}\right) r_{m,u}r_{n,v}\varepsilon_{ijk}N_i^\Gamma \,\mathrm{d}u\mathrm{d}v \\ &= \int_T \psi^\Gamma \partial_\ell(W_j)\varepsilon_{p\ell k}\varepsilon_{pmn}r_{m,u}r_{n,v}\varepsilon_{ijk}N_i^\Gamma \,\mathrm{d}u\mathrm{d}v \end{aligned} \tag{B.8}$$

Note that

$$\begin{aligned}\varepsilon_{pmn}r_{m,u}r_{n,v} &= \left(\boldsymbol{r}_{,u}\times\boldsymbol{r}_{,v}\right)_p \\ &= N_p^\Gamma|\boldsymbol{r}_u\times\boldsymbol{r}_v|\end{aligned} \tag{B.9}$$

Using this result lets us write the integral over Γ.

$$\begin{aligned}\frac{\mathrm{d}}{\mathrm{d}\varepsilon}\Pi^{\Gamma_\varepsilon}\big|_{\varepsilon=0} &= \int_T \psi^\Gamma \partial_\ell(W_j)\varepsilon_{p\ell k}\varepsilon_{ijk}N_i^\Gamma N_p^\Gamma|\boldsymbol{r}_u\times\boldsymbol{r}_v|\,\mathrm{d}u\mathrm{d}v \\ &= \int_\Gamma \psi^\Gamma \partial_\ell(W_j)\varepsilon_{p\ell k}\varepsilon_{ijk}N_i^\Gamma N_p^\Gamma \,\mathrm{d}S \\ &= \int_\Gamma \psi^\Gamma \left[\partial_\ell(N_i^\Gamma W_j\varepsilon_{ijk}) - \partial_\ell(N_i^\Gamma)W_j\varepsilon_{ijk}\right]\varepsilon_{p\ell k}N_p^\Gamma \,\mathrm{d}S \\ &= \int_\Gamma \psi^\Gamma [\partial_\ell(N_i^\Gamma W_j\varepsilon_{ijk})\varepsilon_{p\ell k}N_p^\Gamma - \partial_\ell(N_i^\Gamma)W_j(\delta_{ip}\delta_{j\ell} - \delta_{i\ell}\delta_{jp})N_p^\Gamma]\,\mathrm{d}S \\ &= \int_\Gamma \psi^\Gamma [\partial_\ell(N_i^\Gamma W_j\varepsilon_{ijk})\varepsilon_{p\ell k}N_p^\Gamma - \partial_j(N_i^\Gamma)N_i^\Gamma W_j + \partial_i(N_i^\Gamma)W_jN_j^\Gamma]\,\mathrm{d}S \end{aligned} \tag{B.10}$$

The term $\partial_j(N_i^\Gamma)N_i^\Gamma$ reduces to zero since $N_i^\Gamma N_i^\Gamma = 1$. The result can be expressed in direct notation.

$$\frac{\mathrm{d}}{\mathrm{d}\varepsilon}\Pi^{\Gamma_\varepsilon}\big|_{\varepsilon=0} = \int_\Gamma \psi^\Gamma \left[\nabla \times \left(\boldsymbol{N}^\Gamma \times \boldsymbol{W}\right) + \left(\nabla \cdot \boldsymbol{N}^\Gamma\right) \boldsymbol{W}\right] \cdot \boldsymbol{N}^\Gamma \,\mathrm{d}S \tag{B.11}$$

Stoke's theorem is applied to the first term and use $\nabla \cdot \boldsymbol{N}^\Gamma = -2H$, where H is the mean curvature.

$$\frac{\mathrm{d}}{\mathrm{d}\varepsilon}\Pi^{\Gamma_\varepsilon}\big|_{\varepsilon=0} = \int_\Gamma -2\psi^\Gamma H \left(\boldsymbol{W} \cdot \boldsymbol{N}^\Gamma\right) \,\mathrm{d}S + \oint_{\partial\Gamma} \psi^\Gamma (\boldsymbol{N}^\Gamma \times \boldsymbol{W}) \cdot \mathrm{d}\boldsymbol{r} \tag{B.12}$$

At equilibrium, the first variation of the total energy is zero, giving the following result.

$$0 = \int_\Gamma -2\psi^\Gamma H \left(\boldsymbol{W} \cdot \boldsymbol{N}^\Gamma\right) \,\mathrm{d}S + \oint_{\partial\Gamma} \psi^\Gamma (\boldsymbol{N}^\Gamma \times \boldsymbol{W}) \cdot \mathrm{d}\boldsymbol{r} \tag{B.13}$$

If there is a full Dirichlet condition on the boundary of Γ then $\boldsymbol{W} = 0$ on $\partial\Gamma$ and the line integral is equal to zero. This gives the result

$$0 = \int_\Gamma -2\psi^\Gamma H \left(\boldsymbol{W} \cdot \boldsymbol{N}^\Gamma\right) \,\mathrm{d}S \tag{B.14}$$

The other possible condition is to allow the boundary of the interface Γ to move within the boundary $\partial\Omega$. This corresponds to $\boldsymbol{U} \cdot \boldsymbol{N} = \boldsymbol{W} \cdot \boldsymbol{N} = 0$, where $\boldsymbol{N}$ is the outward unit normal to $\partial\Omega$. A boundary with this condition is designated as $\partial\Gamma_T$. On such boundaries, $\boldsymbol{W}$ can be expressed using the orthonormal basis $\{\boldsymbol{N}, \boldsymbol{T}^\Gamma, \boldsymbol{N} \times \boldsymbol{T}^\Gamma\}$, where $\boldsymbol{T}^\Gamma$ is the unit tangent vector to $\partial\Gamma$. The result is

$$\boldsymbol{W} = W^T \boldsymbol{T}^\Gamma + W^{N\times T} \left(\boldsymbol{N} \times \boldsymbol{T}^\Gamma\right) \tag{B.15}$$

which satisfies the condition $\boldsymbol{W} \cdot \boldsymbol{N} = 0$. Substitute this expression into the line integral:

$$\oint_{\partial\Gamma} \psi^{\Gamma}(\boldsymbol{N}^{\Gamma} \times \boldsymbol{W}) \cdot \mathrm{d}\boldsymbol{r} = \oint_{\partial\Gamma} \psi^{\Gamma} \left[\boldsymbol{N}^{\Gamma} \times \left[W^{T}\boldsymbol{T}^{\Gamma} + W^{N\times T}\left(\boldsymbol{N} \times \boldsymbol{T}^{\Gamma}\right)\right]\right] \cdot \mathrm{d}\boldsymbol{r} \tag{B.16}$$

Since $\boldsymbol{T}^{\Gamma}$ and $\mathrm{d}\boldsymbol{r}$ have the same orientation, $(\boldsymbol{N}^{\Gamma} \times \boldsymbol{T}^{\Gamma}) \cdot \mathrm{d}\boldsymbol{r} = 0$. The identity $\boldsymbol{a} \times (\boldsymbol{b} \times \boldsymbol{c}) = \boldsymbol{b}(\boldsymbol{a} \cdot \boldsymbol{c}) - \boldsymbol{c}(\boldsymbol{a} \cdot \boldsymbol{b})$ is used.

$$\begin{aligned}\oint_{\partial\Gamma} \psi^{\Gamma}(\boldsymbol{N}^{\Gamma} \times \boldsymbol{W}) \cdot \mathrm{d}\boldsymbol{r} &= \oint_{\partial\Gamma} \psi^{\Gamma} W^{N\times T}\left[\boldsymbol{N}(\boldsymbol{N}^{\Gamma} \cdot \boldsymbol{T}^{\Gamma}) - \boldsymbol{T}^{\Gamma}(\boldsymbol{N}^{\Gamma} \cdot \boldsymbol{N})\right] \cdot \mathrm{d}\boldsymbol{r} \\ &= -\oint_{\partial\Gamma} \psi^{\Gamma} W^{N\times T}(\boldsymbol{N}^{\Gamma} \cdot \boldsymbol{N})\boldsymbol{T}^{\Gamma} \cdot \mathrm{d}\boldsymbol{r}\end{aligned} \tag{B.17}$$

since $\boldsymbol{N}^{\Gamma}$ and $\boldsymbol{T}^{\Gamma}$ are orthogonal. Finally, the relation $W^{N\times T} = \boldsymbol{W} \cdot \left(\boldsymbol{N} \times \boldsymbol{T}^{\Gamma}\right)$ is used and substitute into equation (B.13) to get the complete condition for equilibrium with respect to interfacial energy.

$$0 = \int_{\Gamma} -2\psi^{\Gamma} H \left(\boldsymbol{W} \cdot \boldsymbol{N}^{\Gamma}\right) \mathrm{d}S - \oint_{\partial\Gamma} \psi^{\Gamma} \boldsymbol{W} \cdot \left(\boldsymbol{N} \times \boldsymbol{T}^{\Gamma}\right)(\boldsymbol{N}^{\Gamma} \cdot \boldsymbol{N})\boldsymbol{T}^{\Gamma} \cdot \mathrm{d}\boldsymbol{r} \tag{B.18}$$

Note that $\boldsymbol{T}^{\Gamma} \cdot \mathrm{d}\boldsymbol{r}$ and $\boldsymbol{N} \times \boldsymbol{T}^{\Gamma}$ are always nonzero, so the following strong form is obtained:

$$-2\psi^{\Gamma} H = 0 \text{ in } \Gamma \tag{B.19a}$$

$$\psi^{\Gamma} \boldsymbol{N}^{\Gamma} \cdot \boldsymbol{N} = 0 \text{ on } \partial\Gamma_{T} \tag{B.19b}$$

If the interfacial energy is nonzero, this requires zero mean curvature within the interface and that the interface is perpendicular to the boundary of the body where they meet. If the interfacial energy ψ^{Γ} provides only one contribution to the driving force on Γ, as in Section 2.1.2, then the left hand-side of Equation (B.19a) is the corre-

sponding contribution to Equation (2.19a), while (B.19b) is the additional boundary condition (2.19b).

APPENDIX C

Variational formulation for the diffuse interface problem

Let $\boldsymbol{U}^\varepsilon := \boldsymbol{U} + \varepsilon \boldsymbol{W}$ and $\bar{\boldsymbol{u}}^\varepsilon := \bar{\boldsymbol{u}} + \varepsilon \bar{\boldsymbol{w}}$. Then, recalling equation 2.28, equilibrium requires the following:

$$\begin{aligned}
\frac{\mathrm{d}}{\mathrm{d}\varepsilon}\Pi[\bar{\boldsymbol{u}}^\varepsilon; \boldsymbol{U}^\varepsilon]\bigg|_{\varepsilon=0} &= \frac{\mathrm{d}}{\mathrm{d}\varepsilon}\Bigg\{ \int_{\Omega_0} \psi^{\mathrm{M}}(\boldsymbol{X}^0, \boldsymbol{\chi}^\varepsilon, \nabla^0 \boldsymbol{\chi}^\varepsilon)\, \mathrm{d}V_0 \\
&\qquad + \int_{\Omega_0} \psi^{\mathrm{S}}(\boldsymbol{X}^\varepsilon, \boldsymbol{F}^\varepsilon, \boldsymbol{\chi}^\varepsilon) \det \boldsymbol{\chi}^\varepsilon \, \mathrm{d}V_0 \\
&\qquad - \int_{\Omega_0} \boldsymbol{f}^0 \cdot \bar{\boldsymbol{u}}^\varepsilon \, \mathrm{d}V_0 - \int_{\partial\Omega^{\mathrm{S}}_{T_0}} \boldsymbol{T}^0 \cdot \bar{\boldsymbol{u}}^\varepsilon \, \mathrm{d}S_0 \Bigg\}\Bigg|_{\varepsilon=0} \\
&= 0
\end{aligned} \tag{C.1}$$

Then

$$
\begin{aligned}
0 = &\int_{\Omega_0} \left(\frac{\partial \psi^{\mathrm{M}}}{\partial \boldsymbol{\chi}} : \frac{\mathrm{d}\boldsymbol{\chi}^{\varepsilon}}{\mathrm{d}\varepsilon}\bigg|_{\varepsilon=0} + \frac{\partial \psi^{\mathrm{M}}}{\partial \nabla^0 \boldsymbol{\chi}} \vdots \frac{\mathrm{d}\nabla^0 \boldsymbol{\chi}^{\varepsilon}}{\mathrm{d}\varepsilon}\bigg|_{\varepsilon=0} \right) \mathrm{d}V_0 \\
&+ \int_{\Omega_0} \left(\frac{\partial \psi^{\mathrm{S}}}{\partial \boldsymbol{X}} \cdot \frac{d\boldsymbol{X}^{\varepsilon}}{d\varepsilon}\bigg|_{\varepsilon=0} + \frac{\partial \psi^{\mathrm{S}}}{\partial \boldsymbol{F}} : \frac{d\boldsymbol{F}^{\varepsilon}}{d\varepsilon}\bigg|_{\varepsilon=0} \right) \det \boldsymbol{\chi} \, \mathrm{d}V_0 \\
&+ \int_{\Omega_0} \left(\frac{\partial \psi^{\mathrm{S}}}{\partial \boldsymbol{\chi}} : \frac{d\boldsymbol{\chi}^{\varepsilon}}{d\varepsilon}\bigg|_{\varepsilon=0} \det \boldsymbol{\chi} + \psi^{\mathrm{S}} \frac{d \det \boldsymbol{\chi}^{\varepsilon}}{d\varepsilon}\bigg|_{\varepsilon=0} \right) \mathrm{d}V_0 \\
&- \int_{\Omega_0} \boldsymbol{f}^0 \cdot \bar{\boldsymbol{w}} \, \mathrm{d}V_0 - \int_{\partial \Omega^{\mathrm{S}}_{T_0}} \boldsymbol{T}^0 \cdot \bar{w} \, \mathrm{d}S_0
\end{aligned} \tag{C.2}
$$

The earlier results concerning the first variations of $\boldsymbol{F}$ and $\det \boldsymbol{\chi}$ are applied. The following terms are also defined $\boldsymbol{B} := \partial \psi^{\mathrm{M}} / \partial \nabla^0 \boldsymbol{\chi}$ and $J_\chi := \det \boldsymbol{\chi}$. The result is

$$
\begin{aligned}
0 = &\int_{\Omega_0} \left(\frac{\partial \psi^{\mathrm{M}}}{\partial \boldsymbol{\chi}} : \nabla^0 \boldsymbol{W} + \boldsymbol{B} \vdots \nabla^0 \nabla^0 \boldsymbol{W} \right) \mathrm{d}V_0 \\
&+ \int_{\Omega_0} \left(\frac{\partial \psi^{\mathrm{S}}}{\partial \boldsymbol{X}} \cdot \boldsymbol{W} + \boldsymbol{P} : \left[\left(\nabla^0 \bar{\boldsymbol{w}} - \boldsymbol{F} \nabla^0 \boldsymbol{W} \right) \boldsymbol{\chi}^{-1} \right] \right) J_\chi \, \mathrm{d}V_0 \\
&+ \int_{\Omega_0} \left[\frac{\partial \psi^{\mathrm{S}}}{\partial \boldsymbol{\chi}} : \nabla^0 \boldsymbol{W} + \psi^{\mathrm{S}} \mathbb{1} : \left(\nabla^0 \boldsymbol{W} \boldsymbol{\chi}^{-1} \right) \right] J_\chi \, \mathrm{d}V_0 \\
&- \int_{\Omega_0} \boldsymbol{f}^0 \cdot \bar{\boldsymbol{w}} \, \mathrm{d}V_0 - \int_{\partial \Omega^{\mathrm{S}}_{T_0}} \boldsymbol{T}^0 \cdot \bar{\boldsymbol{w}} \, \mathrm{d}S_0
\end{aligned} \tag{C.3}
$$

Terms are grouped by $\bar{\boldsymbol{w}}$, $\boldsymbol{W}$, and their gradients and use the Eshelby stress tensor, $\boldsymbol{\mathcal{E}} := \psi^{\mathrm{S}} \mathbb{1} - \boldsymbol{F}^T \boldsymbol{P}$. The resulting weak form is as follows:

$$
\begin{aligned}
0 = &\int_{\Omega_0} \boldsymbol{B} \vdots \nabla^0 \nabla^0 \boldsymbol{W} \, \mathrm{d}V_0 + \int_{\Omega_0} J_\chi \frac{\partial \psi^{\mathrm{S}}}{\partial \boldsymbol{X}} \cdot \boldsymbol{W} \, \mathrm{d}V_0 \\
&+ \int_{\Omega_0} \left[\frac{\partial \psi^{\mathrm{M}}}{\partial \boldsymbol{\chi}} + J_\chi \left(\boldsymbol{\mathcal{E}} \boldsymbol{\chi}^{-T} + \frac{\partial \psi^{\mathrm{S}}}{\partial \boldsymbol{\chi}} \right) \right] : \nabla^0 \boldsymbol{W} \, \mathrm{d}V_0 \\
&+ \int_{\Omega_0} J_\chi \left(\boldsymbol{P} \boldsymbol{\chi}^{-T} \right) : \nabla^0 \bar{\boldsymbol{w}} \, \mathrm{d}V_0 - \int_{\Omega_0} \boldsymbol{f}^0 \cdot \bar{\boldsymbol{w}} \, \mathrm{d}V_0 - \int_{\partial \Omega^{\mathrm{S}}_{T_0}} \boldsymbol{T}^0 \cdot \bar{\boldsymbol{w}} \, \mathrm{d}S_0
\end{aligned} \tag{C.4}
$$

Applying integration by parts gives the following result.

$$
\begin{aligned}
0 = & \int_{\Omega_0} \boldsymbol{B} \dddot{:} \nabla^0 \nabla^0 \boldsymbol{W} \, \mathrm{d}V_0 \\
& + \int_{\partial \Omega^{\mathrm{M}}_{T_0}} \boldsymbol{W} \cdot \left[\frac{\partial \psi^{\mathrm{M}}}{\partial \boldsymbol{\chi}} + J_\chi \left(\boldsymbol{\mathcal{E}} \boldsymbol{\chi}^{-T} + \frac{\partial \psi^{\mathrm{S}}}{\partial \boldsymbol{\chi}} \right) \right] \boldsymbol{N}^0 \, \mathrm{d}S_0 \\
& - \int_{\Omega_0} \boldsymbol{W} \cdot \left(\nabla^0 \cdot \left[\frac{\partial \psi^{\mathrm{M}}}{\partial \boldsymbol{\chi}} + J_\chi \left(\boldsymbol{\mathcal{E}} \boldsymbol{\chi}^{-T} + \frac{\partial \psi^{\mathrm{S}}}{\partial \boldsymbol{\chi}} \right) \right] - J_\chi \frac{\partial \psi^{\mathrm{S}}}{\partial \boldsymbol{X}} \right) \mathrm{d}V_0 \\
& + \int_{\partial \Omega^{\mathrm{S}}_{T_0}} \bar{\boldsymbol{w}} \cdot \left(J_\chi \boldsymbol{P} \boldsymbol{\chi}^{-T} \boldsymbol{N}^0 - \boldsymbol{T}^0 \right) \mathrm{d}S_0 \\
& - \int_{\Omega_0} \bar{\boldsymbol{w}} \cdot \left[\nabla^0 \cdot \left(J_\chi \boldsymbol{P} \boldsymbol{\chi}^{-T} \right) + \boldsymbol{f}^0 \right] \mathrm{d}V_0
\end{aligned} \tag{C.5}
$$

Deriving the strong form from this weak form involves several additional terms due to the dependence on $\nabla^0 \boldsymbol{\chi}$, as described in **(author?)** [85]. The normal and surface gradient operators, ∇^n and ∇^s, are used, where

$$\nabla^n \psi = \nabla^0 \psi \cdot \boldsymbol{N}^0 \tag{C.6}$$

$$\nabla^s \psi = \nabla^0 \psi - (\nabla^n \psi) \, \boldsymbol{N}^0 \tag{C.7}$$

Also, $\boldsymbol{b} = -\nabla^s \boldsymbol{N}^0 = \boldsymbol{b}^T$ is the second fundamental form of the smooth parts of the boundary, $\partial\Omega_0$ and $\boldsymbol{N}^E = \boldsymbol{\Xi} \times \boldsymbol{N}^0$, where $\boldsymbol{\Xi}$ is the unit tangent to the smooth curve $\mathcal{C}_0$ that forms an edge between subsets $\partial\Omega_0^+$ and $\partial\Omega_0^-$of the smooth boundary surfaces $\partial\Omega_0$. If $\boldsymbol{N}^{\mathcal{C}^+}$ is the outward unit normal to $\mathcal{C}_0$ from $\partial\Omega_0^+$ and $\boldsymbol{N}^{\mathcal{C}^-}$ is the outward unit normal to $\mathcal{C}_0$ from $\partial\Omega_0^-$, then the expression $[\![\boldsymbol{B} : \left(\boldsymbol{N}^{\mathcal{C}} \otimes \boldsymbol{N}^0 \right)]\!]^{\mathcal{C}} := \boldsymbol{B} :$

$\left(\boldsymbol{N}^{\mathcal{C}^+} \otimes \boldsymbol{N}^0\right) + \boldsymbol{B} : \left(\boldsymbol{N}^{\mathcal{C}^-} \otimes \boldsymbol{N}^0\right)$ is defined. The following can then be written:

$$\begin{aligned}\int_{\Omega_0} \boldsymbol{B}\vdots\nabla^0\nabla^0\boldsymbol{W}\,\mathrm{d}V_0 = &\int_{\Omega_0} \boldsymbol{W}\cdot\nabla^0\nabla^0\boldsymbol{B}\,\mathrm{d}V_0 - \int_{\partial\Omega_0} \boldsymbol{W}\cdot\boldsymbol{C}\,\mathrm{d}S_0 \\ &+ \int_{\mathcal{C}_0} \boldsymbol{W}\cdot[\![\boldsymbol{B} : (\boldsymbol{N}^{\mathcal{C}}\otimes\boldsymbol{N}^0]\!]^{\mathcal{C}}\,\mathrm{d}L_0 \\ &+ \int_{\partial\Omega_0} \nabla^n\boldsymbol{W}\cdot\boldsymbol{B} : \left(\boldsymbol{N}^0\otimes\boldsymbol{N}^0\right)\,\mathrm{d}S_0 \end{aligned} \tag{C.8}$$

where, using coordinate notation for clarity,

$$\begin{aligned}C_I = &\nabla^n B_{I\gamma\zeta}N^0_\zeta N^0_\gamma + 2\nabla^s_\gamma B_{I\gamma\zeta}N^0_\zeta \\ &+ B_{I\gamma\zeta}\nabla^s_\gamma N^0_\zeta - (b_{\xi\xi}N^0_\gamma N^0_\zeta - b_{\gamma\zeta})B_{I\gamma\zeta}\end{aligned} \tag{C.9}$$

Applying this result to equation C.5 gives the following:

$$\begin{aligned}0 = &\int_{\Omega_0} \boldsymbol{W}\cdot\nabla^0\nabla^0\boldsymbol{B}\,\mathrm{d}V_0 + \int_{\mathcal{C}_0} \boldsymbol{W}\cdot[\![\boldsymbol{B} : \left(\boldsymbol{N}^{\mathcal{C}}\otimes\boldsymbol{N}^0\right)]\!]^{\mathcal{C}}\,dL_0 \\ &- \int_{\partial\Omega^{\mathrm{M}}_{T_0}} \boldsymbol{W}\cdot\boldsymbol{C}\,\mathrm{d}S_0 + \int_{\partial\Omega^{\mathrm{M}}_{T_0}} \nabla^n\boldsymbol{W}\cdot\boldsymbol{B} : \left(\boldsymbol{N}^0\otimes\boldsymbol{N}^0\right)\,\mathrm{d}S_0 \\ &+ \int_{\partial\Omega^{\mathrm{M}}_{T_0}} \boldsymbol{W}\cdot\left[\frac{\partial\psi^{\mathrm{M}}}{\partial\boldsymbol{\chi}} + J_\chi\left(\boldsymbol{\mathcal{E}}\boldsymbol{\chi}^{-T} + \frac{\partial\psi^{\mathrm{S}}}{\partial\boldsymbol{\chi}}\right)\right]\boldsymbol{N}^0\,\mathrm{d}S_0 \\ &- \int_{\Omega_0} \boldsymbol{W}\cdot\left(\nabla^0\cdot\left[\frac{\partial\psi^{\mathrm{M}}}{\partial\boldsymbol{\chi}} + J_\chi\left(\boldsymbol{\mathcal{E}}\boldsymbol{\chi}^{-T} + \frac{\partial\psi^{\mathrm{S}}}{\partial\boldsymbol{\chi}}\right)\right] - J_\chi\frac{\partial\psi^{\mathrm{S}}}{\partial\boldsymbol{X}}\right)\,\mathrm{d}V_0 \\ &+ \int_{\partial\Omega^{\mathrm{S}}_{T_0}} \bar{\boldsymbol{w}}\cdot\left(J_\chi\boldsymbol{P}\boldsymbol{\chi}^{-T}\boldsymbol{N}^0 - \boldsymbol{T}^0\right)\,\mathrm{d}S_0 \\ &- \int_{\Omega_0} \bar{\boldsymbol{w}}\cdot\left[\nabla^0\cdot\left(J_\chi\boldsymbol{P}\boldsymbol{\chi}^{-T}\right) + \boldsymbol{f}^0\right]\,\mathrm{d}V_0\end{aligned} \tag{C.10}$$

Applying the appropriate integration by parts and standard variational arguments

leads to the following strong form.

$$J_\chi \boldsymbol{P}\boldsymbol{\chi}^{-T}\boldsymbol{N}^0 - \boldsymbol{T}^0 = 0 \text{ on } \partial\Omega_{T_0}^{\mathrm{M}} \tag{C.11a}$$

$$\nabla^0 \cdot \left(J_\chi \boldsymbol{P}\boldsymbol{\chi}^{-T}\right) + \boldsymbol{f}^0 = 0 \text{ in } \Omega_0 \tag{C.11b}$$

$$[\![\boldsymbol{B} : \left(\boldsymbol{N}^{\mathcal{C}} \otimes \boldsymbol{N}^0\right)]\!]^{\mathcal{C}} = 0 \text{ on } \mathcal{C}_{T_0}^{\mathrm{M}} \tag{C.11c}$$

$$\boldsymbol{B} : \left(\boldsymbol{N}^0 \otimes \boldsymbol{N}^0\right) = 0 \text{ on } \partial\Omega_{T_0}^{\mathrm{S}} \tag{C.11d}$$

$$\frac{\partial \psi^{\mathrm{M}}}{\partial \boldsymbol{\chi}}\boldsymbol{N}^0 + J_\chi\left(\boldsymbol{\mathcal{E}}\boldsymbol{\chi}^{-T} + \frac{\partial \psi^{\mathrm{S}}}{\partial \boldsymbol{\chi}}\right)\boldsymbol{N}^0 - \boldsymbol{C} = 0 \text{ on } \partial\Omega_{T_0}^{\mathrm{S}} \tag{C.11e}$$

$$\nabla^0 \cdot \left[\frac{\partial \psi^{\mathrm{M}}}{\partial \boldsymbol{\chi}} + J_\chi\left(\boldsymbol{\mathcal{E}}\boldsymbol{\chi}^{-T} + \frac{\partial \psi^{\mathrm{S}}}{\partial \boldsymbol{\chi}}\right)\right] - J_\chi \frac{\partial \psi^{\mathrm{S}}}{\partial \boldsymbol{X}} - \nabla^0\nabla^0 \boldsymbol{B} = 0 \text{ in } \Omega_0 \tag{C.11f}$$

Consider the simplification of equation C.11f, using coordinate notation for clarity:

$$\begin{aligned}
0 &= \left[\frac{\partial \psi^{\mathrm{M}}}{\partial \chi_{I\alpha}} + J_\chi\left(\mathcal{E}_{IJ}\chi^{-1}_{\alpha J} + \frac{\partial \psi^{\mathrm{S}}}{\partial \chi_{I\alpha}}\right)\right]_{,\alpha} - J_\chi \frac{\partial \psi^{\mathrm{S}}}{\partial X_I} - B_{I\alpha\beta,\alpha\beta} \\
&= \left(\frac{\partial \psi^{\mathrm{M}}}{\partial \chi_{I\alpha}}\right)_{,\alpha} + \left(J_\chi \psi^{\mathrm{S}} \chi^{-1}_{\alpha I}\right)_{,\alpha} - \left(J_\chi F_{iI} P_{iJ} \chi^{-1}_{\alpha J}\right)_{,\alpha} + \left(J_\chi \frac{\partial \psi^{\mathrm{S}}}{\partial \chi_{I\alpha}}\right)_{,\alpha} \\
&\quad - J_\chi \frac{\partial \psi^{\mathrm{S}}}{\partial X_I} - B_{I\alpha\beta,\alpha\beta} \\
&= \left(\frac{\partial \psi^{\mathrm{M}}}{\partial \chi_{I\alpha}}\right)_{,\alpha} + J_\chi\left(\frac{\partial \psi^{\mathrm{S}}}{\partial X^0_\alpha} + \frac{\partial \psi^{\mathrm{S}}}{\partial F_{iJ}} F_{iJ,\alpha}\right)\chi^{-1}_{\alpha I} + \psi^{\mathrm{S}}\left(J_\chi \chi^{-1}_{\alpha I}\right)_{,\alpha} \\
&\quad - F_{iI,\alpha}\left(J_\chi P_{iJ}\chi^{-1}_{\alpha J}\right) - F_{iI}\left(J_\chi P_{iJ}\chi^{-1}_{\alpha J}\right)_{,\alpha} + \left(J_\chi \frac{\partial \psi^{\mathrm{S}}}{\partial \chi_{I\alpha}}\right)_{,\alpha} - J_\chi \frac{\partial \psi^{\mathrm{S}}}{\partial X_I} - B_{I\alpha\beta,\alpha\beta} \\
&= \left(\frac{\partial \psi^{\mathrm{M}}}{\partial \chi_{I\alpha}}\right)_{,\alpha} + J_\chi P_{iJ} F_{iJ,I} + \psi^{\mathrm{S}}\left(J_\chi \chi^{-1}_{\alpha I}\right)_{,\alpha} \\
&\quad - J_\chi F_{iI,J} P_{iJ} - F_{iI}\left(J_\chi P_{iJ}\chi^{-1}_{I\alpha}\right)_{,\alpha} + \left(J_\chi \frac{\partial \psi^{\mathrm{S}}}{\partial \chi_{I\alpha}}\right)_{,\alpha} - B_{I\alpha\beta,\alpha\beta}
\end{aligned} \tag{C.12}$$

Consider the term $\left(J_\chi \chi_{\alpha I}^{-1}\right)_{,\alpha}$ and use the relation $\chi_{J\beta,\alpha} = \chi_{J\alpha,\beta}$

$$\begin{aligned}
\left(J_\chi \chi_{\alpha I}^{-1}\right)_{,\alpha} &= \frac{\partial\left(J_\chi \chi_{\alpha I}^{-1}\right)}{\partial \chi_{J\beta}} \chi_{J\beta,\alpha} \\
&= \left(\frac{\partial J_\chi}{\partial \chi_{J\beta}} \chi_{\alpha I}^{-1} + J_\chi \frac{\partial \chi_{\alpha I}^{-1}}{\partial \chi_{J\beta}}\right) \chi_{J\beta,\alpha} \\
&= \left(J_\chi \chi_{\beta J}^{-1} \chi_{\alpha I}^{-1} - J_\chi \chi_{\alpha J}^{-1} \chi_{\beta I}^{-1}\right) \chi_{J\beta,\alpha} \\
&= 0
\end{aligned} \tag{C.13}$$

Substitute this result, the relation $F_{iI,J} = F_{iJ,I}$, and equation C.11b into equation C.12. This gives

$$\left(\frac{\partial \psi^{\mathrm{M}}}{\partial \chi_{I\alpha}} + J_\chi \frac{\partial \psi^{\mathrm{S}}}{\partial \chi_{I\alpha}}\right)_{,\alpha} + F_{iI} f_i^0 - B_{I\alpha\beta,\alpha\beta} = 0 \tag{C.14}$$

or, in direct notation,

$$\nabla^0 \cdot \left(\frac{\partial \psi^{\mathrm{M}}}{\partial \boldsymbol{\chi}} + J_\chi \frac{\partial \psi^{\mathrm{S}}}{\partial \boldsymbol{\chi}}\right) + \boldsymbol{F}^T \boldsymbol{f}^0 - \nabla^0 \nabla^0 \boldsymbol{B} = 0 \tag{C.15}$$

BIBLIOGRAPHY

BIBLIOGRAPHY

[1] Gregory H. Teichert, N.S. Harsha Gunda, Shiva Rudraraju, Anirudh Raju Natarajan, Brian Puchala, Krishna Garikipati, and Anton Van der Ven. A comparison of redlich-kister polynomial and cubic spline representations of the chemical potential in phase field computations. *Computational Materials Science*, 128:127 – 139, 2017.

[2] Ellen L. S. Solomon, Timothy Chan, Andrew Chen, Benjamin Uttal-Veroff, and Emmanuelle A. Marquis. *Aging Behavior of Mg Alloys Containing Nd and Y*, pages 349–352. Springer International Publishing, Cham, 2017.

[3] Anirudh Raju Natarajan and Anton Van der Ven. A unified description of ordering in {HCP} mg-re alloys. *Acta Materialia*, 124:620 – 632, 2017.

[4] Y.Z. Ji, A. Issa, T.W. Heo, J.E. Saal, C. Wolverton, and L.-Q. Chen. Predicting β' precipitate morphology and evolution in MgRE alloys using a combination of first-principles calculations and phase-field modeling. *Acta Materialia*, 76:259 – 271, 2014.

[5] H. Liu, Y. Gao, J.Z. Liu, Y.M. Zhu, Y. Wang, and J.F. Nie. A simulation study of the shape of β' precipitates in MgY and MgGd alloys. *Acta Materialia*, 61(2):453 – 466, 2013.

[6] Cuiping Guo, Zhenmin Du, and Changrong Li. A thermodynamic description of the gdmgy system. *Calphad*, 31(1):75 – 88, 2007.

[7] G. B. Olson and W. Owen, editors. *Martensite : a tribute to Morris Cohen*. ASM International, Materials Park, OH, 1992.

[8] K. Otsuka and C. M. Wayman, editors. *Shape Memory Materials*. Cambridge Univ. Press, Cambridge, 1998.

[9] R.D. James and K.F. Hane. Martensitic transformations and shape-memory materials. *Acta Materialia*, 48(1):197 – 222, 2000.

[10] K. Bhattacharya, S. Conti, G. Zanzotto, and J. Zimmer. Crystal symmetry and the reversibility of martensitic transformations. *Nature*, 428:55–59, 2004.

[11] G.B. Olson. Advances in theory: Martensite by design. *Materials Science and Engineering: A*, 438440:48 – 54, 2006. Proceedings of the International Conference on Martensitic Transformations.

[12] S. Rudraraju, A. Van der Ven, and K. Garikipati. Mechanochemical spinodal decomposition: a phenomenological theory of phase transformations in multi-component, crystalline solids. *npj Computational Materials*, 2, 2016.

[13] M.P Casaletto, G.M Ingo, S Kaciulis, G Mattogno, L Pandolfi, and G Scavia. Surface studies of in vitro biocompatibility of titanium oxide coatings. *Applied Surface Science*, 172(1):167 – 177, 2001.

[14] Y.X Leng, N Huang, P Yang, J.Y Chen, H Sun, J Wang, G.J Wan, X.B Tian, R.K.Y Fu, L.P Wang, and P.K Chu. Structure and properties of biomedical tio2 films synthesized by dual plasma deposition. *Surface and Coatings Technology*, 156(1):295 – 300, 2002. Proceedings of the VIth International Conference on Plasma-Based Ion Implantation.

[15] A. Van der Ven, B. Puchala, and T. Nagase. Ti and Zr based metal-air batteries. *Journal of Power Sources*, 242:400–404, 2013.

[16] H. Dong and X. Y. Li. Oxygen boost diffusion for the deep-case hardening of titanium alloys. *Materials Science and Engineering A*, 280:303–310, 2000.

[17] C. C. Ting, S. Y. Chen, and D. M. Liu. Structural evolution and optical properties of TiO_2 thin films prepared by thermal oxidation of sputtered Ti films. *ournal of Applied Physics*, 88:4628, 2000.

[18] D. S. R. Krishna and Y. Sun. Effect of thermal oxidation conditions on tribological behavior of titanium films on 316L stainless steel. *Surface & Coating Technology*, 198:447–453, 2005.

[19] M. Jamesh, T. S. N. S Narayanan, and P. K. Chu. Thermal oxidation of titanium: Evaluation of corrosion resistance as a function of cooling rate. *Materials Chemistry and Physics*, 138:565, 2013.

[20] C. H. Kao, S. W. Yeh, H. L. Huang, D. Gan, and P. Shen. Study of the TiO to anatase transformation by thermal oxidation of Ti film in air. *Journal of Physical Chemistry C*, 115:5648–5656, 2011.

[21] T. Okazumi, K. Ueda, K. Tajima, N. Umetsu, and T. Narushima. Anatase formation on titanium by two-step thermal oxidation. *Journal of Materials Science*, 46:2998, 2011.

[22] Y. L. Chung, D. S. Gan, K. L. Ou, and S. Y. Chiou. Formation of anatase and TiO from Ti thin film after anodic treatment and thermal annealing. *Journal of the Electrochemical Society*, 158:C319, 2011.

[23] Y. L. Chung, D. S. Gan, and K. L. Ou. The Ti to TiO and TiO to anatase transformations induced by anodizing and annealing treatments of Ti thin film. *Journal of The Electrochemical Society*, 159:C133, 2012.

[24] H. Dong, A. Bloyce, P. H. Morton, and T. Bell. Surface engineering to improve tribological performance of Ti-6Al-4V. *Surface Engineering*, 13(5):402–406, 1997.

[25] M. Cancarevic, M. Zinkevich, and F. Aldinger. Thermodynamic description of the TiO system using the associate model for the liquid phase. *Calphad*, 31(3):330 – 342, 2007.

[26] C Deacon, M. H. Loretto, and R. E. Smallman. Behaviour of vacancies during oxidation. *Materials Science and Technology*, 1(5):344–350, 1985.

[27] J. L. González-carrasco, V. Guttmann, and H. Fattori. Void formation during oxidation of the ods alloy ma 6000. *Metallurgical and Materials Transactions A*, 26(4):915–924, 1995.

[28] I. J. Polmear. Magnesium alloys and applications. *Materials Science and Technology*, 10(1):1–16, 1994.

[29] Jian-Feng Nie. Precipitation and hardening in magnesium alloys. *Metallurgical and Materials Transactions A*, 43(11):3891–3939, 2012.

[30] Jian-Feng Nie. 20 - Physical metallurgy of light alloys. In David E. Laughlin and Kazuhiro Hono, editors, *Physical Metallurgy (Fifth Edition)*, pages 2009 – 2156. Elsevier, Oxford, fifth edition, 2014.

[31] Anirudh Raju Natarajan, Ellen L.S. Solomon, Brian Puchala, Emmanuelle A. Marquis, and Anton Van der Ven. On the early stages of precipitation in dilute MgNd alloys. *Acta Materialia*, 108:367 – 379, 2016.

[32] M.E. Thompson and P.W. Voorhees. Equilibrium particle morphologies in elastically stressed coherent solids. *Acta Materialia*, 47(3):983 – 996, 1999.

[33] S. Mller, C. Wolverton, L.-W. Wang, and A. Zunger. Prediction of alloy precipitate shapes from first principles. *EPL (Europhysics Letters)*, 55(1):33, 2001.

[34] Y. Gao, H. Liu, R. Shi, N. Zhou, Z. Xu, Y.M. Zhu, J.F. Nie, and Y. Wang. Simulation study of precipitation in an mgynd alloy. *Acta Materialia*, 60(12):4819 – 4832, 2012.

[35] Y.Z. Ji, A. Issa, T.W. Heo, J.E. Saal, C. Wolverton, and L.-Q. Chen. Predicting β' precipitate morphology and evolution in MgRE alloys using a combination of first-principles calculations and phase-field modeling. *Acta Materialia*, 76:259 – 271, 2014.

[36] H. Liu, W.F. Xu, L.M. Peng, W.J. Ding, and J.F. Nie. A simulation study of the distribution of β' precipitates in a crept Mg-Gd-Zr alloy. *Computational Materials Science*, 130:152 – 164, 2017.

[37] Stephen DeWitt, Ellen L.S. Solomon, Anirudh Raju Natarajan, Vicente Araullo-Peters, Shiva Rudraraju, Larry K. Aagesen, Brian Puchala, Emmanuelle A. Marquis, Anton van der Ven, Katsuyo Thornton, and John E. Allison. Misfit-driven β''' precipitate composition and morphology in Mg-Nd alloys. *Acta Materialia*, pages –, 2017.

[38] P. Hohenberg and W. Kohn. Inhomogeneous electron gas. *Phys. Rev.*, 136:B864–B871, Nov 1964.

[39] W. Kohn and L. J. Sham. Self-consistent equations including exchange and correlation effects. *Phys. Rev.*, 140:A1133–A1138, Nov 1965.

[40] J. M. Sanchez, F. Ducastelle, and D. Gratias. Generalized cluster description of multicomponent systems. *Physica A*, 128:334–350, 1984.

[41] D. De Fontaine. Cluster approach to order-disorder transformations in alloys. volume 47 of *Solid State Physics*, pages 33 – 176. Academic Press, 1994.

[42] A. Van der Ven, M. K.. Aydinol, G. Ceder, G. Kresse, and J. Hafner. First-principles investigation of phase stability in Li_xCoO_2. *Phys. Rev. B*, 58:2975–2987, 1998.

[43] A. van de Walle and M. Asta. Self-driven lattice-model Monte Carlo simulations of alloy thermodynamic properties and phase diagrams. *Modelling and Simulation in Materials Science and Engineering*, 10:521–538, 2002.

[44] Vikram Gavini, Kaushik Bhattacharya, and Michael Ortiz. Quasi-continuum orbital-free density-functional theory: A route to multi-million atom non-periodic dft calculation. *Journal of the Mechanics and Physics of Solids*, 55(4):697 – 718, 2007.

[45] A. Van der Ven, J. C. Thomas, Q. Xu, and J. Bhattacharya. Linking the electronic structure of solids to their thermodynamic and kinetic properties. *Mathematics and Computers in Simulation*, 80(7):1393–1410, 2010.

[46] B. Puchala and A. Van der Ven. Thermodynamics of the Zr-O system from first-principles calculations. *Phys. Rev. B*, 88:094108, Sep 2013.

[47] M.-H. Chen, B. Puchala, and A. Van Der Ven. High-temperature stability of δ'-ZrO. *Calphad: Computer Coupling of Phase Diagrams and Thermochemistry*, 51:292–298, 2015.

[48] Sambit Das, Mrinal Iyer, and Vikram Gavini. Real-space formulation of orbital-free density functional theory using finite-element discretization: The case for al, mg, and al-mg intermetallics. *Phys. Rev. B*, 92:014104, Jul 2015.

[49] S. M. Allen and J. W. Cahn. A microscopic theory for antiphase boundary motion and its application to antiphase boundary coarsening. *Acta Metallurgica*, 27:10851091, 1979.

[50] S. Osher and J. A. Sethian. Fronts propagating with curvature dependent speed: algorithms based on Hamilton-Jacobi formulation. *J. Comput. Phys.*, 79(12):12–49, 1988.

[51] T. J. Barth and J. A. Sethian. Numerical schemes for the Hamilton-Jacobi and level set equations on triangulated domains. *J. Comput. Phys.*, 145:1–40, 1998.

[52] J. W. Cahn and J. E. Hilliard. Free energy of a nonuniform system. i. interfacial free energy. *J. Chem. Phys.*, 1958.

[53] M. Hillert. *Phase Equilibria, Phase Diagrams and Phase Transformations*. Cambridge University Press, Cambridge, 2nd edition, 2007.

[54] Marvin J. Forray. *Variational Calculus in Science and Engineering*. McGraw-Hill, 1968.

[55] R. Courant and D. Hilbert. *The Calculus of Variations*, pages 164–274. Wiley-VCH Verlag GmbH, 2007.

[56] Luis Miguel Rios and Nikolaos V. Sahinidis. Derivative-free optimization: a review of algorithms and comparison of software implementations. *Journal of Global Optimization*, 56(3):1247–1293, Jul 2013.

[57] Ky Khac Vu, Claudia D'Ambrosio, Youssef Hamadi, and Leo Liberti. Surrogate-based methods for black-box optimization. *International Transactions in Operational Research*, 24(3):393–424, 2017.

[58] Olaf Arndt, Thomas Barth, Bernd Freisleben, and Manfred Grauer. Approximating a finite element model by neural network prediction for facility optimization in groundwater engineering. *European Journal of Operational Research*, 166(3):769 – 781, 2005. Advances in Complex Systems Modeling.

[59] George Kourakos and Aristotelis Mantoglou. Pumping optimization of coastal aquifers based on evolutionary algorithms and surrogate modular neural network models. *Advances in Water Resources*, 32(4):507 – 521, 2009.

[60] Yaochu Jin. Surrogate-assisted evolutionary computation: Recent advances and future challenges. *Swarm and Evolutionary Computation*, 1(2):61 – 70, 2011.

[61] J. D. Eshelby. The force on an elastic singularity. *Philos. Trans. R. Soc. London, Ser. A*, 244(877):87–112, Nov 1951.

[62] C. V. Burton. A theory concerning the constitution of matter. *Philos. Mag.*, 33:191–204, 1892.

[63] J. Larmor. A dynamical theory of the electric and luminiferous medium - iii. relations with material media. *Philos. Trans. R. Soc. London, Ser. A*, 190:205–300, 1897.

[64] M. E. Gurtin. *Configurational forces as basic concepts of continuum physics*. New York: Springer, 2000.

[65] G. A. Maugin. Material forces: Concepts and applications. *Applied Mechanics Reviews*, 48(5):213–245, 1995.

[66] R. Kienzler and G. Herrmann. On the properties of the Eshelby tensor. *Acta Mech.*, 125(1-4):73–91, March 1997.

[67] P. Steinmann. On spatial and material settings of hyperelastostatic crystal defects. *J. Mech. Phys. Solids*, 50:1743–1766, 2002.

[68] G. A. Maugin. *Configurational forces : thermomechanics, physics, mathematics, and numerics*. Boca Raton, FL: Chapman & Hall/CRC, 2011.

[69] DK Vu and P Steinmann. On the spatial and material motion problems in nonlinear electro-elastostatics with consideration of free space. *Mathematics and Mechanics of Solids*, 17(8):803–823, 2012.

[70] R. Mueller and G. A. Maugin. On material forces and finite element discretizations. *Computational Mechanics*, 29(1):52–60, July 2002.

[71] Amit Acharya and Claude Fressengeas. Coupled phase transformations and plasticity as a field theory of deformation incompatibility. *International Journal of Fracture*, 74:87–94, 2012.

[72] Arash Yavari, Jerrold E. Marsden, and Michael Ortiz. On spatial and material covariant balance laws in elasticity. *Journal of Mathematical Physics*, 47:042903, 2006.

[73] Arash Yavari and Alain Goriely. Nonlinear elastic inclusions in isotropic solids. *Proceedings of the Royal Society of London A: Mathematical, Physical and Engineering Sciences*, 469(2160), 2013.

[74] Ralf Denzer and Andreas Menzel. Configurational forces for quasi-incompressible large strain electro-viscoelasticity e application to fracture mechanics. *European Journal of Mechanics A/Solids*, 48:3–15, 2014.

[75] P. Podio-Guidugli. Configurational forces: are they needed? *Mech. Res. Commun.*, 29(6):513–519, November-December 2002.

[76] P. Macklin and J. Lowengrub. An improved geometry-aware curvature discretization for level set methods: Application to tumor growth. *J. Comput. Phys.*, 215:392–401, 2006.

[77] V. S. Rao, T. J. R. Hughes, and K. Garikipati. On modelling thermal oxidation of silicon ii: numerical aspects. *Int. J. Numer. Methods Eng.*, 47(1-3):359–377, 2000.

[78] V. S. Rao and T. J. R. Hughes. On modelling thermal oxidation of silicon i: theory. *Int. J. Numer. Methods Eng.*, 47(1-3):341–358, 2000.

[79] K. Garikipati and V. S. Rao. Recent advances in models for thermal oxidation of silicon. *J. Comput. Phys.*, 174(1):138–170, November 2001.

[80] V. K. Kalpakides and A. I. Arvanitakis. Configurational forces in continuous theories of elastic ferroelectrics. In P. Steinmann, editor, *IUTAM Symposium on Progress in the Theory and Numerics of Configurational Mechanics*, volume 17 of *IUTAM Bookseries*, pages 229–238. Springer Netherlands, 2009.

[81] K. Garikipati, J. E. Olberding, H. Narayanan, E. M. Arruda, K. Grosh, and S. Calve. Biological remodelling: Stationary energy, configurational change, internal variables and dissipation. *J. Mech. Phys. Solids*, 54:1493–1515, 2006.

[82] K. Bhattacharya and R. V. Kohn. Elastic energy minimization and the recoverable strains of polycrystalline shape-memory materials. *Archive for Rational Mechanics and Analysis*, 139:99–180, 1997.

[83] S. Müller. *Calculus of Variations and Geometric Evolution Problems: Lectures given at the 2nd Session of the Centro Internazionale Matematico Estivo (C.I.M.E.) held in Cetraro, Italy, June 15–22, 1996*, chapter Variational models for microstructure and phase transitions, pages 85–210. Springer Berlin Heidelberg, Berlin, Heidelberg, 1999.

[84] J. M. Ball and E. C. M. Crooks. Local minimizers and planar interfaces in a phase-transition model with interfacial energy. *Calculus of Variations*, 40:501–538, 2011.

[85] S. Rudraraju, A. Van der Ven, and K. Garikipati. Three-dimensional isogeometric solutions to general boundary value problems of Toupin's gradient elasticity theory at finite strains. *Comput. Methods Appl. Mech. Eng.*, 278:705–728, 2014.

[86] S. Rudraraju, A. Van der Ven, and K. Garikipati. Mechano-chemical spinodal decomposition: A phenomenological theory of phase transformations in multi-component crystalline solids. *Nature npj Computational Materials*, 2, 2016.

[87] R. Toupin. Elastic materials with couple-stresses. *Arch. Ration. Mech. Anal.*, 11:385–414, 1962.

[88] G. Russo and P. Smereka. A remark on computing distance functions. *J. Comput. Phys.*, 163:51–67, 2000.

[89] A. N. Brooks and T. J. R. Hughes. Streamline upwind/Petrov-Galerkin formulations for convection dominated flows with particular emphasis on the incompressible Navier-Stokes equations. *Comput. Methods Appl. Mech. Eng.*, 32:199–259, 1982.

[90] H.M Flower and P.R Swann. An in situ study of titanium oxidation by high voltage electron microscopy. *Acta Metallurgica*, 22(11):1339 – 1347, 1974.

[91] Digby D. Macdonald. On the formation of voids in anodic oxide films on aluminum. *J. Electrochem. Soc.*, 140(3):L27 – L30, 1993.

[92] P.Y. Hou, Y. Niu, and C. Van Lienden. Analysis of pore formation at oxide–Alloy interfaces—I: Experimental results on FeAl. *Oxidation of Metals*, 59(1):41–61, Feb 2003.

[93] Yanli Wang, Keith Duncan, Eric Wachsman, and Fereshteh Ebrahimi. Effects of oxygen vacancy concentration on mechanicsl properties of cerium oxide. *ECS Transactions*, 1(7):23 – 31, 2006.

[94] Mazharul M. Islam, Boubakar Diawara, Vincent Maurice, and Philippe Marcus. Atomistic modeling of voiding mechanisms at oxide/alloy interfaces. *The Journal of Physical Chemistry C*, 113:9978 – 9981, 2009.

[95] Russell R. Wang and Kon K. Fung. Oxidation behavior of surface-modified titanium for titanium-ceramic restorations. *The Journal of Prosthetic Dentistry*, 77(4):423 – 434, 1997.

[96] Shang-Di Mo and W. Y. Ching. Electronic and optical properties of three phases of titanium dioxide: Rutile, anatase, and brookite. *Phys. Rev. B*, 51:13023–13032, May 1995.

[97] Daan Frenkel and Berend Smit. Chapter 7 - Free energy calculations. In Daan Frenkel and Berend Smit, editors, *Understanding Molecular Simulation (Second Edition)*, pages 167 – 200. Academic Press, San Diego, 2002.

[98] R. T. DeHoff. *Thermodynamics in Materials Science*. McGraw-Hill, 2006.

[99] Otto Redlich and A. T. Kister. Algebraic representation of thermodynamic properties and the classification of solutions. *Industrial & Engineering Chemistry*, 40(2):345–348, 1948.

[100] Germund Dahlquist and Åke Björck. *Numerical methods in scientific computing*, volume 1. Philadelphia: Society for Industrial and Applied Mathematics, 2008.

[101] Josef Tomiska. Mathematical conversions of the thermodynamic excess functions represented by the Redlich-Kister expansion, and by the Chebyshev polynomial series to power series representations and vice-versa. *Calphad*, 8(4):283 – 294, 1984.

[102] N. Ouerfelli, O. Iulian, and M. Bouaziz. Competition between Redlich-Kister and improved Herrez equations of correlation viscosities in 1,4-dioxane+water binary mixtures at different temperatures. *Physics and Chemistry of Liquids*, 48(4):488–513, 2010.

[103] John W. Cahn and John E. Hilliard. Free energy of a nonuniform system. I. Interfacial free energy. *The Journal of Chemical Physics*, 28(2):258–267, 1958.

[104] Benjamin Paul Burton and Axel van de Walle. First principles phase diagram calculations for the octahedral-interstitial system $\alpha\mathrm{TiO}_X$, $0 \leq X \leq 1/2$. *Calphad*, 39:97 – 103, 2012.

[105] John C. Thomas and Anton Van der Ven. Finite-temperature properties of strongly anharmonic and mechanically unstable crystal phases from first principles. *Phys. Rev. B*, 88:214111, Dec 2013.

[106] G. Kresse and J. Furthmüller. Efficient iterative schemes for *ab initio* total-energy calculations using a plane-wave basis set. *Phys. Rev. B*, 54:11169–11186, Oct 1996.

[107] G. Kresse and D. Joubert. From ultrasoft pseudopotentials to the projector augmented-wave method. *Phys. Rev. B*, 59:1758–1775, Jan 1999.

[108] Carl de Boor. On calculating with B-splines. *Journal of Approximation Theory*, 6(1):50–62, July 1972.

[109] L. Q. Chen. Phase-field models for microstructure evolution. *Annual Review of Materials Research*, 32, 2002.

[110] A. Van der Ven, H. C. Yu, G. Ceder, and K. Thornton. Vacancy mediated substitutional diffusion in binary crystalline solids. *Progress in Materials Science*, 55(2):61–105, 2010.

[111] T. J. R. Hughes, J. A. Cottrell, and Yuri Bazilevs. Isogeometric analysis: CAD, finite elements, NURBS, exact geometry and mesh refinement. *Computer Methods in Applied Mechanics and Engineering*, 194:4135–4195, October 2005.

[112] J. Austin Cottrell, Thomas J. R. Hughes, and Yuri Bazilevs. *Isogeometric Analysis: Toward Integration of CAD and FEA*. John Wiley & Sons, Ltd, Chichester, 2009.

[113] Nathan O. Collier, Lisandro Dalcín, and Victor M. Calo. PetIGA: High-performance isogeometric analysis. *CoRR*, abs/1305.4452, 2013.

[114] J. Z. Zhu, Z. K. Liu, V. Vaithyanathan, and L. Q. Chen. Linking phase-field model to CALPHAD: application to precipitate shape evolution in Ni-base alloys. *Scripta Materialia*, 46:401–406, 2002.

[115] V. Vaithyanathan, C. Wolverton, and L.Q. Chen. Multiscale modeling of precipitation in alcu binary alloys. *Acta Materialia*, 52(10):2973 – 2987, 2004.

[116] Hctor Gmez, Victor M. Calo, Yuri Bazilevs, and Thomas J.R. Hughes. Isogeometric analysis of the CahnHilliard phase-field model. *Computer Methods in Applied Mechanics and Engineering*, 197(49):4333 – 4352, 2008.

[117] M. D. McKay, R. J. Beckman, and W. J. Conover. A comparison of three methods for selecting values of input variables in the analysis of output from a computer code. *Technometrics*, 21(2):239–245, 1979.

[118] I.M Sobol'. On the distribution of points in a cube and the approximate evaluation of integrals. *USSR Computational Mathematics and Mathematical Physics*, 7(4):86 – 112, 1967.

[119] Paul Bratley and Bennett L. Fox. Algorithm 659: Implementing sobol's quasirandom sequence generator. *ACM Trans. Math. Softw.*, 14(1):88–100, March 1988.

[120] M.A. Bessa, R. Bostanabad, Z. Liu, A. Hu, Daniel W. Apley, C. Brinson, W. Chen, and WingKam Liu. A framework for data-driven analysis of materials under uncertainty: Countering the curse of dimensionality. *Computer Methods in Applied Mechanics and Engineering*, 320:633 – 667, 2017.

[121] Martín Abadi, Ashish Agarwal, Paul Barham, Eugene Brevdo, Zhifeng Chen, Craig Citro, Greg S. Corrado, Andy Davis, Jeffrey Dean, Matthieu Devin, Sanjay Ghemawat, Ian Goodfellow, Andrew Harp, Geoffrey Irving, Michael Isard, Yangqing Jia, Rafal Jozefowicz, Lukasz Kaiser, Manjunath Kudlur, Josh Levenberg, Dan Mané, Rajat Monga, Sherry Moore, Derek Murray, Chris Olah, Mike Schuster, Jonathon Shlens, Benoit Steiner, Ilya Sutskever, Kunal Talwar, Paul Tucker, Vincent Vanhoucke, Vijay Vasudevan, Fernanda Viégas, Oriol Vinyals, Pete Warden, Martin Wattenberg, Martin Wicke, Yuan Yu, and Xiaoqiang Zheng. TensorFlow: Large-scale machine learning on heterogeneous systems, 2015. Software available from tensorflow.org.

[122] W. Bangerth, D. Davydov, T. Heister, L. Heltai, G. Kanschat, M. Kronbichler, M. Maier, B. Turcksin, and D. Wells. The `deal.II` library, version 8.4. *Journal of Numerical Mathematics*, 24, 2016.

[123] Christopher M. Bishop. *Neural networks for pattern recognition*. Oxford : Clarendon Press, 1995.

[124] Jrgen Schmidhuber. Deep learning in neural networks: An overview. *Neural Networks*, 61:85 – 117, 2015.

[125] Yann LeCun, Yoshua Bengio, and Geoffrey Hinton. Deep learning. *Nature*, 521:436 – 444, 2015.

[126] Subana Shanmuganathan and Sandhya Samarasinghe, editors. *Artificial Neural Network Modelling*. Springer International Publishing, 2016.

[127] James Bergstra and Yoshua Bengio. Random search for hyper-parameter optimization. *J. Mach. Learn. Res.*, 13(1):281–305, February 2012.

[128] Seong Gyoon Kim, Won Tae Kim, and Toshio Suzuki. Phase-field model for binary alloys. *Phys. Rev. E*, 60:7186–7197, Dec 1999.